UNIVERSITAT POLITÈCNICA DE CATALUNYA
BARCELONATECH

MASTER THESIS

Experimental Investigation of Fatigue Behavior of Curved Composite Laminates

Ezgi Üstün

SUPERVISED BY

Antonio Manuel Mateo
Demirkan Çöker

Universitat Politècnica de Catalunya
Master in Aerospace Science & Technology
July 2016

Experimental Investigation of Fatigue Behavior of Curved Composite Laminates

BY

Ezgi Üstün

DIPLOMA THESIS FOR DEGREE

Master in Aerospace Science and Technology

AT

Universitat Politècnica de Catalunya

SUPERVISED BY:

Prof. Antonio Manuel Mateo

UPC-Department of Materials Science and Metallurgical Engineering

Assoc. Prof. Demirkan Çöker

METU-Aerospace Engineering Department

ABSTRACT

In the aerospace and wind turbine industries, high demand for light weight structures with high strength extend the use of composite laminates in a wide variety of geometries as load carrying elements. However, more complex geometries as curved composite laminates experience delamination and matrix cracking due to high interlaminar stresses induced in the curved region. Moreover, under cyclic loading failure on these components initiates under lower stress states so that fatigue behavior of curved composite laminates are critical. This thesis discusses the experimental investigation of fatigue behavior of curved composite laminates under bending moment. Bending moment is obtained at the curved region by applying axial load from both tips of the curved composite laminates. A special loading fixture is designed in order to apply axial load to curved specimens in universal testing machine. Two different lay-up configurations are investigated; $[0]_{15s}$ unidirectional as fiber dominated and $[0_3/90_3/0_3/90_3/0_3]_s$ cross-plied laminates as matrix dominated. Static loading experiments are conducted in order to obtain average ultimate strength of materials to use in fatigue loading experiments and compare the damage pattern with the fatigue failure. The load-displacement curves are recorded for both static and fatigue loading cases. The failure is observed using high speed camera under static loading. DSLR camera images and micrographs are taken for both static and fatigue experiments. Under static loading, two load drop is observed for [0] UD laminates until failure. Under fatigue loading, [0] UD laminates experience one sharp load drop, then stiffness degrades gradually until failure. The failure pattern of [0] UD laminates under static and fatigue loading is completely different. Cross-plied laminates show similar behavior on load-displacement curves and failure mechanisms under static and fatigue loading. Under static and fatigue loading, unexpected failure mechanisms are observed for cross-plied laminates which are found to be sensitive to the manufacturing defects.

I would like to dedicate my thesis to my beloved parents…

ACKNOWLEDGEMENTS

First of all, I would like to thank my advisor Antonio Manuel Mateo, for providing an opportunity of pursuing my thesis studies together. His perspective always took me a step forward. I would like to express my special thanks to my co-advisor Assoc. Prof. Demirkan Çöker for his offer to study together during M. S. research. He always showed his continuous support, patience and motivation during my thesis studies. His expertise guidance helped me from beginning to end of my research and writing my thesis.

My sincere thanks also goes to Assist. Prof. Oğuz Uzol for special opportunities to work at a great environment of RUZGEM / METUWIND facilities.

I thank to my fellows from Coker-Lab: Burcu Taşdemir and Tamer Tahir Ata for being a great companion during our studies, experiments and their countless help during thesis period. In particular, I would like to thank to İmren Uyar, Denizhan Yavaş and Başar Kütükoğlu for their friendship and conveying their experiences about research and the lab environment.

I would like to acknowledge TAI-TUSAŞ for providing me specimens used during my thesis studies. I specially thanks to Gökhan Gürün for his supports during manufacturing process.

In addition I thank to my colleagues in TAI: Büşra Yaban, Enes Erkan Kısa, Mert Güven, Kaan Ergül and Tuğçe Koç for their friendship and their support during the most intense period of my thesis studies. Moreover, I would like to thank to Başak Okumuş and Barış Deniz Sağlam.

Special thanks go to my fellow in Coker-Lab and very best friend Miray Aydan Arca for her limitless support, her motivation and everything for seven years. With her assist, I could continue when I think I fail, with her experiences and support I could establish the background and finish my thesis.

I would like to thank especially to the other half of my life, my love Burak Çakman for his best support all the time. His encouragement and his belief created my self-confidence, always kept me from falling. He was the one to motivate me in writing my thesis in a very short time.

Last but not the least; I would like to thank my family: my parents Mukaddes Üstün and Hüseyin Üstün, for their unlimited support both financially and spiritually throughout my life.

Table of Contents

List of Figures

List of Tables

List of Symbols

G	Elastic modulus
E_i	Energy release rate
L_1	Left arm
L_2	Right arm
P	Axial load parallel to the right arm
R_i	Inner Radius
M	Moment loading
V	Shear load perpendicular to the right arm
t	Thickness
w	Width
ρ	Density
ν_{ij} $(i \neq j)$	Poisson ratio
σ_r	Radial stress
$\tau_{r\theta}$	Shear stress
R_m	Mean radius

Abbreviations

ASTM	American Society for Testing Materials
BTW	Basic Testware
CBS	Curved Beam Strength
CFRP	Carbon Fiber Reinforced Polymers
DCB	Double Cantilever Beam
FEA	Finite Element Analysis
FRP	Fiber Reinforced Polymers
ILT	Interlaminar Tensile
MRR	Modulus Reduction Ratio
MPT	Multi-Purpose Testware
NDT	Nondestructive Testing
SS	Steady State
UD	Unidirectional
TTU	Through-Transmission Ultrasound

Chapter 1

INTRODUCTION

In this chapter, first of all, composite is defined briefly. Afterwards, composite material and curved composite laminate applications in aerospace and wind turbine industry are discussed. Fatigue behavior of composite laminates and metals is compared in detail. Then, loads on curved composite laminates are presented and failure mechanisms, primarily delamination and matrix cracking are introduced. Finally, the scope of this study is described.

1.1. The history of composite materials

Composite is a material which consists of two or more phases on a macroscopic level, in order to achieve superior designs by using independent mechanical performance of the forming materials. One of the phases of composite materials is reinforcement and the other is matrix (**Figure 1.1**). The reinforcement may be in the form of fibers, particles or flakes. The matrix phase materials are continuous and provide protection and support [1, 2]. Desired properties are obtained by stacking reinforcement phase in the appropriate direction.

Composites may be found in nature as well. Wood and bones are the best examples for natural composites.

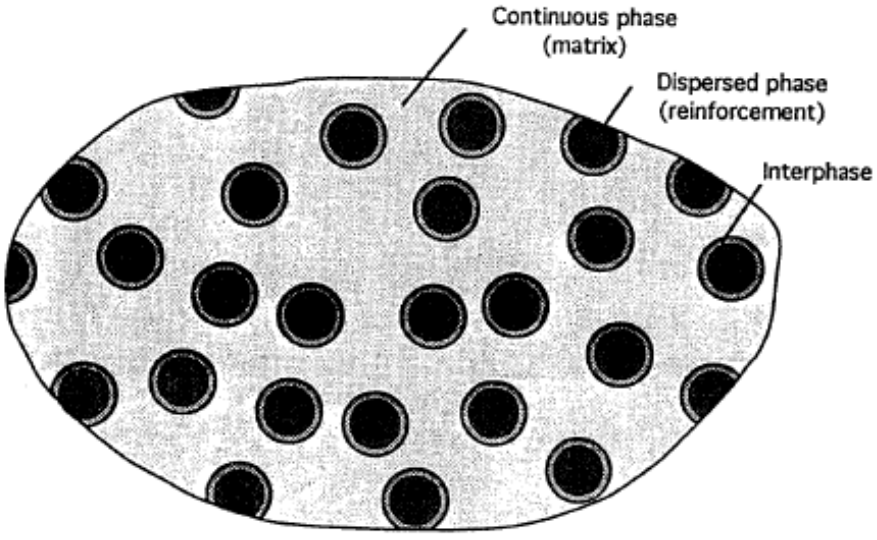

Figure 1.1 Illustration of phases forming composite materials [1]

The concept of composite dates back in the history. Bamboo was used by Israelites as reinforcement for clay bricks. Bamboo reinforced mud walls and glued laminated woods were used in houses by ancient Egyptians. During wars in history, composite bows were developed as weapons, also laminated metals were used in forging swords. In the nineteenth century iron rods were started using to reinforce masonry and led to the development of steel-reinforced concrete. In the twentieth century, glass fiber reinforced resins were used initially in the industry, especially in boats. In 1960s, the first boron and high strength carbon fiber applications were presented as aircraft components. Since 1970s metal matrix composites were applicable in the industry and the applications of composites materials expanded to automotive, aircraft and sporting industries [1, 2, 3]. The major types of composite fibers commonly used in different industries are explained and compared in the following paragraphs:

Carbon/Graphite Fibers: Carbon and graphite fibers are based on graphene (hexagonal) layer networks present in carbon. Graphene layers, or planes, are stacked with three dimensional order and form graphite. Usually extended time and temperature processing are required, hence the process of graphite fibers is more expensive. Bonding between planes is weak. Carbon fibers are very stiff and strong, 3 to 10 times stiffer than glass fibers. Carbon fiber is used for structural aircraft applications, such as floor beams, stabilizers, flight controls, and primary fuselage and wing structure. Advantages include its high strength and corrosion resistance. Disadvantages comprise lower conductivity than aluminum; therefore, a lightning protection mesh or coating is necessary for aircraft parts that are prone to lightning strikes. Another disadvantage of carbon fiber is its high cost. Carbon fiber is gray or black in color and is available as dry fabric and pre-preg material [4].

Glass Fibers: Fiberglass is often used for secondary structure on aircraft, such as fairings, and wing tips. It is also used for helicopter rotor blades. There are several types of fiberglass used in the aviation industry, mainly, E-glass as electrical glass and S-glass as structural fiber because it has higher strength than E-glass. Advantages of fiberglass are lower cost than other composite materials, chemical or galvanic corrosion resistance, and electrical insulation. Fiberglass has a white color and is available as a dry fiber fabric or pre-preg material [4].

Kevlar® (Aramid) Fibers: Aramid fibers are light weight, strong, and tough. An advantage of aramid fibers is their high resistance to impact damage, so they are often used in areas prone to impact damage. Their main disadvantage is weakness in compression and hygroscopy. Components made of aramid fibers need to be protected from the environment. Another disadvantage is that Kevlar® is difficult to machining. Kevlar® is generally used for military ballistic and body armor applications. It has a natural yellow color and is available as dry fabric and pre-preg material [4].

Boron Fibers: Boron fibers are very stiff and have a high tensile and compressive strength. The fibers have a relatively large diameter and are not flexible, hence, only

they are available as a pre-preg tape. Boron fibers are used to repair cracked aluminum aircraft skins, because the thermal expansion of boron is close to aluminum and boron fibers have no corrosion potential. The boron fibers are very expensive and used primarily in military aviation applications [4].

1.2. Composite materials in aerospace applications

In this section applications of composite materials in aircraft and turbine industry are explained in detail. Organic composite materials are an alternative to metals in many aerospace and wind turbine applications due to the advantage of weight saving without any loss of strength and stiffness. In addition to improved specific strength and stiffness, composites have superior properties over conventional metals such as; fatigue resistance, thermal conductivity, corrosion and impact resistance [2]. Due to these advantages, fiber reinforced polymers (FRPs) especially carbon fiber reinforced polymers (CFRPs) satisfy the requirements of advanced technologies and are commonly used in both aerospace and wind turbine industries.

The first composite aircraft in history is accepted the British two-seated small airplane Bristol Scout in the 1910s, however, the usage of composites in large transport aircrafts was not seen until the early 60s [5,6]. In the last decades, there has been an increasing trend in using composite materials in aerospace industry. In **Figure 1.2** the evolution of composite materials in aerospace industry is presented. In 1970s only 5% of airframe weight was manufactured by composite materials. Airplane manufacturers used composite materials as secondary structures and in control surfaces as can be seen in **Figure 1.3**. In 1988, Airbus introduced A320, the first airplane with tail section made of composite and in 1995 Boeing built B777 with composite tail too [7]. As shown in Figure 1.3 the usage of composite materials in airframe increases year by year and nowadays even fuselage is manufactured by composite. In these days, new aircrafts consist of approximately 50% of composite materials (**Figure 1.4**).

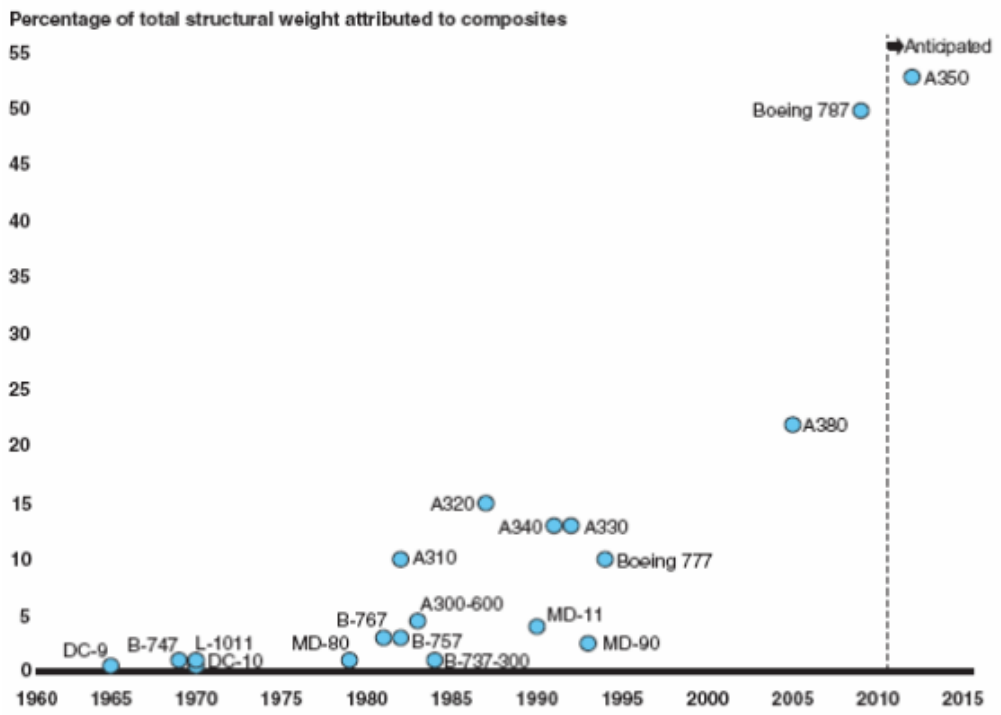

Figure 1.2 Commercial airplanes over time by percentage of composite materials [7]

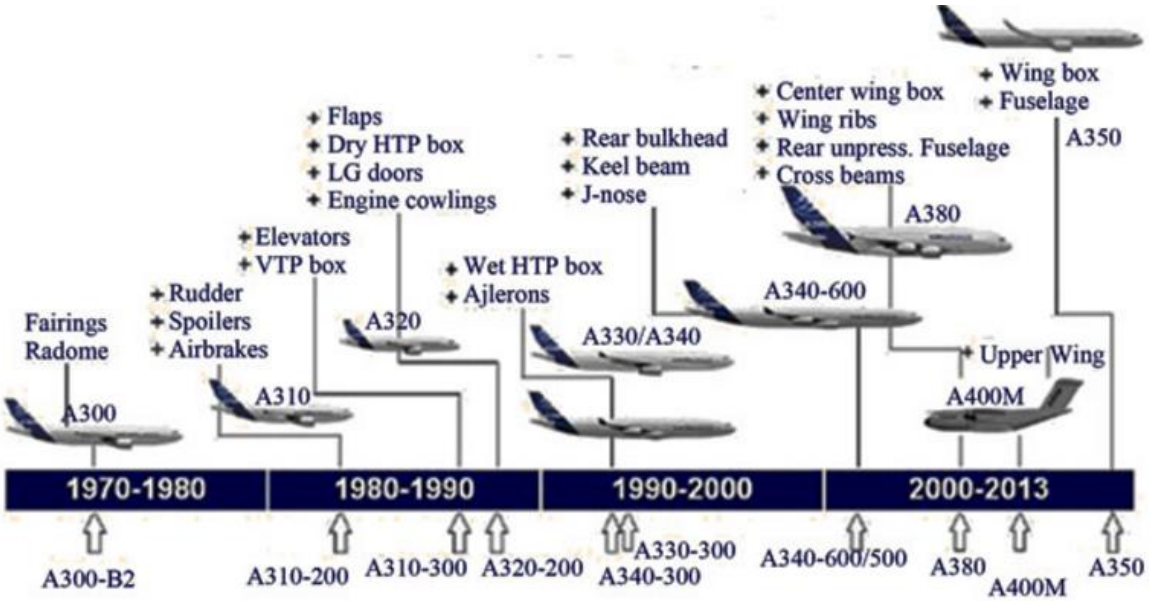

Figure 1.3 Evolution of composite applications [8]

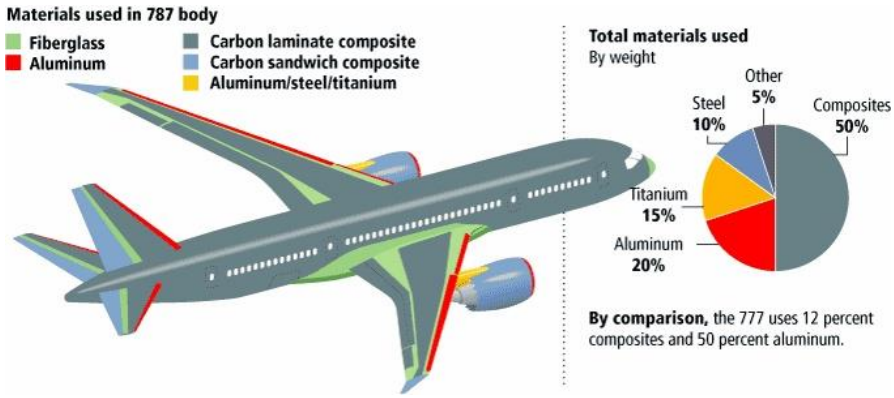

Figure 1.4 Types of materials used in 787 aircraft structure in weight percent [9]

With developing manufacturing capabilities of composites, more complex geometries such as curved laminates can be used for both aircraft and wind turbine industry, instead of metallic structures. Curved composite laminates are used in wing structure as critical support members such as ribs and spars. Although, composites have superior advantages over metallic structures, since they have a laminated nature, their damage mechanisms are different than those of metals. For that reason, the application of curved composite laminates and their failure mechanisms are explained in detail in the following sections.

1.3. Fatigue behavior of composites vs. metals

Aerospace structures are subjected to cyclic loading such as fluctuating loads on aircraft wings. Not only aircraft components, but also wind turbine blades are fatigue critical machines [10]. With time, cyclic loads cause structures lose their strength and give them a finite life [11]. Great number of failures in service occurs due to fatigue loading and relatively few are static failure [12]. Thus, fatigue of a structural element is a vital design criterion in both aerospace and wind turbine industries.

Composite materials have taken place of metals in aerospace systems due to their superior properties. Especially, composite materials offer great resistance to fatigue loading compared to metals. Fatigue behavior of composite materials totally differs from that of metals. Predictable crack initiation and growth are observed in metals leading to failure [11]. However, composites have different failure mechanisms such as delamination, matrix cracking, transverse-ply cracking, debonding, fiber failure, etc. It is difficult to predict the damage modes and which mode or modes will dominate the failure [11, 13]. In **Figure 1.5** variety of different damage modes of composite materials under fatigue loading is shown. The early stage of damage development consists of matrix cracking in the off-axis plies. Phase 2 begins by initiation of transverse cracks which is called the secondary matrix cracks leading to the interlaminar cracks. In the following phase, these interlaminar cracks cause separation of the plies locally. In the final phase of damage development, matrix cracking interactions increase and locally

failed regions find a path, then localized fiber failures are formed which rapidly lead to the loss of structural integrity of the material, hence, fracture.

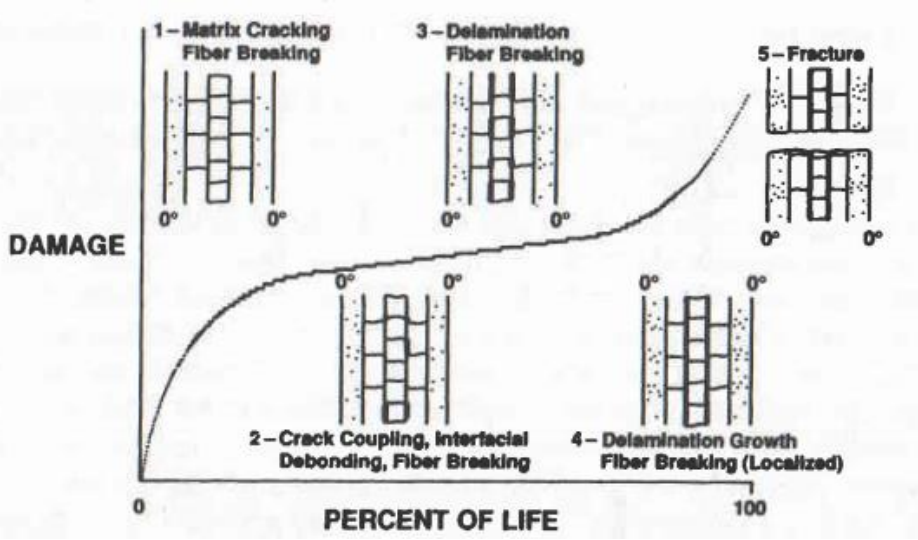

Figure 1.5 Variety of damage modes of composite materials under fatigue loading [15]

The difference between fatigue behavior of composite materials and metals is shown in **Figure 1.6**. All structures have initial flaws which may eventually cause fatigue crack growth [14]. As illustrated in **Figure 1.6**, the initial damage in composites, as broken fibers, matrix cracking, etc., can be much larger than initial imperfections in metals, which are primarily small cracks. The crack initiation time represents most of the fatigue life of metals. Then the propagation of crack until catastrophic failure occurs suddenly with little warning [13]. **Figure 1.7** shows the fracture surface of a coil spring. The fatigue crack starts at a surface flaw and it progresses in the direction of maximum stress [12]. In contrast of metals, composite materials cracking occupies only the end of the fatigue life. Hence, depending on the fiber orientation, composite materials are more damage tolerant over metals [11, 15].

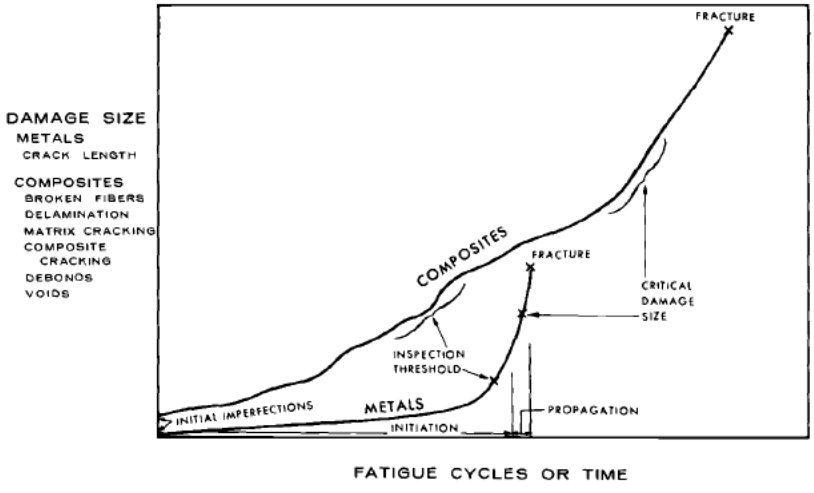

Figure 1.6 Comparison of fatigue behavior in metals and composites [11]

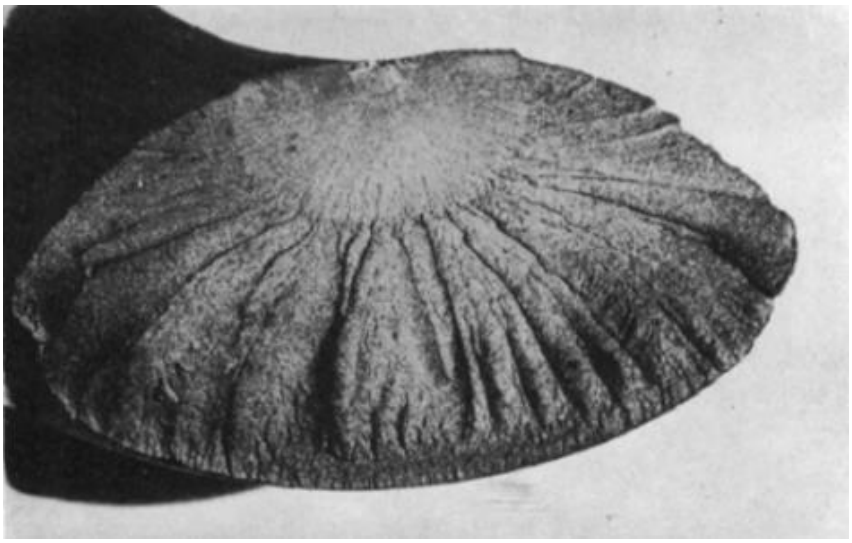

Figure 1.7 Fatigue fracture surface of a coil spring [12]

Besides failure modes, low cycle and high cycle fatigue behaviors are different between metals and composites. Compared to static and low cycle fatigue strength, composite materials have higher high cycle fatigue strength. Under fatigue loading, low stresses are critical design factors for metals [11]. However, it is wrong to assume that stresses below the monotonic failure stress inevitably result in failure of composite materials [13].

Figure 1.8 shows the stiffness versus life plot of metal and composite materials. Conventional metals hold stiffness until the end of their life, then, stiffness drops sharply. In contrast, composites lose stiffness gradually over the lifetime [15].

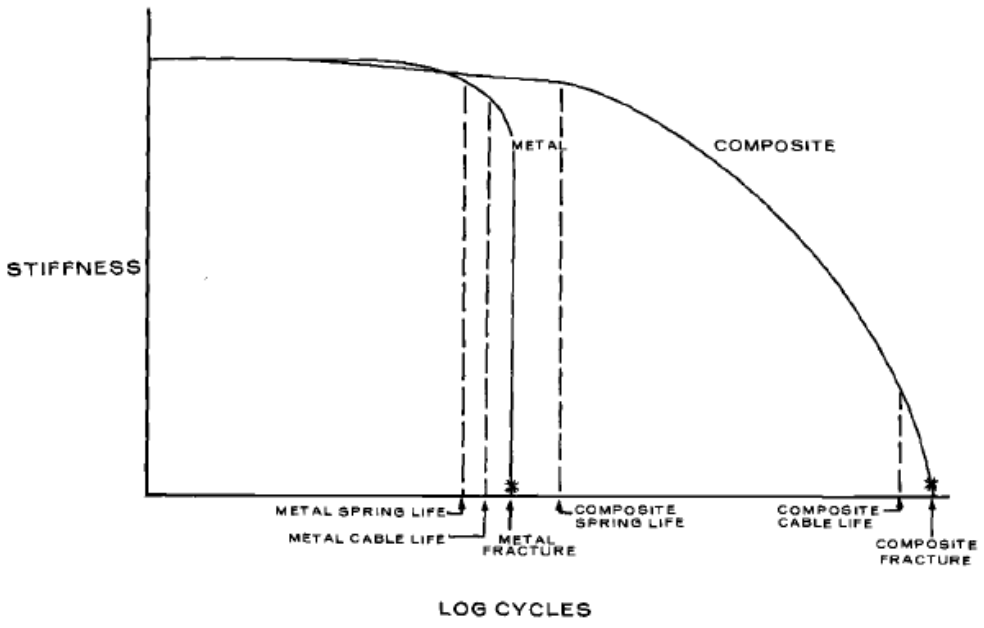

Figure 1.8 Schematic stiffness comparison of metal and composite under fatigue loading [11]

Typical SN curves for different composite materials and metals are shown in **Figure 1.9**. Curves of composite materials are flatter than those of the metals. The initial advantage of higher strength of composites over metals provides higher performance under high cycle fatigue loading [15]. This advantage of longer life besides specific strength and stiffness over metals is the primary reason to increase the demand of composite materials in aerospace and wind turbine applications.

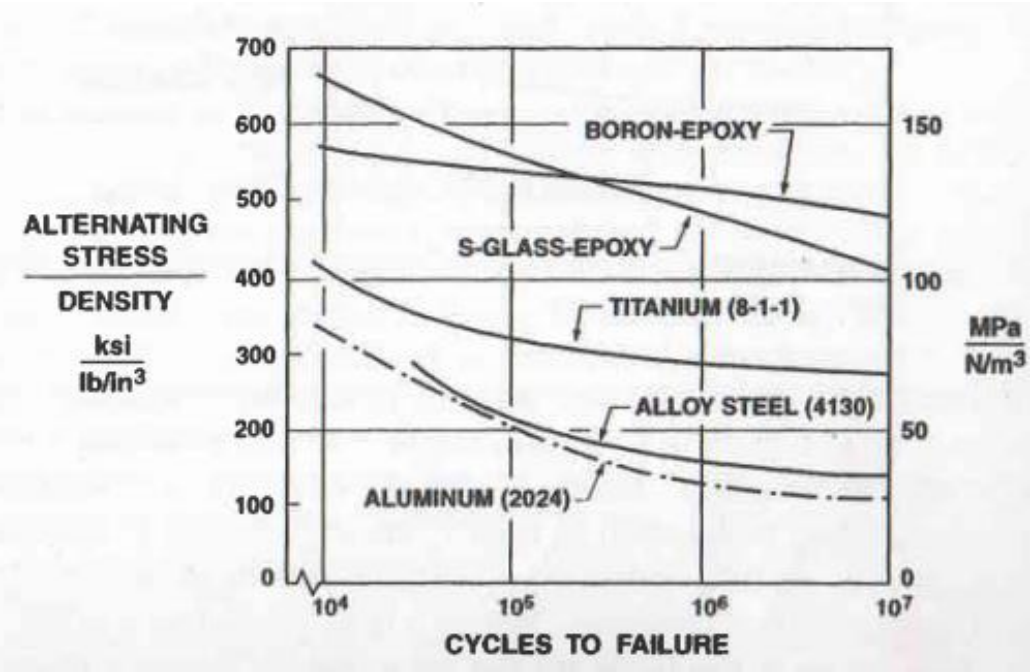

Figure 1.9 SN curves of different metals and composite materials [15]

Composite materials provide an opportunity of design desired stiffness by different fiber orientations. This is another reason that makes composite materials attractive. In general, unwoven laminates have superior fatigue behavior than woven laminates [11]. Prediction of failure mechanisms is more complex since composite materials are nonhomogeneous and anisotropic. Hence, for any number of cycles the changes in stiffness in one direction may be unrelated to stiffness change in the other direction [11]. Thus, with wider applications of composite materials it is vital to detect damage mechanisms under fatigue loading.

1.4. Curved composite laminates and fatigue loading

In this section the applications of curved composite laminates in aerospace and wind turbine industry are explained. The applied loads and failure mechanisms that curved composite laminate members can experience are described in detail.

1.4.1. Curved composite laminate structures

The wing is essentially a beam which transmits and gathers the entire applied air load to the attachment to the fuselage. The most critical part of the airplane is wing box which is required to be light and strong enough to endure bending and torsion moment created on the wing [16]. With developing manufacturing capabilities of composites, more complex geometries such as curved composite laminates can be used in aircraft and wind turbine industry instead of metallic structures. These box structures consist of load carrying members as ribs, spars and stringers, which are the main applications of curved composite materials replacing metal components. **Figure 1.10** shows the applications of curved composite laminates in aircraft wings and wind turbine blades.

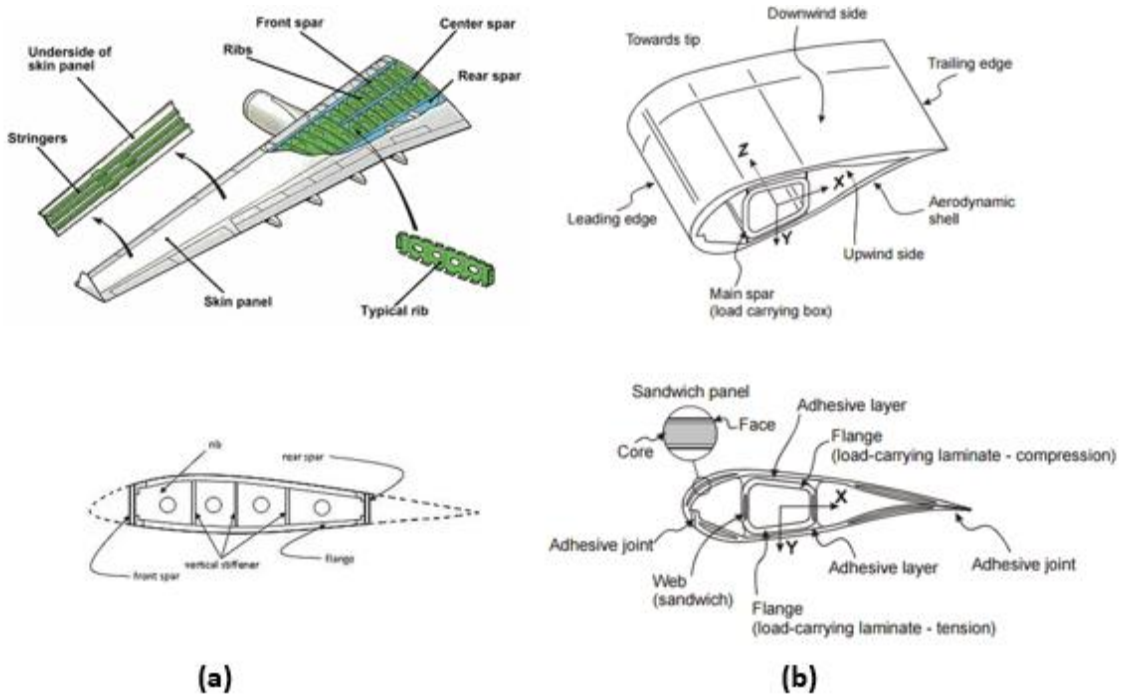

Figure 1.10 Application of curved composite laminates [17] (a) wing internal structure; (b) wind turbine blade structure [18]

In a typical wing cross section, curved composite laminate parts are placed into the wing covers as the extension of spars/ ribs that are laid through the skin or as a separate part which connect the rib to the skin. Examples of these load carrying members are explained in the following paragraphs;

Ribs: In an aircraft, ribs are forming elements of the structure of a wing. Ribs form the airfoil shape of the wing, and the skin adopts this shape when stretched over the ribs. The ribs need to support the wing panels, achieve the desired aerodynamic shape, add strength, prevent buckling, and separate the individual fuel tanks within the wing [19] as shown in **Figure 1.11**.

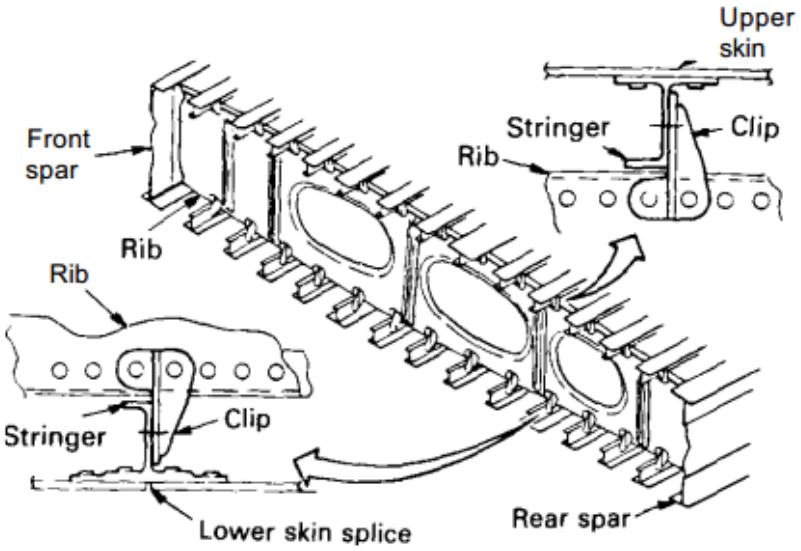

Figure 1.11 Typical rib construction [16]

Stringers: A stringer is a thin strip of material, to which the skin of the aircraft is fastened (**Figure 1.12**). Its primary function is to transfer the bending loads acting on the wings onto the ribs and spar [19]. Stringers are the most effective mechanism to save weight [16]. **Figure 1.12**b shows the typical interior stringer of the Boing 787.

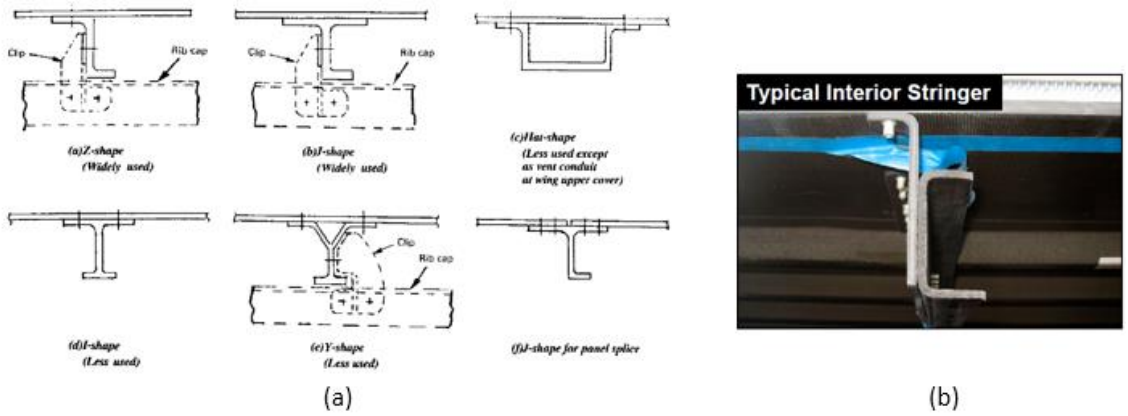

Figure 1.12 (a) Types of stringers; (b) Boeing 787 interior stringer panel [16, 20]

Spars: Spars are the main structural members of the wing. They extend from the fuselage to the tip of the wing (**Figure 1.13**). The entire load carried by the wing is taken up by the spars. The spars are designed to have great bending strength [21].

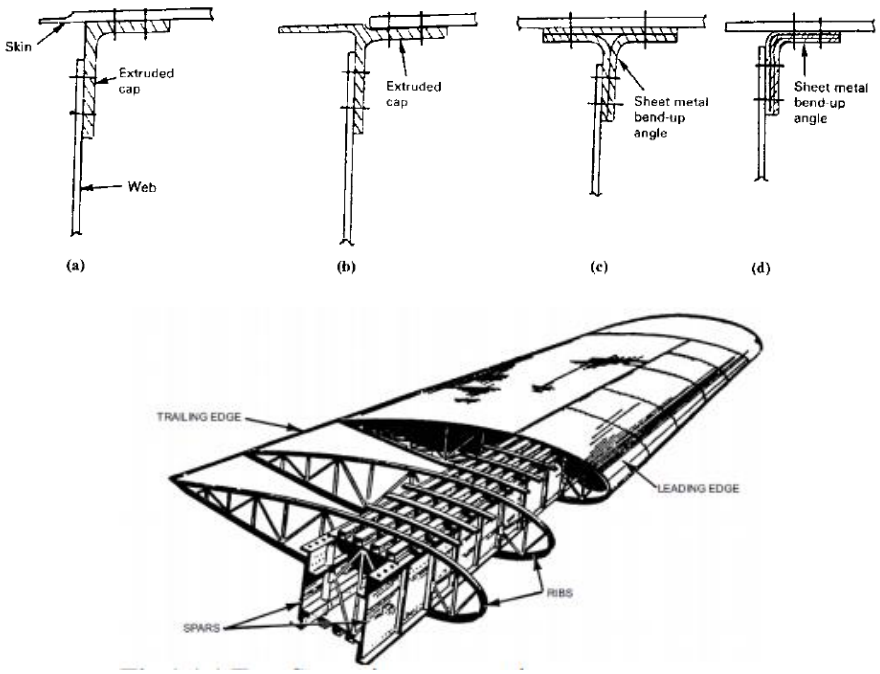

Figure 1.13 Typical spar cap configurations [16]

1.4.2. Service loads on curved composite laminates

Aeronautical structures are designed to be operated for several decades. Fatigue damage in these structures occurs due to repetitive loads in service under various loading conditions [22]. A typical airframe is exposed to concentrated and distributed loads during flight. For aeronautical structures, the load cycles are related to the number of flights, ranging from constant amplitude to arbitrary spectrum loading such as, fuselage pressurization in every load, wing loads due to take off, equilibrium, turbulence, gust, etc. [22].

A typical wing is subjected to both aerodynamic and structural loads during its service life. The wing is designed to provide adequate lift and minimize drag. The aircraft wing is also designed structurally to carry the entire weight of the aircraft [21]. Hence, the wing is one of the most critical components of an aircraft both aerodynamically and structurally. In order to prevent larger designs and thick frames, also to provide requisite strength and light weight, wing box is designed which carried the normal forces formed by upper and lower wing skin during flight [23].

In every flight, a typical wing rib section located in a wing box is subjected to mainly three types of loads acting on a wing rib section, which are: the axial load (parallel to the arm, P), the shear load (perpendicular to the arm, V), and the bending moment (M) (**Figure 1.14b**). These are the reaction forces to the applied loads on wing rib structure (**Figure 1.14a**). These loads can be explained as follows [24]:

- Shear loads in the web

- Distributed pressure load at the sides due to the air and fuel inside the box structure, resulting in moment load at the curved section

- Compression and tension loads in the chord wise direction due to the Poisson's ratio effect and end load at spars

- Shear flow distribution on a rib bordering a cut-out

- Torsion loads due to the air flow during flight

- Redistributes concentrated loads: such as nacelle and landing gear loads to wing spars and cover panels

Under these loads, the wing box is more highly loaded than the wing itself. On this wise, the materials used in critical locations in the wing box are required to have higher stiffness, strength, fatigue resistance and fracture toughness than metal alloys used in main wing section in order to accomplish many flight hours without experience fatigue damage [25]. In modern aircrafts, these critical components are usually constructed with CFRPs. The loads applied to curved composite parts located in the wing box structure create a complex stress state at the curved region which causes fatigue damage on these components.

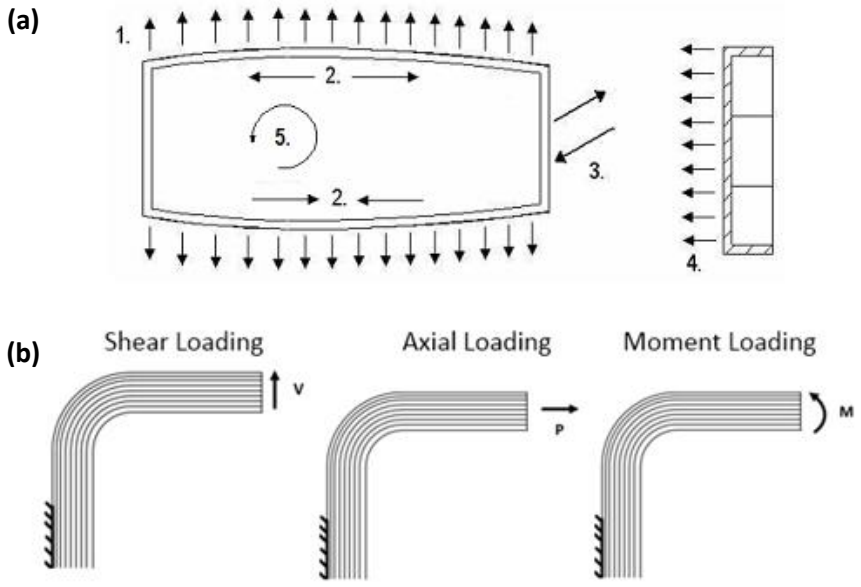

Figure 1.14 (a) Types of loads applied on a typical rib box structure; (b) reaction forces on the curved section of the composite laminate [24]

1.4.3. Failure mechanisms of curved composite laminates

Advances in manufacturing capabilities of composite laminates increase the trend in usage of complex geometries such as curved composite laminates as load carrying members. These laminated composite structures have a loaded curved region [32]. Due to laminated nature of these composite materials, the failure mechanisms differ from metals. Moreover, curved structural geometries introduce failure mechanisms not encountered in flat laminates [26]. Static and fatigue loads, which were explained in section 1.4.2, cause different failure modes. The failure of composite laminates under fatigue loading is usually characterized by a combination of various damage modes such as delamination, matrix cracking, debonding, ply failure, and fiber breakage [37]. Due to the low through-the-thickness strength of these laminates the primary failure mode is delamination [27]. Delamination is the separation along the interfaces of the layers. The delamination growth generally occurs in combination with the other failure modes, especially matrix cracking in off-axis plies [28]. The early stage of damage development is dominated by cracking of the matrix along fibers in plies that are not aligned with the principal tensile loading direction leading to delamination failure [38].

Delamination occurs due to high interlaminar stresses, which arise from material discontinuities, geometric discontinuities or eccentricities in the load path. Curved composite laminates consist of all of these interlaminar stress sources. Mostly the composite laminates are multidirectional and the difference in material properties between adjacent plies of different orientations also cause singular stresses at the free edges which initiates edge delaminations. Delaminations at the corner of the laminates may initiate due to interlaminar tensile or interlaminar shear stresses which cause radial stresses because of the curvature [27]. Delaminations may occur due to voids and errors formed during the manufacturing process too. **Figure 1.15** presents structural configurations and variable damage modes for curved composite laminates.

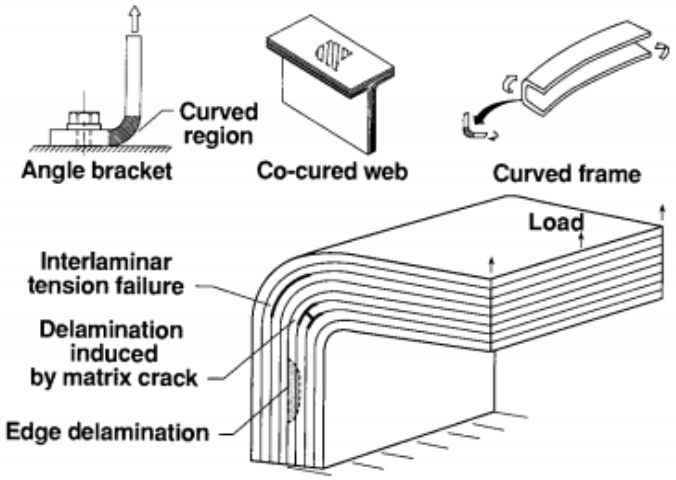

Figure 1.15 Curved composite laminate configurations and failure modes [27]

The curved region of the laminate is considered as a fatigue critical location. Delamination initiation and propagation occur in combination of the three fracture modes: Mode-I, Mode-II and Mode-III, as shown in **Figure 1.16**. Mode-I represents the opening mode of the crack faces, Mode-II is the sliding mode and Mode-III corresponds to the tearing mode deformation [28]. In order to understand the characterization of the delamination, complete mix-mode failure analysis have to be conducted.

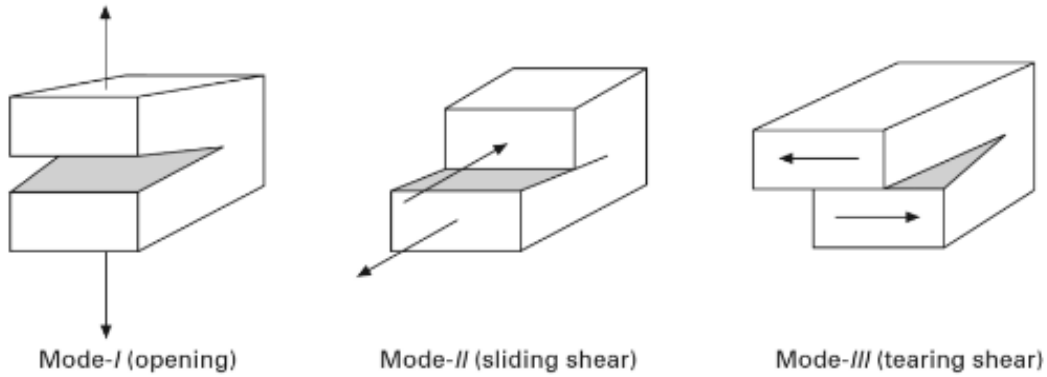

Figure 1.16 The three modes of fracture [28]

Interlaminar tensile (ILT) strength/through-the-thickness strength is generally lower than the interlaminar shear strength. Hence, through the thickness strength designates the strength of curved laminate [27]. Repeated loads create less interlaminar stress states than static cases and result in delamination initiation and propagation under lower stresses. Consequently, the interlaminar tensile (ILT) fatigue properties are the weakest link of curved composite laminates subjected to cyclic loading [34]. In order to understand the complete life behavior of curved composite laminates it is required to determine not only the curved beam strength and failure behavior under static loads but also the its fatigue properties.

1.5. Scope of the study

In modern aerospace and wind turbine industry, carbon fiber reinforced polymers are used widely. In order to obtain higher stiffness and strength, and also to provide lower weight, composites are preferred over metals. Besides superior specific strength and specific stiffness, composites have many distinguished properties, such as fatigue resistance. On the other hand, the failure mechanisms of composite materials are different and more complex than those of metals. In-plane properties of composite laminates are excellent. In contrast, their out-of-plane properties are relatively weaker. Material discontinuities and curved geometry creates interlaminar stresses causing matrix cracking in off-axis plies and delamination. In the fiber direction composite laminates demonstrate great fatigue resistance. However, fatigue properties in

through-the-thickness direction are the weakest point of curved composite laminates. The damage modes occurred under fatigue loading cause changes in material properties, affecting residual strength, stiffness and lifetime. By measuring these changes, it is possible to obtain an estimation of the damage in composite laminates [37].

The main application of composite laminates in airplane structures is for load carrying members, typically in the form of curved geometries located in the wing box structure. The L-shape brackets of A380 wings are an important example of fatigue damage in curved composite laminates. In 2012, Airbus confirmed that cracks had been found in L-shape brackets in the wings which were made of plastic based composites [29]. Fatigue crack growth in these curved composite laminates located in young planes occurred earlier than expected. Hence, it is vital to provide complete understanding about fatigue behavior of curved composite laminates made of CFRPs to improve their performance by extending both their reliability and service life.

In this study, the major objective is to analyze the fatigue behavior of curved CFRP laminates and compare it with the static failure. In this scope, the failure process of curved laminates with different stacking sequences is investigated under bending moment. Delamination onset cycles under various stresses are recorded. The stiffness reduction of curved laminates is observed through the cycles. Therefore, failure mechanisms are compared under fatigue and static loading.

In chapter 1, the application of composite laminates in aerospace and wind turbine industries is briefly introduced. Fatigue behavior of composites are discussed and compared with fatigue properties of conventional metals. Curved composite laminate applications in aircraft wings and repetitive flight loads on these laminates are explained. Failure modes of curved composite laminates under static and fatigue loading are mentioned in detail. In chapter 2, previous literature studies on damage process of composite laminates, and specifically on curved composite laminates, both under static and fatigue loading, are commented. Chapter 3 explains in detail the experimental procedure, including material and manufacturing process, fixture design, experimental setup and measuring techniques. Chapter 4 presents the results obtained from the experiments for three different lay-ups under static and fatigue loading. Static and fatigue failure mechanisms are discussed briefly for three different lay-ups. In chapter 5, the damage mechanisms are compared for different lay-up orientations under static loading. The difference between static and fatigue failure mechanisms for lay-ups are discussed. Finally, the effects of defects are presented.

Chapter 2

LITERATURE RESEARCH

In literature, there are many studies for fatigue damage progression on composite laminates and also on the characterization of curved composite laminates under both static and fatigue loading. In this chapter, these studies about composite laminates are discussed briefly in chronological order.

2.1. Fatigue damage progression of composite laminates

Talreja (1986) focused on two damage modes in composite laminates namely, intralaminar damage (matrix cracking) and the interlaminar damage (interior delamination) in the paper ‘Stiffness Properties of Composite Laminates with Matrix Cracking and Interior Delamination’. In this study, the deformational response of the composite laminates to mechanical loads were considered. With this aim, a representative volume element about material point, containing intralaminar cracking was constructed (**Figure 2.1a**). **Figure 2.1b** represents the volume element for interlaminar cracking corresponding to interior delamination. Of a composite laminate. An interlaminar layer was displayed to show the presence of interior delamination. Using these volume elements, vectorial representation of two types of damages were defined and relationship between the overall stiffness properties and the damage in the individual modes were derived from a phenomenological theory.

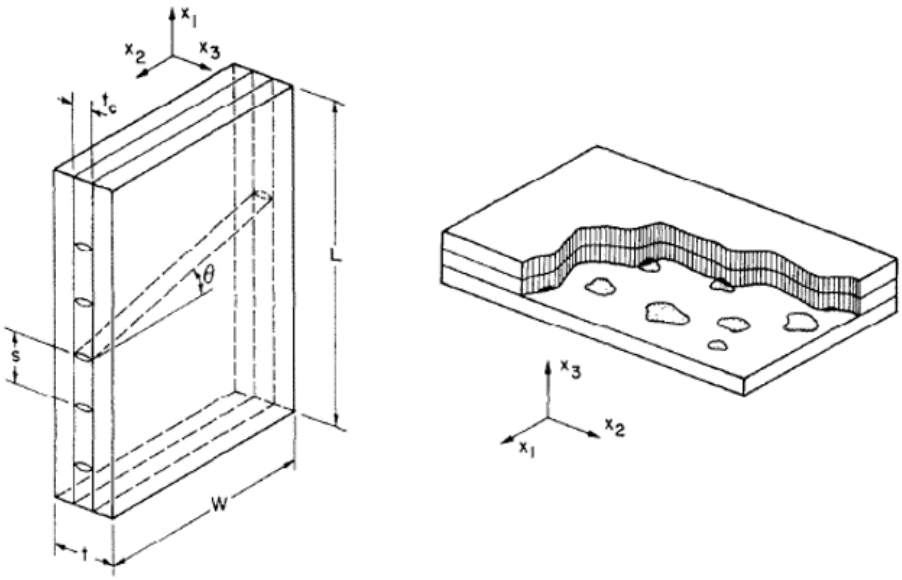

Figure 2.1 Representative volume element of a composite laminate having (a) Intralaminar cracking; (b) Interlaminar cracking [38]

The calculated relationships showed that the matrix cracking reduced all elastic modulus and changed the initial orthotropic symmetry of a laminate. However, the interlaminar damage did not change the symmetry but reduced the elastic modulus as well. Complete understanding of the damage evolution and changes in the deformational response of the material corresponded to not only the properties in the longitudinal direction but the changes in all stiffness coefficients. The determination of changes in the engineering modulus required knowledge of the phenomenological material constants for intralaminar cracks. Consequently, the required phenomenological constants were determined analytically. These constants were used in the derived stiffness-damage relations and elastic modulus degradation was predicted, then compared with the experimental results as shown in **Figure 2.2a** and **Figure 2.2b**. The results of predictions and the experiments were in good agreement. It was stated that, these modulus degradation typically occurred in the first stage of fatigue damage. A theoretical work was conducted on the effect of interlaminar cracking to the elastic modulus. Significant stiffness degradation was predicted in the second stage of the fatigue damage dominated by interior delaminations. However, the effect of this cracking mode on stiffness properties was not evaluated experimentally [38].

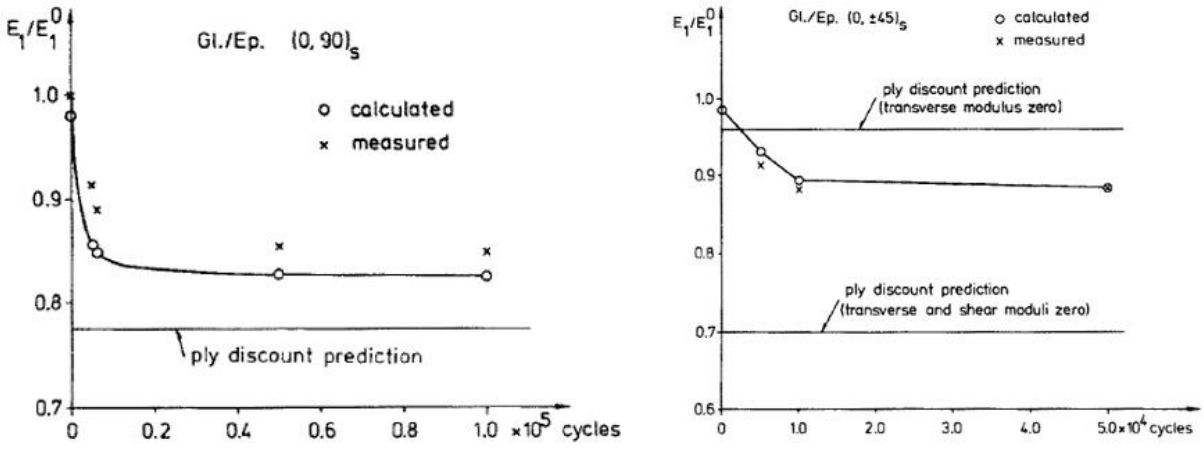

Figure 2.2 Variation of the longitudinal Young's modulus under tensile fatigue loading (a) $[0,90]_s$ glass epoxy laminate; (b) $[0, +45]_s$ glass epoxy laminate [38]

Whitworth (2000) conducted a study on stiffness degradation of composite laminates under fatigue loading in the paper 'Stiffness Degradation Model for Composite Laminates under Fatigue Loading'. In this study a model to predict stiffness degradation was proposed and its validity was evaluated. With this aim, AS4/3501-6 graphite/epoxy unnotched laminates were subjected to tensile and fatigue loading. Tensile tests were performed to the specimens in order to determine the ultimate strength and the initial stiffness of the material. Fatigue tests were conducted under load control and tension-tension cyclic load at R-ratio of 0.1 and at 10 Hz. In the fatigue experiments, specimens were subjected to ten different stress level ranging from 40 to 80 % of the initial strength. Strain was measured during the fatigue experiments. From the results, stress-strain data were obtained and stiffness values changing with the cycles were acquired.

Applied stress was calculated with the strain value corresponding to different cycles and modulus reduction ratio (MRR) was obtained analytically. All data and parameters obtained from experiments were used to predict the statistical distribution of the MRR at any applied stress level. **Figure 2.3** shows the prediction and the experimental results of MRR. There was a good agreement between the model and the experiments. The accuracy improved with increasing cycles due to rapid stiffness loss occurrence in the early cycles [30].

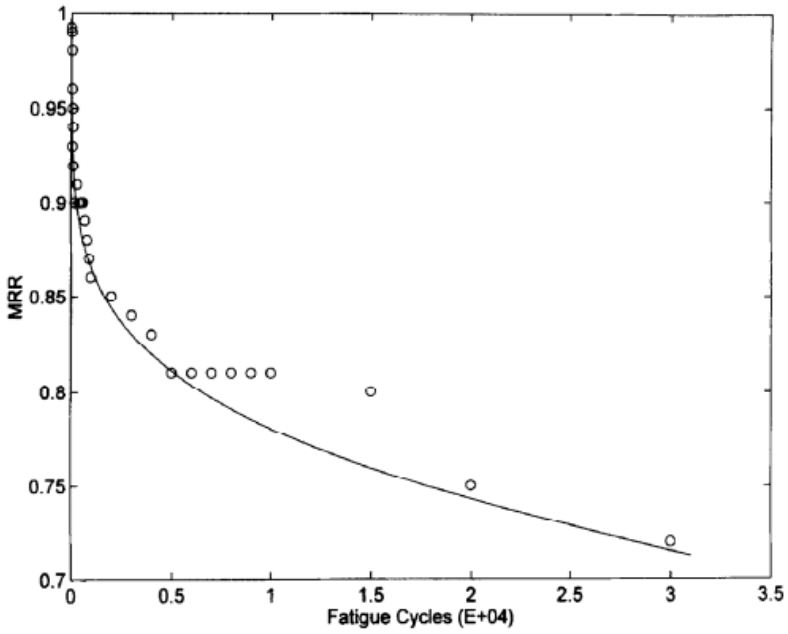

Figure 2.3 Stiffness degradation model and experimental data [30]

In the paper 'Damage Evolution under Multiaxial Cyclic Stress State: A Comparative Analysis between Glass/Epoxy Tubes and Laminates', Quaresimin et al. (2014) investigated the damage initiation and evolution in laminates under cyclic loading experimentally. The multiaxial fatigue behavior of composite materials was focused since its extreme importance and interest for many industrial fields. It was stated that multiaxial state occurred due to external loads in several direction or material anisotropy. In order to investigate these phenomena, off-axis flat specimens would be used to achieve internal multiaxial loading conditions, whereas external multiaxiality could be applied using tubular or cruciform specimens. Tubular specimens were designed in order to understand the effect of σ_2 and σ_6 on the number of cycles before the initiation of a transverse crack. With this aim tubular specimens with 90˚ fibers with respect to the tube axis were manufactured and exposed to tension-torsion cyclic loading with different λ_{12}, biaxiality ratio values which were the ratio of σ_6 to σ_2. Since these specimens were made of UD 0° laminates, the specimens experienced the final failure without allowing analyzing the cyclic crack propagation phase.

It would be easier and cheaper to test multiaxial fatigue behavior of composite with off-axis loaded UD 0° specimens using the material anisotropy. UD 0° specimen configuration did not allow focusing on analyzing the crack propagation phase as well. Constraining off-axis plies was required to observe the propagation of matrix cracks. With this aim, E-glass/epoxy pre-preg UE400-REM was produced in a $[0/\theta_2/0/-\theta_2]$ lay-up orientation with θ=50˚ and θ=60˚ configurations. Plies with 50˚ and 60˚ fiber orientations referred to thick and thin layers, respectively which resulted in $t_{lay-up}^{\theta=50^\circ}$=4.5 and $t_{lay-up}^{\theta=60^\circ}$=4.3 mm. Uniaxial fatigue tests were performed on the cured flat laminates using hydraulic test machine. Glass/epoxy laminates were semi-

transparent and crack propagation was observed using uniform distributed light source. The experimental setup is shown in **Figure 2.4a**. Cyclic loads were applied with 3-5 Hz frequency and at an R-ratio of 0.1 where $R=P_{min}/P_{max}$. P_{max} value was set for strain values in the range of 0.4% and 1.1% of the maximum strain. As the stiffness of the specimens decreased with the cycles due to damage evolution the applied load was constant while the strain values increased.

As expected, the first crack initiation was followed by multiple onsets through the whole specimen as shown in **Figure 2.4b**. The cycle of delamination onset was recorded for variable σ_{max} and SN curve was generated. Crack propagation was analyzed and crack locations was found to be far enough that the cycles spent for each crack onset could be considered as independent fatigue results. The increase in crack density in the off-axis plies led to the stiffness degradation of the test specimens. It was easily observed that stiffness reduction in earlier fatigue lifer was strongly dependent on the load level.

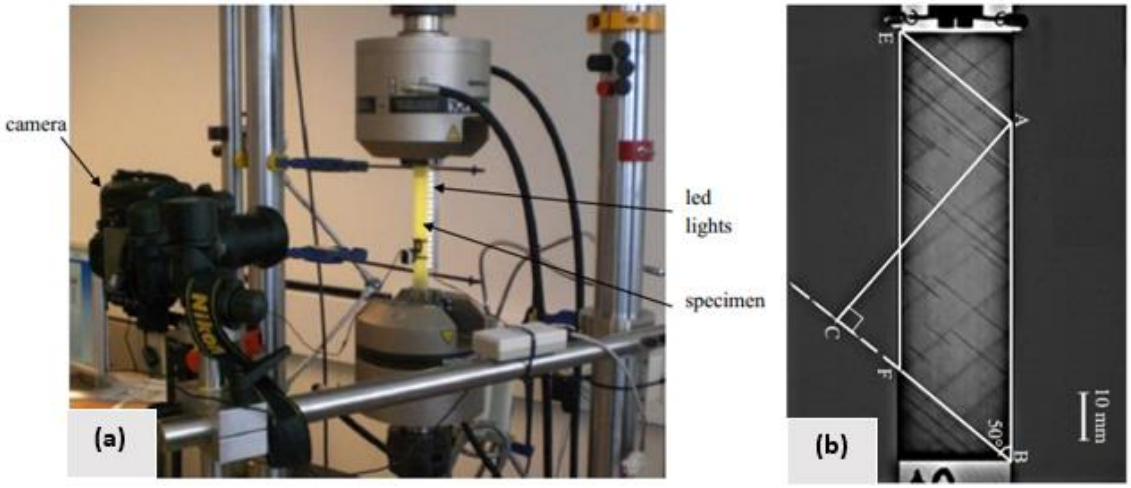

Figure 2.4 (a) Fatigue experimental setup; (b) Damage occurred on flat specimens under fatigue loading [29]

In order to analyze the crack propagation stage in detail, Energy Release Rate (G) was calculated for the crack propagation in the ±θ layers. G was computed for both thick and thin layers. G had an increasing trend for short cracks but it reached a steady-state (SS) value when the crack length extended twice the layer thickness. It was stated that crack growth occurred in a SS condition for the most of the propagation phase. It was expected that crack growth rate remained constant with the constant ERR but local toughness due to defects corrupted the steady-state crack growth rate. It was concluded that SS G was the driving force for the propagation of the cracks for a given mode mixity. Alternatively, steady-state G was calculated analytically by energy accounting. It was found that the difference in SS growth rates of cracks could be understood by scaling the SS G with ply thickness. Hence, it was suggested to obtain fatigue crack growth rate data experimentally for a single ply thickness only and use these data to predict the crack growth rate for all other ply thicknesses.

The SN data of the tubular specimens under external multiaxial loading were compared to the flat multidirectional laminates tested under axial loading under various biaxiality ratios. It was observed that the results were reasonably consistent and the fatigue damage evolution was basically the same which resulted that the local multiaxial stress state described in terms of biaxiality ratios was similar [29].

2.2. Damage mechanisms of curved composite laminates

Delamination failure in a UD curved composite laminates was investigated numerically and experimentally in the paper 'Delamination Failure in a Unidirectional Curved Composite Laminate" by Martin (1992). It was stated that delamination was the primary failure mode of composites due to their low through-the-thickness properties. This study aimed to predict the maximum load which a unidirectional curved laminate could sustain without any damage. With this aim, simple right-angled 24-ply graphite/epoxy (AS4/3501-6) UD laminates were manufactured. Double cantilever beam (DCB) specimens were also manufactured with 24-ply and [0] UD fibers, as well. Flat specimens were produced also, in order to determine elastic properties of materials. The fracture toughness value, G_{Ic}, was obtained with DCB specimens and the elastic tensile and shear properties were measured using ASTM standards. The fixture for testing the curved composite laminates is shown in **Figure 2.5a**. Load was applied to the specimen at a distance L of 50 mm from the curved region by a hinge, clamped to the specimen. The other leave of the hinge is clamped to the fixture which consisted of a clamp free to pivot. The laminates were loaded quasi-statically under load control and load-displacement data were monitored in order to determine the failure load. The maximum load per unit width and the first delamination location was tabulated in the results. The damage evaluation of the specimens is shown in **Figure 2.5b**. Damage initiated as a single delamination around the curved region in which 46-49% of total thickness and extended through the arm and the leg. Final failure corresponded to delamination at different locations through the thickness of the curved region with the loss of all bending stiffness of the specimen as shown in **Figure 2.5b** (bottom).

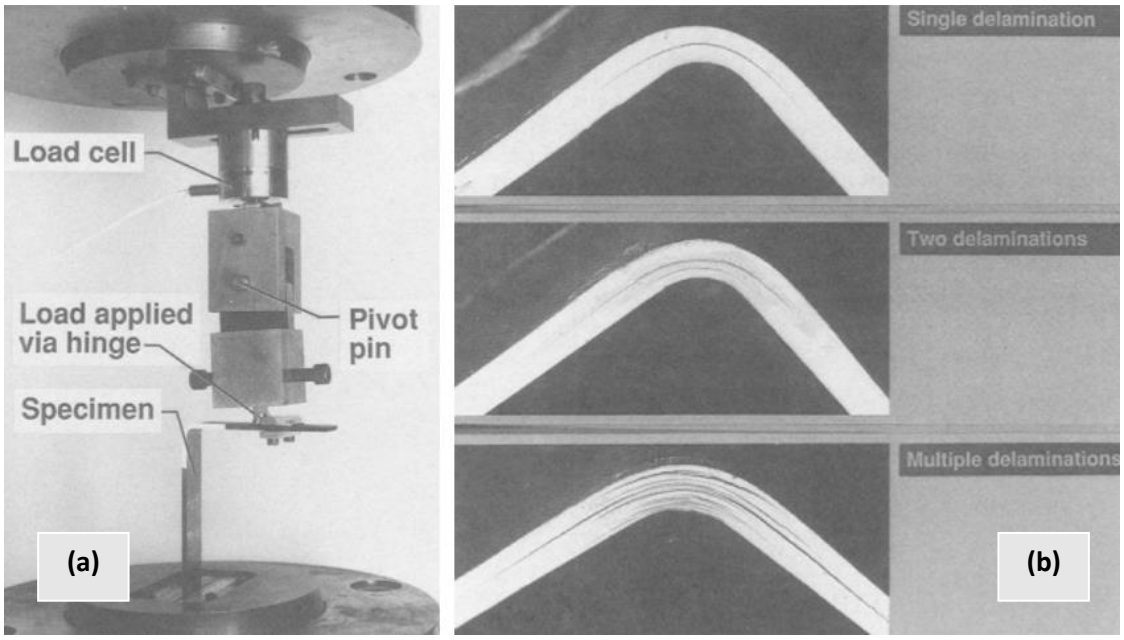

Figure 2.5 (a) Loading fixture; (b) Damage evolution in UD composites [27]

Analyses were conducted in order to characterize the onset and growth of the delamination of the curved composite laminates. The location of the highest radial stress was determined using a closed form elasticity solution for anisotropic curved beam. This was used to determine the mesh refinement location in FEA. 2D FEA was conducted to verify the beam solution and determine the variation of G with delamination growth. Elastic tensile and shear properties were used in FEA and radial, transverse shear and tangential stresses were calculated. The highest radial stress was located in 42% of the thickness. The results slowed that the transverse shear stress was almost negligible so that the failure was dominated by the radial stress. In order to predict failure loads for the onset of the first delamination, a failure damage criterion was obtained using stress analysis.

The total and individual mode values for the energy release rate (G) were obtained analytically. It was stated that the delamination was dominated by Mode I around the curved region. Energy release rate tendency was the same for both right and left crack tips but the magnitudes was different Mode II energy release rate volume explained these differences. Consequently, the delamination grew individually in both arms. Simultaneous crack growths occurred as well and only some explanations were made under same assumptions. Then, a G criterion was developed. If G value was 2% greater at one delamination front than the other, then growth would occur in that direction only. If the difference was less than %2, the delamination would grow in both directions equally [27].

Jackson and Martin (1993) proposed a technique to determine interlaminar tensile strength, σ_3 of the fiber reinforced composites using curved beam laminates in the paper ‘Interlaminar Tensile Strength Specimen’ the curved beam specimens used in the experiments were [0] UD laminates with various width, inner radii, loading arm

lengths and thicknesses namely, 16, 24, 48 plies. The material was AS/3501-6 carbon/epoxy. Initially aluminum hinges were bonded to the tips of the specimens and load was applied through the hinges. However, high loads caused bend or break of the hinges. Thus, loads were applied through a steel loading fixture (**Figure 2.6**) which allowed conducting the experiment in the universal test machine. Experiments were carried out under displacement control with the rate of 0.5 mm/min. load displacement curve was recorded and the initial laminar tension failure coincided with the sudden decrease in load. In order to observe the failure easily, the curved region of the laminates were painted to white.

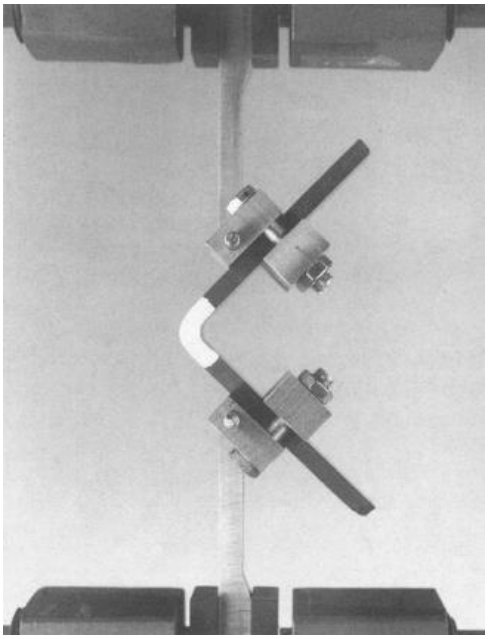

Figure 2.6 Loading fixture and the specimen [31]

Lekhnitskii solution for a curved beam and beam theory were conducted to determine the radial stresses. Finite element analyses were used to determine the stress state of the laminates, as well. The radial and tangential stress distributions calculated numerically and analytically are shown for 3 mm thick laminate in **Figure 2.7**. Shear stresses were considered as negligible and radial stress increased from zero and varied from tension to compression as the radius increased. The radial stress was maximum at 0.4 of the thickness of the laminates. The failure was dominated by the radial stress alone.

In the experiments, subcritical damages observed before the catastrophic load drop occurred which corresponded to small load drops resulted in steps the plots. The wider specimens experienced more steps until failure. Failure occurred at the load value which is twice more than the initial damage loads. During the failure the load often drop by 40%. **Figure 2.8a** plots the load displacement of curved laminates with different thicknesses. After failure, circumferential cracks were formed at the curved region. **Figure 2.8b** shows an example of crack existed after failure.

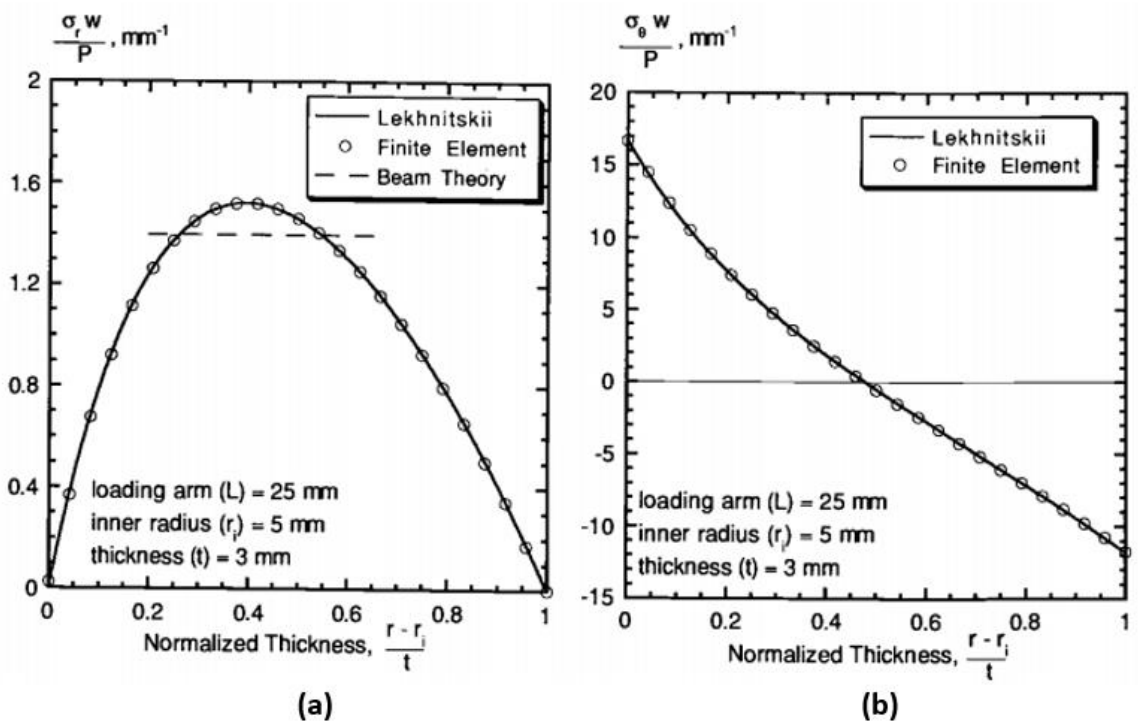

Figure 2.7 FEA results with analytic results (a) Radial stress distribution; (b) Tangential stress distribution [31]

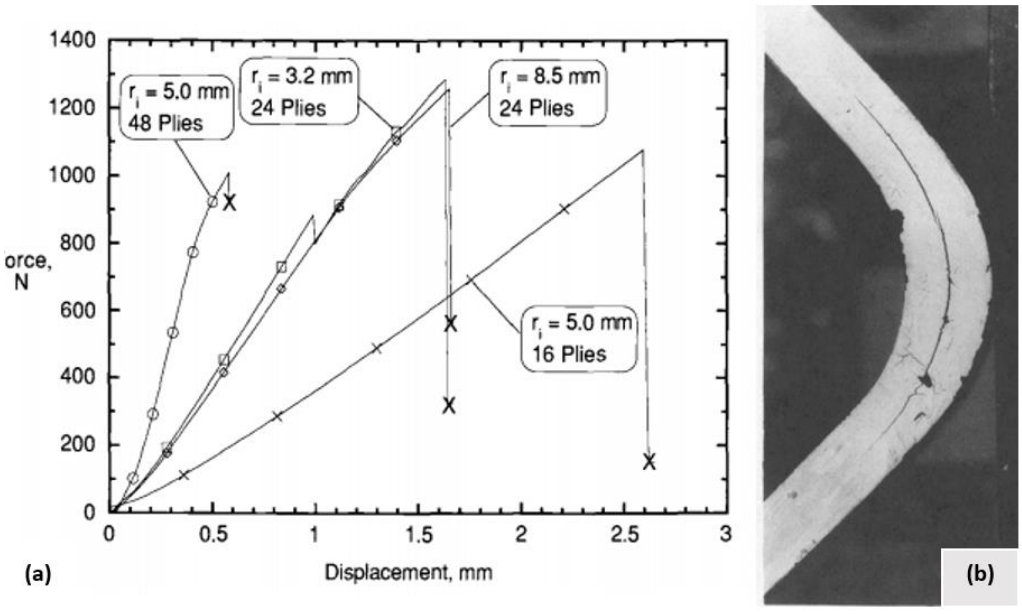

Figure 2.8 (a) Typical load displacement curves; (b) Delamination occurred in the curved region after failure [31]

The radial stress reaches the maximum at single point through the thickness which had the same value through the width. So, it was expected reduction of width to reduce the probability of flaws and give higher strength. However, σ_3 values were very similar

in narrow and wide specimens. Therefore, width had almost no effects on σ_{3c}. As laminates got thicker, a larger volume was under stress and the probability of flaw existence was higher. It was expected that thicker laminates have lower σ_{3c}, if all of the specimens with various thickness had the same manufacturing quality. However, the thinnest specimen with 16 plies had the best quality and the highest strength, whereas the 48-ply specimens with poor quality had the lowest strength. Consequently, strength decreased with the increasing thickness related to laminate quality which caused differences in failure mechanisms. Therefore, interlaminar tensile strengths were highly dependent on the manufacturing quality of the specimens and the thickness effect could not be determined [31].

Martin and Jackson (1993) conducted experimental and analytic work required to predict damage progress in a curved cross-plied laminates under static and fatigue loading in the paper 'Damage Prediction in Cross-Plied Curved Composite Laminates'. In the experimental part of the study, all specimens were fabricated from Hercules AS4/3501-6 graphite/epoxy. First, flat 90º, UD, 24-ply specimen were manufactured and subjected static and fatigue tests until the failure occurred. The fatigue tests were conducted under load control, R-ratio equals to 0.1 and at a frequency of 5 Hz. The static failure load and cycle to delamination onset under fatigue loading were recorded.

In the next step, interlaminar tension strength tests were conducted using 0 UD, 24-ply curved laminates. The static failure loads were taken from the study of Martin 'Delamination Failure in Unidirectional Curved Composite Laminates'. Fatigue tests were conducted using the same fixture and test machine in that study (**Figure 2.5a**), under load control and at an R-ratio of 0.1 and frequency of 5 Hz. The number of cycles to the delamination onset was noted which also corresponded to a rapid loss of bending stiffness of the curved region causing opening. Analytically σ_{3max} was calculated and a σ_{3max} vs cycles to delamination onset graph was plotted.

Double cantilever beam (DCB) tests were conducted in order to determine the Mode-I static and fatigue fracture toughness of the material. The laminate configuration was 24-ply and [0] UD. The static and fatigue DCB tests were carried out under displacement control. During fatigue tests various maximum displacements were applied at an R-ratio of 0.1 and 5 Hz frequency. With static tests, fracture toughness, G_{Ic} was determined and cycles to delamination onset values were recorded under fatigue load. Crack was assumed to grow if maximum load decreased 1%. Maximum strain energy release rate (G_{Imax}) value calculated analytically and a G_{Imax} vs cycle to delamination onset curve was plotted.

In the last step, cross-plied curved laminates were tested under static and fatigue load. Two different layups were used in tests namely, $[0_4/90_3/0_5]_s$, (Lay-up A) and $[0_3/90_3/0/90_2/0_2]_s$, (Lay-up B). These lay-ups were chosen because matrix crack would occur in the tension loaded off-axis plies and delamination would grow from matrix cracking. In both static and fatigue tests, the first crack sound corresponded to the

delamination leading to complete loss of stiffness. As shown in **Figure 2.9a,** an oblique matrix crack occurred in the tension loaded $[90]_3$ plies and interlaminar tension failure occurred in the 0º plies of Lay-up A. Although it was not experimentally proved, it was thought that the matrix crack had occurred before the delamination. **Figure 2.9b** presents two matrix cracking formed in both $[90]_2$ and $[90]_3$ plies of Lay-up B. In analytic calculations, Lay-up A was chosen to be studied due to the second matrix crack formed in Lay-up B created complications. Hence, the maximum load per unit width vs cycles to delamination onset graph of Lay-up A was plotted.

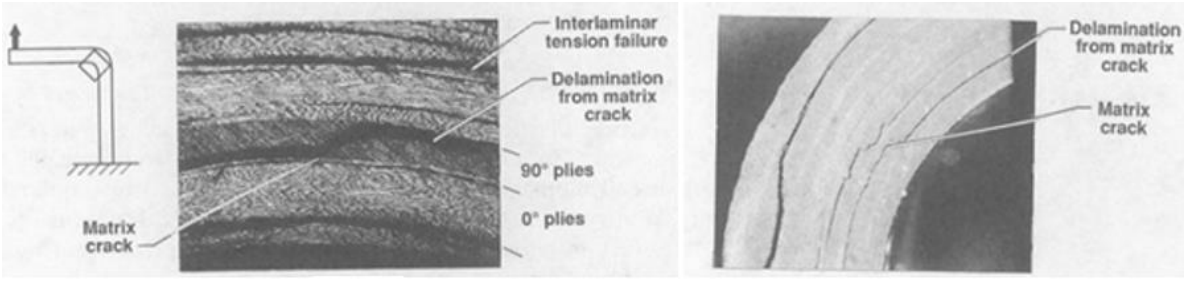

Figure 2.9 Damage in curved laminate (a) Lay-up A; (b) Lay-up B [32]

The stress analyses were conducted using closed-form analysis and compared with FEA results. Finite element model was used to determine the G distribution as well. A technique was used to characterize the path along curved region which consisted of comparing the values of G at each crack front and growing the delamination at the location of highest G. It was concluded that the strain energy release rate value (G) was highest at the inner right part of the curved region under previously described loading. Predictions of damage onset from radial stresses, transverse ply cracking and delamination onset from matrix cracking were made using analytic methods. As a discussion, due to the matrix cracking and interface effects at free edges, multidirectional laminates should not be used to determine interlaminar tensile strength, unless it is certain that ILT failure occurs within a group of plies of the same orientation. Matrix cracks would be avoided by preferring lay-ups to reduce tangential stresses in 90º plies. Free-edge delaminations could be minimized with lay-up configuration resulting low radial stresses between 0/90 interface [32].

In the paper, 'Interlaminar Tension Strength of Graphite/Epoxy Composite Laminates' written by Shivakumar, Allen and Avva (1994), a tension loading fixture were proposed to measure the interlaminar tension strength of L-shaped curved beam laminated textile composites. The curved specimens had equal legs and three different thicknesses, 16, 24, 32 plies (**Figure 2.10a**) were tested. The material is the AS4/3501-6 graphite/epoxy composite. A special load fixture was designed to test the specimens in a standard tension test machine. **Figure 2.10b** shows the illustration of the specimen attachment and the load case. The specimen and the loading fixture assembly as shown in Figure 2.10c were mounted on a servo-hydraulically controlled tension test

machine. Tests were conducted under displacement controlled at 1 mm/min. A sudden decrease in load was observed when the interlaminar tension failure load which was used in calculating interlaminar tensile strength and the data was recorded. Delamination corresponding to loss of stiffness occurred near mid-thickness (**Figure 2.11**) where the transverse tension stress was higher.

2D FE analysis were conducted and modified Lekhnitskii and beam theory equations were used for calculating stress field of curved beam laminates. Calculated radial and tangential stresses from various analyses were compared with each other. Calculated maximum radial stresses corresponded to interlaminar tensile strength of the specimens. The delamination initiation site agreed with the calculated maximum interlaminar tension stress locations. Interlaminar tensile strength decreased with increasing specimen thickness. The decrease in the strength with thickness was because of high probability of having more number and larger size of defects in a large volume of materials [33].

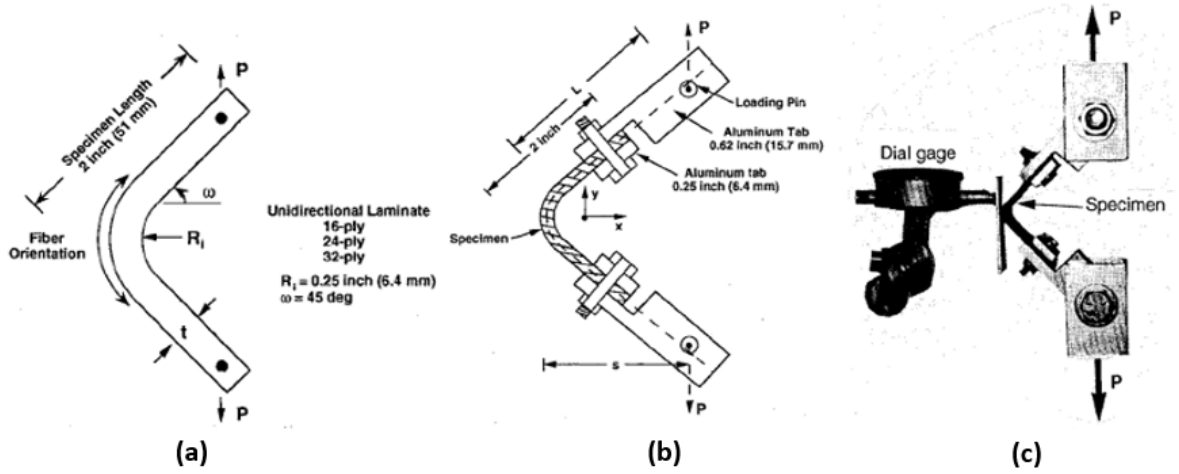

Figure 2.10 (a) Specimen configuration; (b) Illustration of loading fixture; (c) Specimen and the loading fixture [33]

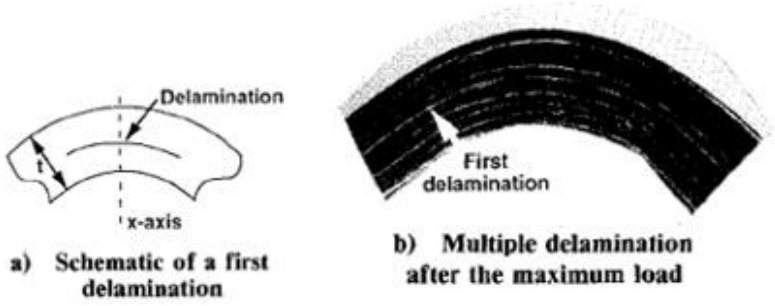

Figure 2.11 Single and multiple delaminations [33]

In the paper 'Effects of Defects on Interlaminar Tensile Fatigue Behavior of Carbon/Epoxy Composites', Seon et al. (2013) conducted a work on a methodology for accurate evaluation of the effects of porosity defects on the interlaminar tensile (ILT) fatigue behavior of carbon/epoxy composite materials. It was focused on this

phenomenon since these composite materials would be used in aircraft as fatigue critical elements and ILT fatigue properties could be the weakest link of a laminated composited subjected to cyclic loading. In the experiments, 36-ply thick IM7/8552 UD curved beam laminates were manufactured appropriate for ASTM D6415 standards. 4-point bending test fixture (**Figure 2.12a**) was used to obtain interlaminar tensile stress with ASTM D6415 standards. The test fixture was placed in a uniaxial servo-hydraulic test machine and subjected to cyclic loading under load control at R-ratio of 0.1 and 5 Hz frequency until delamination failure. Delamination initiated at the curved region and suddenly propagated to the arms.

FEA were conducted in order to obtain the maximum ILT stress. The highest ILT stress was found to occur at about two third of the specimen thickness. However, after failure the location of the delaminations and the cycles to delamination onset under the same load were not consistent among the specimens and did not coincide with the highest ILT stress location. CT scans of the specimens with fatigue damage were taken and it was observed that delaminations started from voids presents in critical locations of the specimens (**Figure 2.12b**). ILT SN curve was generated for the specimens consist of voids. A finite element model was created with voids in critical locations and refined stress calculations were made. In the last step, point-stress and average-stress methods were used in combination with SN curves generated from experiments and the FE model in order to obtain refined ILT SN curve for pristine carbon/epoxy laminates [34].

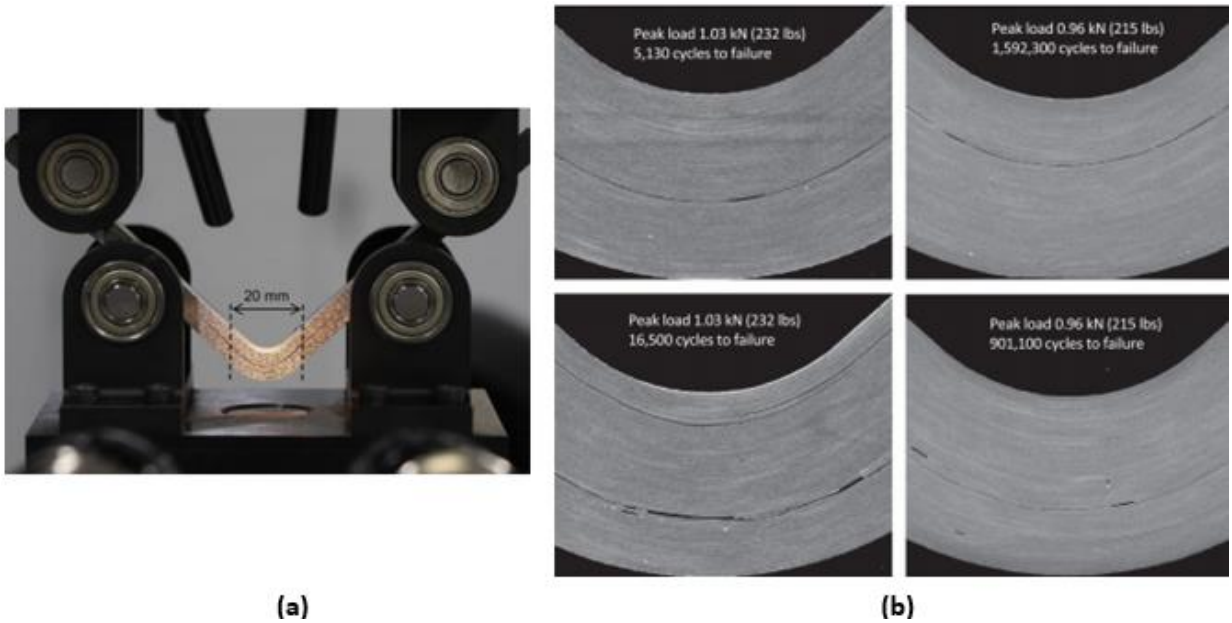

Figure 2.12 (a) 4-point bending test setup; (b) Examples of delaminations on fatigue test specimens [34]

The study, 'Fatigue Delamination Initiation in L-Bend CFRP Coupons', conducted by Blanchfield and Allegri (2014), focused on identifying the point of damage initiation in the curved carbon fiber laminate subjected to pure interlaminar tensile fatigue loading

in order to obtain SN curves for this material. Thick, 32-ply [0] UD curved laminates made of IM7/8552 pre-preg carbon/epoxy were used in the experiments. In order to obtain interlaminar tensile stress, 4-point bending test with ASTM D6415 test standards was carried out. Under quasi-static loading, catastrophic failure occurred suddenly, so that precise delamination initiation point could be observed easily. In order to observe the damage initiation point under fatigue loading, acoustic emission system was used for in-situ monitoring of the specimen. **Figure 2.13a** presents the experimental setup. Initially, CT (X-Ray) inspection was conducted on the specimens and it was confirmed that there were no voids, wrinkling or initial defects (**Figure 2.13b**). The fatigue tests were initially conducted under load control, however, the loss of stiffness led to an increase in crosshead displacement resulting in rapid failure. Consequently, fatigue tests were switched to displacement control in order to detect stiffness loss before the failure. It was stated using the acoustic emission data in combination with the compliance values from the test machine that under fatigue loading the failure occurred suddenly rather than gradually.

The static strength of the curved composite laminates was obtained from the static tests. CT scans of five specimens were taken after fatigue tests and no damage evidence was found as shown in **Figure 2.13c**. Thus, it was assumed that there was no delamination initiation leading to final failure. Hence, the point of damage initiation was accepted as failure. It was stated that failure occurs where the maximum radial stress arose at 40% of the through the thickness of the curved region. Full SN curves were generated from the fatigue tests and it showed that fatigue endurance increased with decreasing severity. This work had been conducted in order to develop a model to predict Mode-I fatigue delamination growth of this material [35].

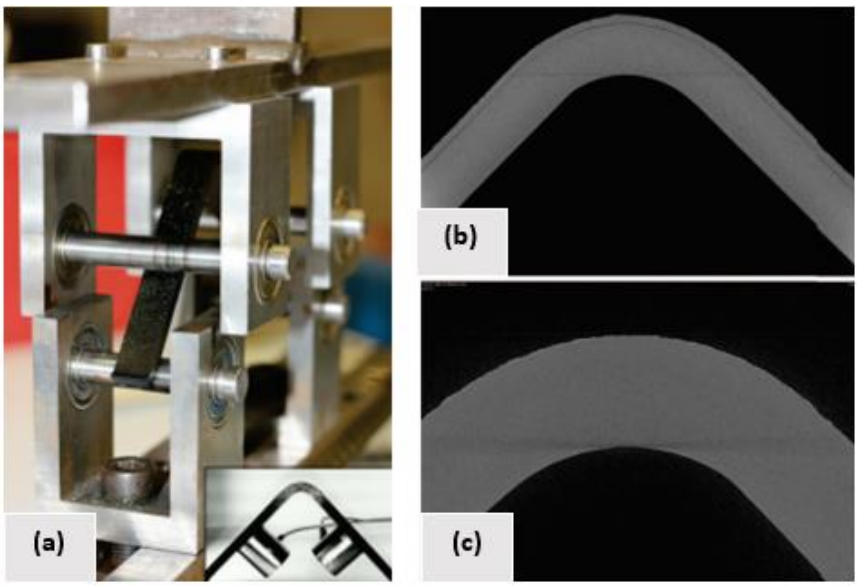

Figure 2.13 (a) Experimental setup; CT scan (a) Before test; (c) After fatigue test [35]

In the paper ‘Determination of The Out-of-Plane Tensile Strength Using Four-Point Bending Tests on Laminated L-Angle Specimens with Different Stacking Sequences

and Total Thicknesses', Charrier et al. (2015) focused on the out-of-plane tensile strength of curved beam carbon/epoxy laminates. 4-point bending test was conducted on curved composite specimens in order to obtain out-of plane properties of the material. The specimens were manufactured from T700GC/M21 UD pre-preg plies with different stacking sequences, arm length, width and thicknesses, namely 16, 32, 48 plies. The parameters such as the distances between the rollers of the test fixture were optimized for different specimens. The tests were performed under displacement control. Different measurement techniques were used to record the maximum displacement and load. **Figure 2.14** shows the specimens and the experimental setup. FEA were conducted in order to compare the stress state results with the experiments.

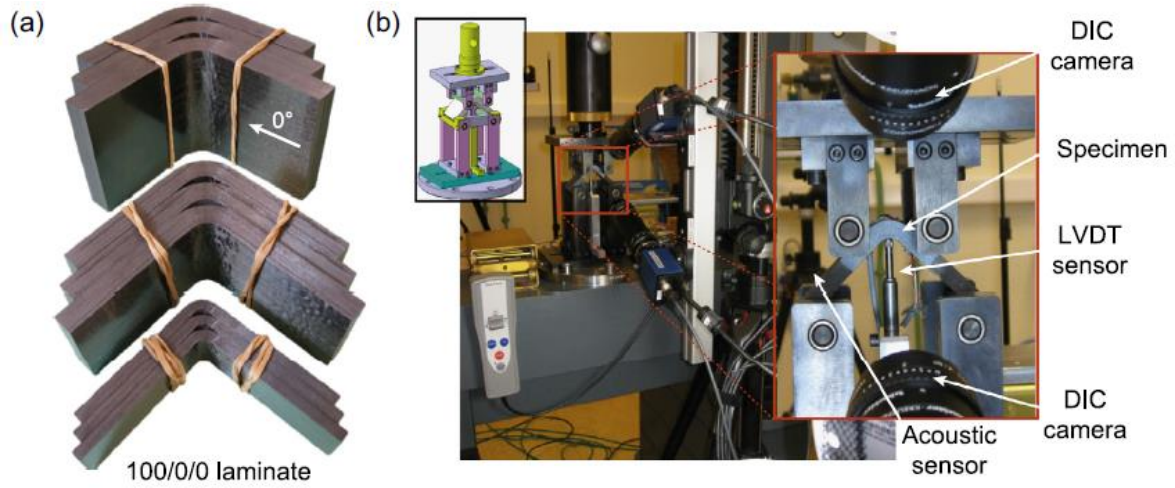

Figure 2.14 (a) Curved composite laminates; (b) Experimental device [36]

The damage initiated at the curved region of the specimens. The initiation and the propagation were instantaneous and leading to sudden decrease in stiffness. The influence of the stacking sequence, the thickness and the elastic properties were investigated. It was stated that the strength was independent of the stacking sequence and the thickness for 16 and 32 ply specimens. However, for 16-ply thick laminates the strength of the material seemed to be dependent on the stacking sequence in the analytic predictions. It was due to an erroneous estimation of the curved beam strength because curvature of the legs cannot be neglected. For 48-ply thick specimens the material strength was determined to be lower than thinner specimens with 16 and 32 ply. This phenomenon was due to a gradient in chemico-physical state of the material which existed due to non-optimal curing cycle for thick specimens. In order to prevent these differences in the experimental and analytic results, it was recommended to use FE simulations to determine out-of-plane tensile strength [36].

Chapter 3

METHODOLOGY

In this chapter the material and the experimental procedure are discussed. First of all, the material properties are introduced and the micro-structures of the laminates are shown. The manufacturing process of curved beams is then explained. Secondly, the specimen geometry and laminate properties are introduced. Then, digital microscopy and specimen preparation steps for the post-process analysis are presented. Finally, the experimental setup and the tension loading fixture are introduced. High speed camera and monitoring are explained as a part of experimental setup.

3.1. Material

In this study, two different lay-up orientation of composite laminates, [0] UD and cross-plied curved composite laminates have been used (**Table 3.1**). The first lay-up $[0]_{15s}$ UD specimen contains 30 plies, the stacking sequence of cross-plied laminates is $[0_3/90_3/0_3/90_3/0_3/90_3]_s$ and laminates contain 30 plies as well.

Table 3.1 Laminate orientation and pre-preg properties of the specimens

Laminate Orientation	Number of Plies	Material	Type
$[0]_{30}$	30	HexPly® AS4/8552	UD Pre-Preg
$[0_3/90_3/0_3/90_3/0_3]_s$	30	HexPly® AS4/8552	UD Pre-Preg

[0] UD lay-up consists of 30 plies of 0˚ positioned UD pre-pregs (**Figure 3.1a**). UD pre-pregs are laid through the thickness. HexPly® AS4/8552 UD carbon pre-pregs are used having 0.184 mm thickness. **Figure 3.1b** shows the micrographs of the side view of the laminates. It can be seen from the figure that UD pre-pregs are laid through the same direction. It is more difficult to hand lay-up UD pre-pregs to manufacture complex geometries, relative to fabric pre-pregs. This lay-up configuration is selected in order to investigate the behavior of the fiber dominated laminates.

The second lay-up is $[0_3/90_3/0_3/90_3/0_3]_s$, cross-plied laminates. It contains 30 plies (**Figure 3.2a**). HexPly® AS4/8552 UD carbon pre-pregs are used having 0.184 mm in thickness. Different lamina directions can be seen easily. Different orientations of pre-pregs create clear interfaces between the plies. Group of 0˚ and 90˚ of plies are laid up since group of plies act as a single ply and decrease the number of interface where delamination may occur [39]. Matrix cracking and delaminations occurring between the interfaces can be observed easier with this lay-up orientation. Cross-plied laminates

have these off-axis plies which provide investigating the behavior of matrix dominated laminates. **Figure 3.2b** presents the micrographs of the side view of cross-plied laminates and the different directions of the laminas. Lamina properties of unidirectional pre-pregs used in both lay-up orientations are shown in **Table 3.2**.

Table 3.2 Lamina properties of pre-pregs used in the specimens

	E_{11} (GPa)	E_{22} (GPa)	E_{33} (GPa)	ν_{13}	ν_{12}	ν_{23}	G_{12} (GPa)	G_{13} (GPa)	G_{23} (GPa)	ρ (gr/cm^3)
AS4/ 8552 UD	135	8.5	8.5	0.29	0.29	0.05	4.2	4.2	4.2	1.58

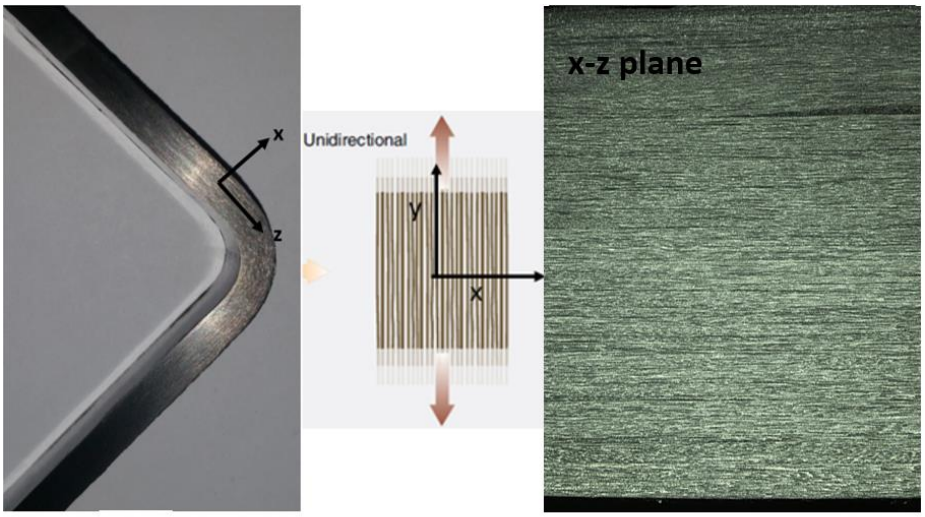

Figure 3.1 (a) [0] UD specimen showing in thickness plane; (b) Micrograph of the side view of [0] UD specimen

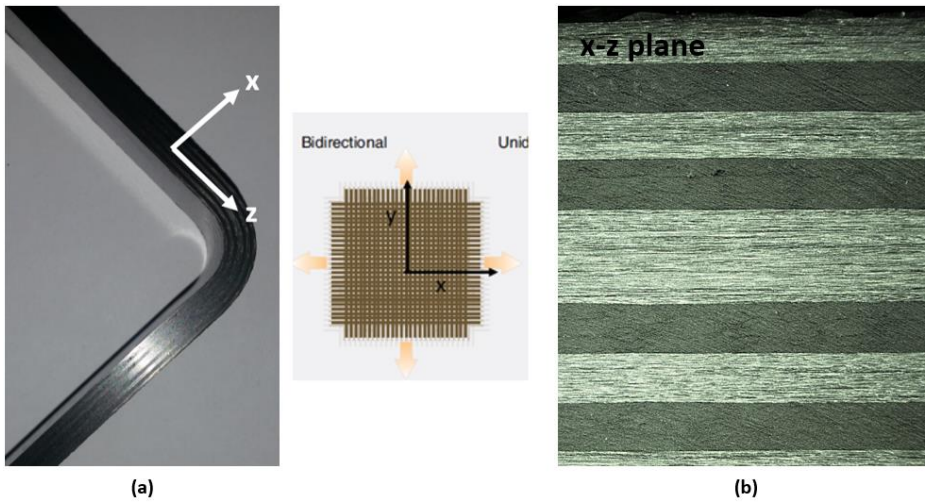

Figure 3.2 (a) Cross-plied specimen showing in thickness plane; (b) Micrograph of the side view of cross-plied specimen

3.2. Manufacturing process

Manufacturing of the L-shape laminates was carried out using hand lay-up with the vacuum bagging technique. Right angled male tool was used. Vacuum bagging for autoclave curing is the most common method in aerospace industry for manufacturing carbon fiber reinforced epoxy parts. **Figure 3.3** shows the simple schematic of the bagging system.

Pre-pregs were used as a starting material for vacuum bagging to save time and make easier the manufacturing process (**Figure 3.4a**). In order to prevent sticking, the tool was cleaned by polish before the lay-up process. Then, pre-pregs were laid up in the desired sequence and the orientation (**Figure 3.4b**). After the lay-up process was complete, the release fabric and bleeder papers were placed (**Figure 3.4c**). The bleeders were used to absorb excess quantity of epoxy during the vacuum bagging process. Finally, an impermeable nylon bagging was positioned with small holes to place vacuum gage ports (**Figure 3.4d**). A vacuum vent line and a pressure gage were mounted on these ports. The entire assembly was placed inside an autoclave for the curing process where the external pressure was applied to merge individual layers into a laminate [41]. The specimens were cured in autoclave for 8 hours minutes at 180 °C temperature and 6.9 bars pressure. In order to finish the procedure, the autoclave temperature was slowly decreased to room temperature, while the pressure was decreased gradually. The total autoclave curing process was approximately 10 hours. After the process, the cured curved composite laminates were cut into the desired dimensions (**Figure 3.4e**).

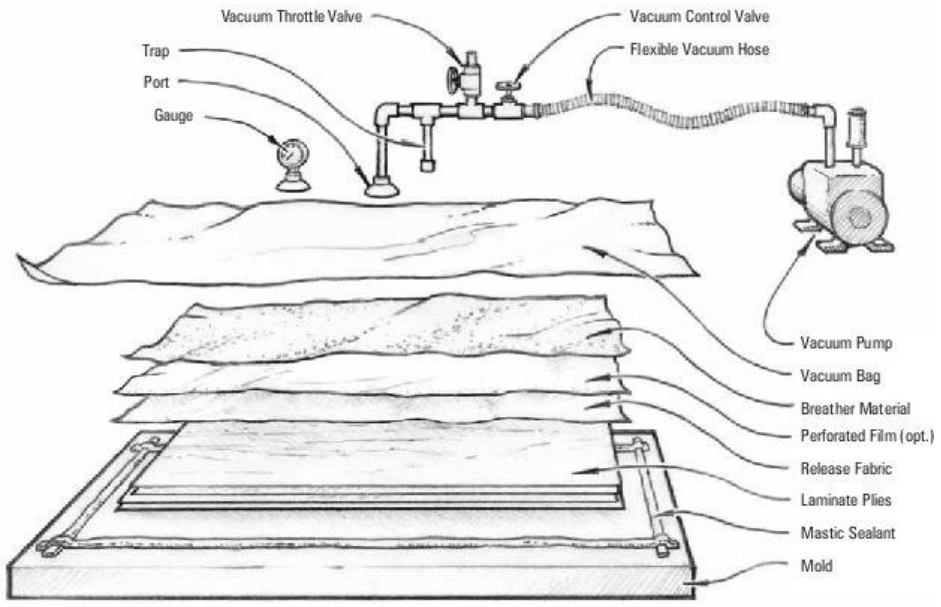

Figure 3.3 The illustration of hand lay-up manufacturing process of composite materials [42]

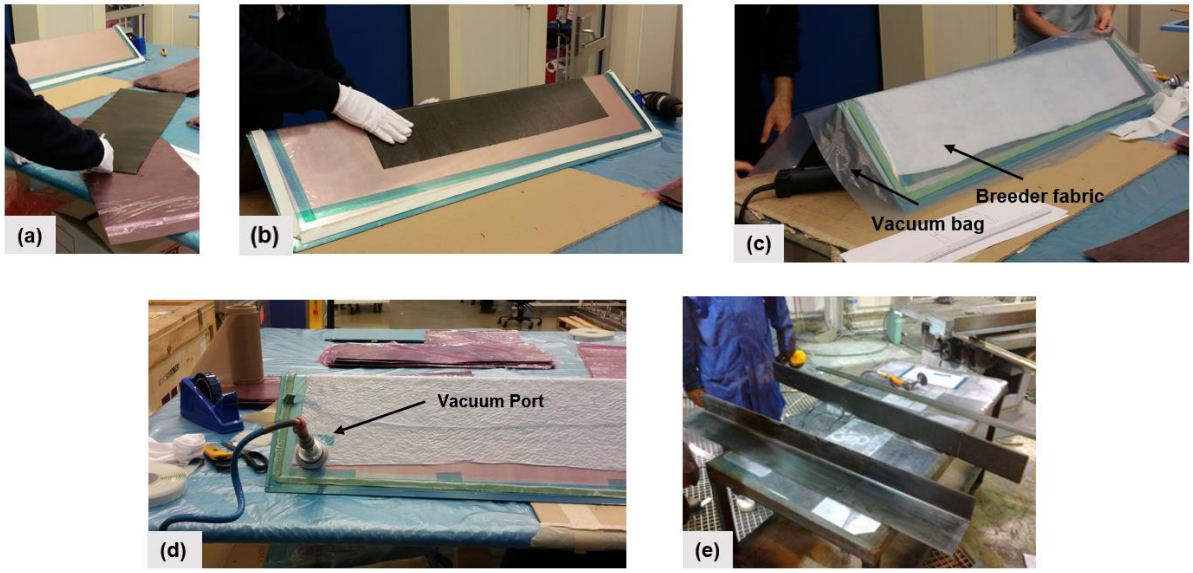

Figure 3.4 (a) Pre-pregs used for lay-up; (b) Hand lay-up over male tool; (c) Vacuum bagging preparation; (d) Vacuum bagging process; (c) Tool length specimens after manufacturing

3.3. Geometry and laminate properties

In this section the geometry and the laminate properties are presented in detail for three different lay-up orientations.

3.3.1. Geometric properties of the specimens

Manufactured L-shaped laminates were in tool size after curing. In this thesis, the experiments were conducted using coupon level specimens. The experimental setup and fixture were appropriate for coupon level testing. To obtain coupons from tool length size L-shape beams, 25 mm-width pieces were cut which refers flanges and brackets of the aircraft. The L-shape composite specimen has 90 mm symmetric upper arm lower arm. The geometry of the curved composite laminate in millimeters are presented in **Figure 3.5a**. The curved composite laminates were formed of 90 mm lower and upper arm, 5 mm inner radius, 25 mm width and 5 mm. 30 plies UD and cross-plied laminates have 5.54 mm thickness. The last version of the specimens after cut and the side view of three different lay-ups are presented in **Figure 3.5b**. In **Table 3.3**, the geometric properties of three different lay-ups are presented.

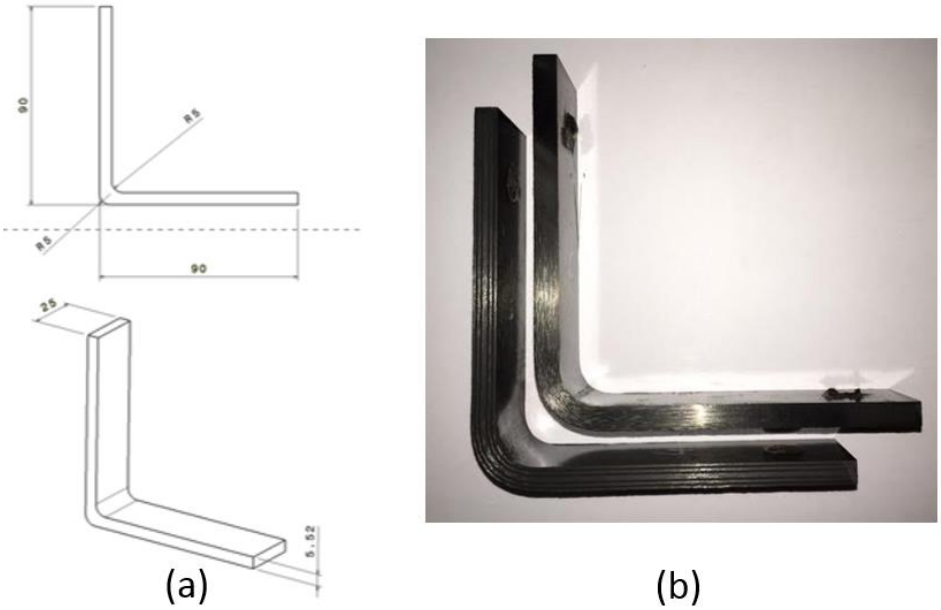

Figure 3.5 (a) The geometry of the specimen; (b) Specimens with different lay-ups

Table 3.3 Geometric properties of the specimens used in the experiments

Orientation	# of Plies	R_i (mm)	L_1 (mm)	L_2 (mm)	w (mm)	t (mm)
$[0]_{30}$	30	5	90	90	25	5.52
$[0_3/90_3/0_3/90_3/0_3]_s$	30	5	90	90	25	5.52

3.3.2. Laminate properties

Using PATRAN software, the geometry and the laminate properties were modeled for three different lay-ups using the lamina properties. **Figure 3.6** shows the modelled geometry and **Table 3.4** present the laminate properties of two different lay-ups.

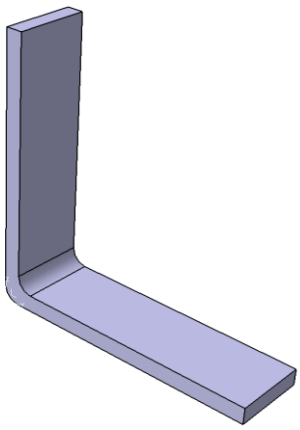

Figure 3.6 Model of the laminate

Table 3.4 Laminate properties of three different lay-ups

Orientation	E_{11} (GPa)	E_{22} (GPa)	v_{12}	G_{12} (GPa)
$[0]_{30}$	135	8.5	0.29	4.2
$[0_3/90_3/0_3/90_3/0_3]_s$	84.7	59.3	0.0417	4.2

3.4. Specimen preparation

In this section, specimen preparation for study and post-process is explained in detail, including nondestructive testing (NDT), polishing and preparation for fixing the specimen to the fixture.

3.4.1. Ultrasonic testing as NDT

Nondestructive testing is important in this study for detecting initial flaws occur during manufacturing process and investigating matrix cracking and delamination occur inside the specimen after exposed to cyclic loading. The hidden internal cracks may have a significant effect on structural integrity of the specimens and these cracks are not detectable by radiography or other NDT techniques but ultrasonic testing. In this study through-transmission method is used to scan the specimens. Through-transmission typically uses two transducers, one emitter and one receiver. The receiver is placed to the opposite side of the specimen and facing to the transmitter probe. The ultrasound is coupled to the specimen through a jet of water projected onto its surface which provides better conductivity of pulses as well. The pulse passes through the specimen and is bounced to the reflector such as glass plate before passing back through the specimen. **Figure 3.7a** illustrates the mechanism of the through-transmission ultrasound (TTU) scan. **Figure 3.7b** and **Figure 3.7c** presents the specimens held by the support structure anchored to the floor and the water jet during the scanning [44].

Figure 3.8 presents the ultrasonic testing results of 6 specimens of each lay-ups. TTU cannot detect the small size flaws but no critical size flaws were found in the curved region. These results are used as reference images in order to detect the matrix cracking and delaminations in the internal region of the composite laminates after fatigue loading.

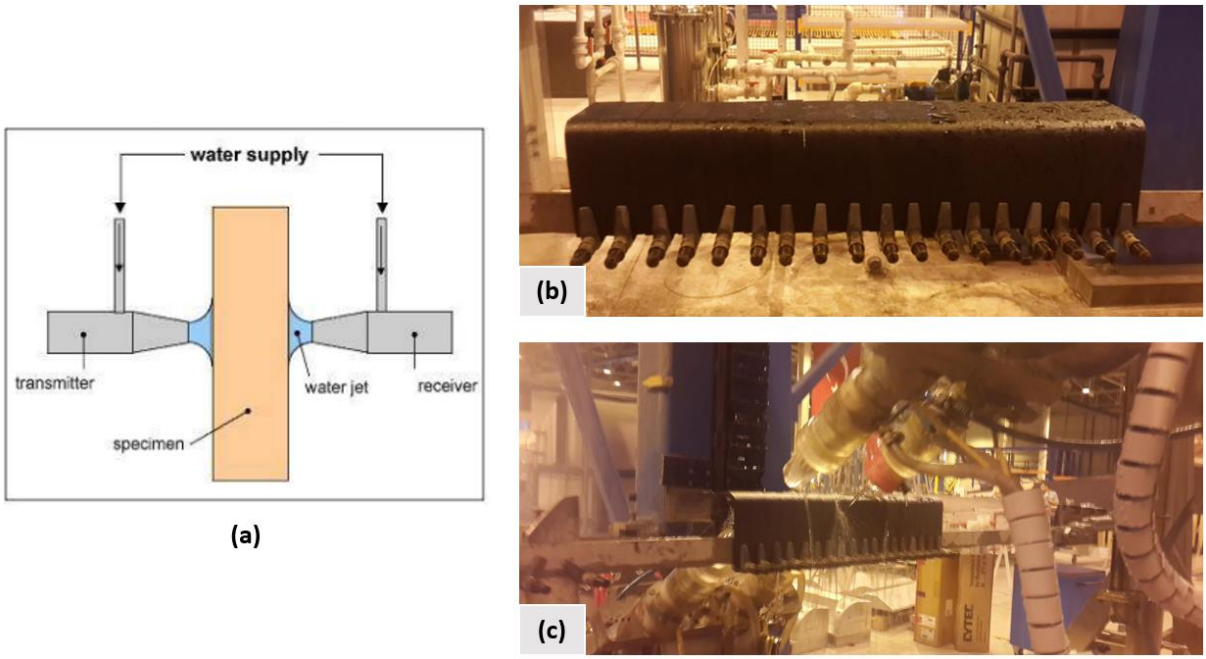

Figure 3.7 (a) Mechanism of through-transmission ultrasound scan [44]; (b) Specimens held by the support structure; (c) Scanned specimens and the water jet

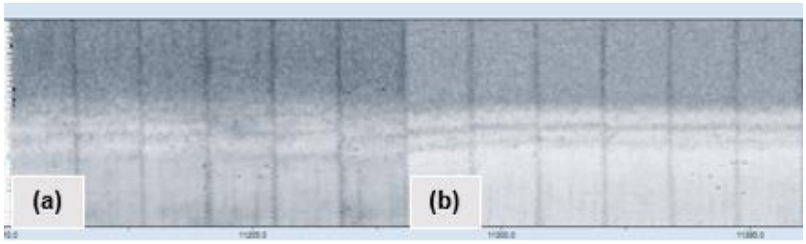

Figure 3.8 Ultrasonic test results of (a) [0] UD laminates; (b) Cross-plied laminates

3.4.2. Polishing process

In order to understand damage mechanisms of static and fatigue failure micro-structural investigation and observation during fatigue experiments were vital. Micrographs of specimens were taken using microscope after failure of specimens with the aim of observing the matrix cracking and delamination. After cutting procedure of the specimens to coupon level, there were machining marks through the lateral surface of the specimens. These marks create a rough surface and make the observation of damage mechanisms impossible under microscope. In order to get proper photos and make a complete analysis of fracture mechanism, it was requisite to have smooth and glassy surface. The lateral surface of the test specimens were polished to obtain the surface quality using different steps which are summarized in **Table 3.4**. Grinding procedure was conducted by waterproof circular SiC papers with different grain sizes (**Figure 3.9b**) using a rotating wheel (**Figure 3.9a**). The process was lubricated with water in order to prevent burnt of the surface and remove grinding particles. Then,

diamond grinding discs (**Figure 3.9b**) were applied with diamond particle solutions to obtain smooth and shiny surface. It was critical to clear lubricant from the specimens after polishing procedure. Water marks affect the micrographs, as well. Hence, it was required to use low-density fluid such as alcohol which dries quickly to clean the specimens.

Table 3.5 Different steps of polishing process

Steps	Grinding Paper	Grain Size	Lubricant	Time	Force (N)	Speed (rpm)
Rough Grinding	P240	60 μm	Water	150 s	50	240
	P400	35 μm	Water	150 s		
Fine Grinding	P1000	18 μm	Water	150 s		
	P2000	10 μm	Water	150 s		
Fine Finishing	Diamond Grinding Disc	3 μm	Diamond Particle Solution 3 μm	5 min		150
	Diamond Grinding Disc	1 μm	Diamond Particle Solution 1 μm	3 min		
Ultra-Fine Finishing	Polishing Clothe	25 nm	-	1 min		

(a) **(b)**

Figure 3.9 (a) Rotating wheel for polishing process; (b) SiC and diamond grinding discs

Micrographs of the specimens were taken before the experiments in order to compare the surface after damage. The specimens were analyzed with Leica DMi1 (**Figure 3.10a**) inverted microscope with 5x, 10x and 20x objectives and 10x camera magnification factor. The aim was to determine crack position in the layers. **Figure 3.10b** presents the micrographs of undamaged specimens with two different lay-ups with 20x magnification.

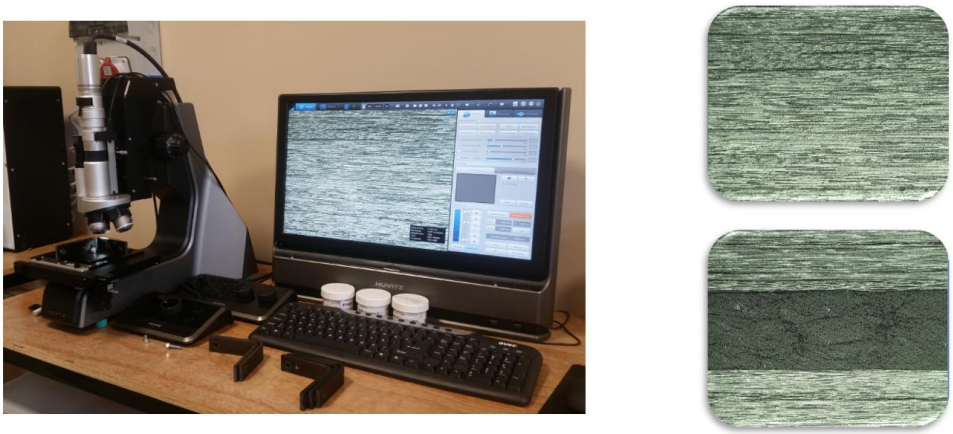

(a) **(b)**

Figure 3.10 (a) Leica DMi1 microscope; (b) Micrographs of the specimens

3.4.3. Preparation for fixing the specimen

Curved composite specimens were ready for fixing after investigating with ultrasonic test and also observing their lateral surface under microscope after polishing process. The test specimens were fixed to the axial loading fixture by bolts. In preliminary tests, 6 mm bolts were used to fix the specimens; however, these bolts experienced fracture under cyclic loading. Then, it was decided to engage the tips of the specimens to the pivot pin of the fixture with 8 mm bolts. With this aim, 8 mm hole was obtained using vertical drilling machine 7.5 mm from the curved region of the specimen. In static tests, the specimen was engaged to the fixture directly. Nevertheless, for fatigue testing, in order to prevent specimen from crack growth starting near the hole, induced by stress concentration due to bolt, metal sheet was glued to the tips of the bottom surface of the specimens. A sand paper was glued to the leave of the hinge in order to prevent slipping. The leave of the hinge was glued to the tip of the specimen and engaged to the fixture together as shown in **Figure 3.11**.

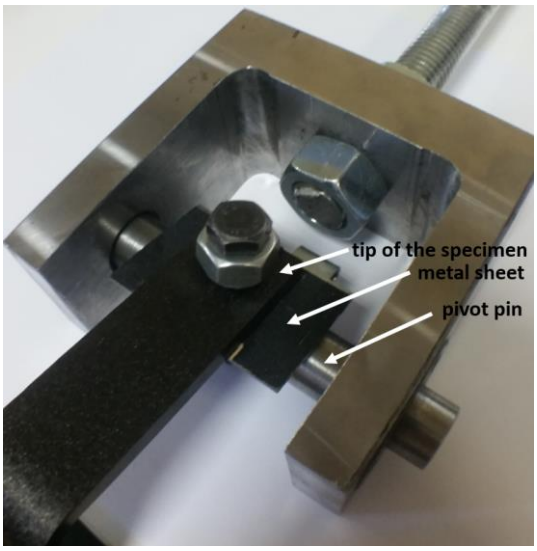

Figure 3.11 Tip of the fatigue tests specimen with metal sheet

3.5. Fixture design and experimental method

3.5.1. Fixture design and loading condition

The aim of this thesis study is investigate the fatigue behavior and static failure of curved beam laminates under pure bending moment. There is an American Society for Testing and Materials (ASTM) standard for measuring curved beam strength (CBS). ASTM D6415 uses curved composite laminates subjected to four point-bending to obtain pure bending moment [43]. However, applying axial force from both tips of the specimen creates bending moment in the curved region of the specimen, as well. Before ASTM D6415/D6415M standards and four point-bending test, applying pure bending moment was a challenge and in literature there are numerous examples of similar axial loading fixtures [31, 33].

At first, hinge mechanism was used in order to apply axial loading to the curved specimens. Two hinges were fastened to the two arms and the load was applied to the specimen through the hinges. Sandpaper was glued to the hinge to fasten the hinge to the specimen without slipping. Hinges were glued to the specimen as well and screwed together so that load was distributed as shown in **Figure 3.12a**. The other leaves of the hinges were held by grips of the test machine. However, after 1000 N the joint of the hinges started to be unfolded. Whereas, **Figure 3.12b** shows the original hinges, **Figure 3.12c** presents the deformed hinges. Then, it was confirmed to design and manufacture a special loading fixture appropriate for axial loading.

In this study, curved composite laminates were subjected to axial static and fatigue loading from both tips using special design fixture. The loading conditions and experimental fixture with the specimen are shown in **Figure 3.13a**. Both arms of the specimen were bolted to a pivot pin bearing system in order to fix the arms on the fixture and provide free rotation around z-axis (**Figure 3.13b**). Axial force was applied to the fixture through the screw located in the middle of the fixture (**Figure 3.13a**).

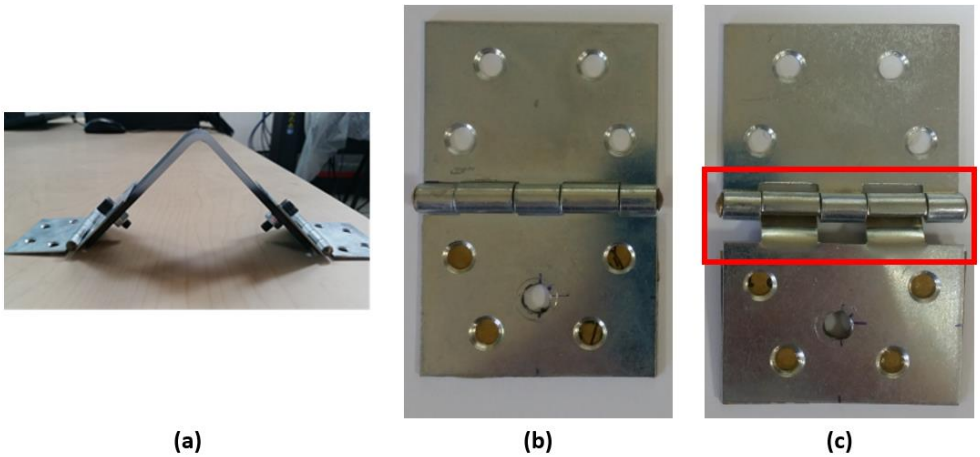

Figure 3.12 (a) Hinge mechanism on the specimen; (b) Original hinge; (c) Deformed hinge under axial loading

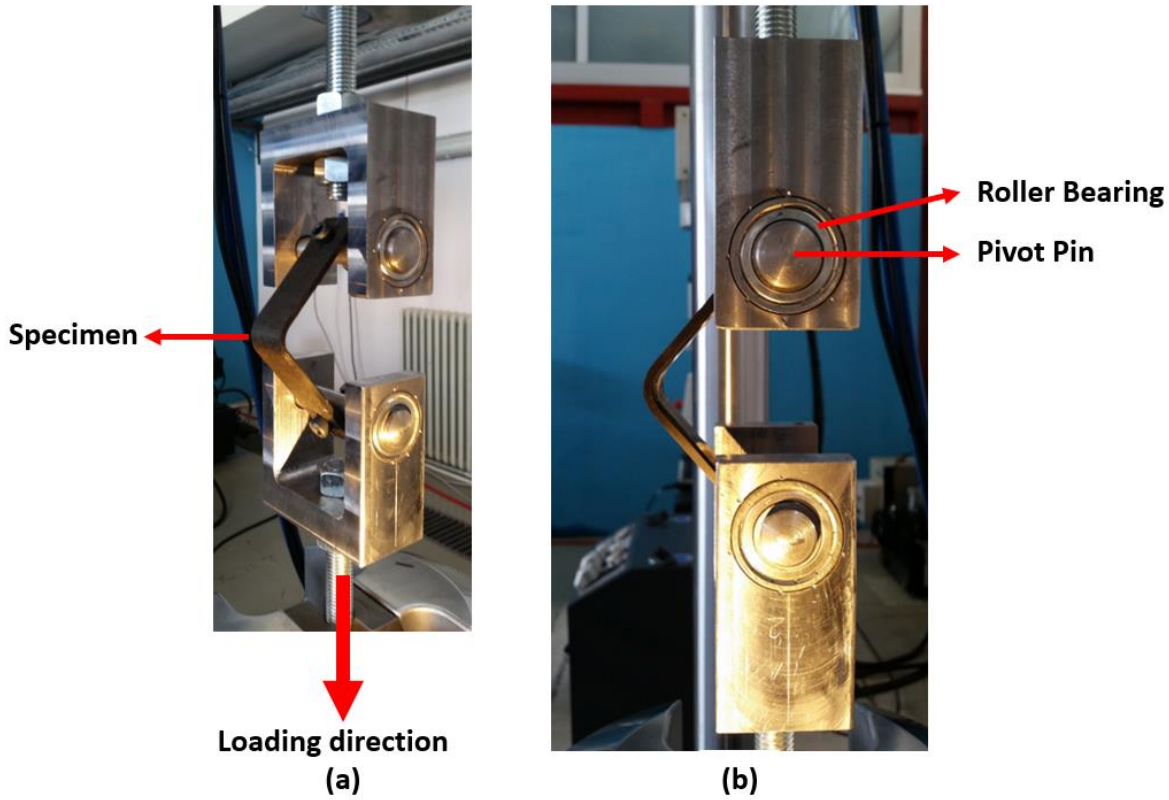

Figure 3.13 (a) Specimen and the loading fixture; (b) Closer look to the fixture and the specimen

3.5.2. Experimental setup

MTS 250 kN axial loading servo-hydraulic test machine was used to carry out static and fatigue tests. All static tests were conducted under displacement control at a rate of 2 mm/min. Multi-Purpose Testware (MPT) module was used to give the displacement command to the test machine and acquire the data. Delaminations were recorded using Photron FASTCAM SA-5 high-speed camera system which recorded the images with framing rates of 150000 fps at full resolution of 1 MP. **Figure 3.14** presents the experimental setup, including the loading fixture, specimen and the high speed camera system.

Fatigue tests were conducted under displacement control as well with the R ratio, $R=\delta_{min}/\delta_{max}$, of 0.1 and at 2 Hz frequency. Basic Testware (BTW) module was used to give the command of the parameters used in fatigue experiments and for data acquisition as well. Full process was recorded with DSLR Canon D650 camera with macro-lens and crack initiation and propagation was observed.

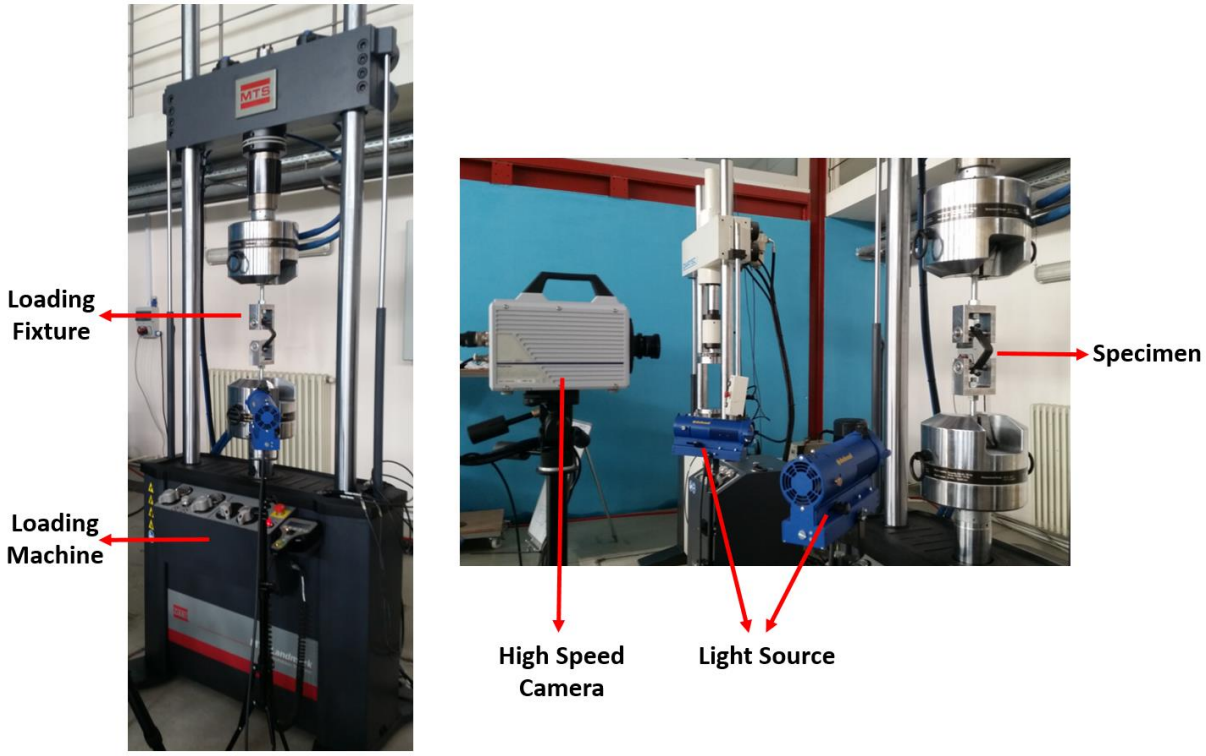

Figure 3.14 Experimental setup

3.6. Preliminary tests

Preliminary tests were conducted in order to validate the loading fixture and experimental method. In the preliminary tests, [0] UD 25 ply specimens with R_i equal to 10 mm were exposed to static and fatigue tests. Static test was conducted under displacement control at the rate of 2 mm/min. Fatigue test was conducted under displacement control at R-ratio of 0.5 with maximum displacement of 12 mm and at 2 Hz. In the **Figure 3.15**, the load displacement curves of the static and fatigue tests are presented. Static test is represented with dark red line and the evolution of the fatigue curve is represented with red dashed lines. As seen from the plot, force increased with increasing displacement almost linearly. Maximum load was 1597 N at 11 mm displacement. Then load dropped suddenly to 215 N with the multiple delaminations occurred through the thickness at the curved region. After that point the specimen failed almost completely with critical stiffness degradation. As can be seen in **Figure 3.15**, under fatigue loading stiffness degradation was observed with ongoing cycles. The slope of the load displacement curves was calculated in every 5000 cycles and corresponding compliance value of the material was plotted in **Figure 3.16**. During the tests, the loading fixture experienced no deformation as hinges mechanism. Both static and fatigue tests results were rational and consisted with the expectations. With these preliminary tests, it was proved that the loading fixture had satisfying design and it was ready for further experiments.

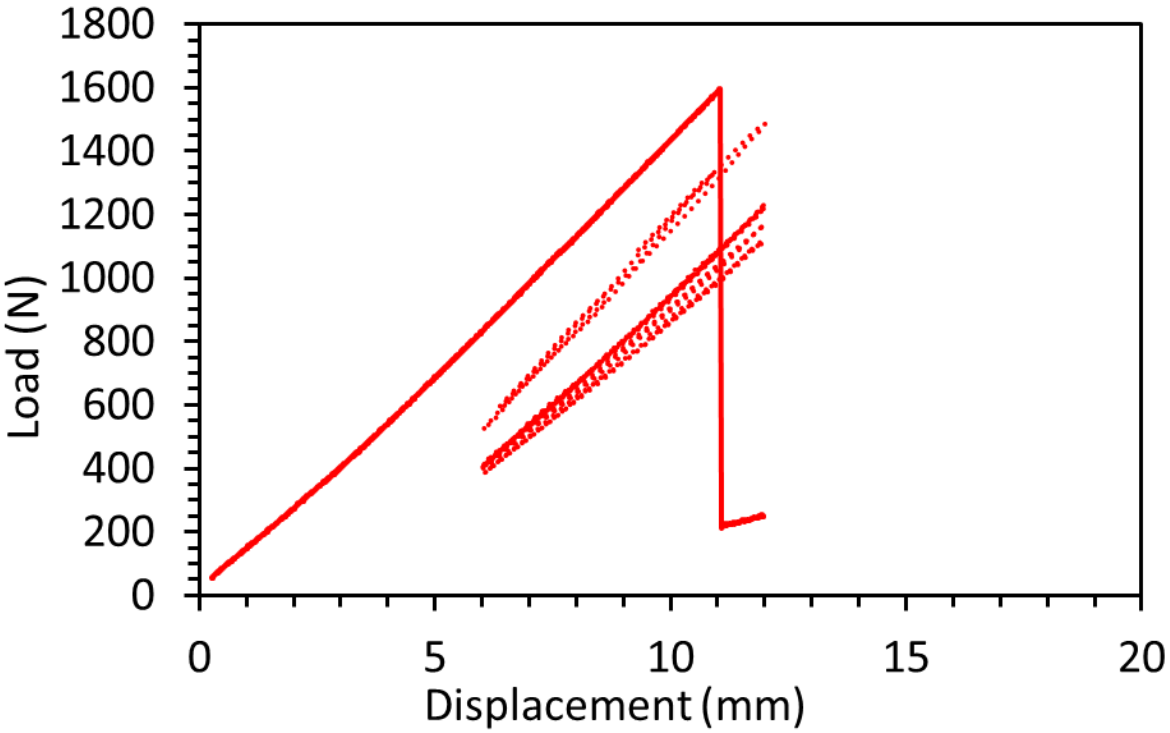

Figure 3.15 Load displacement plot of preliminary static and fatigue tests

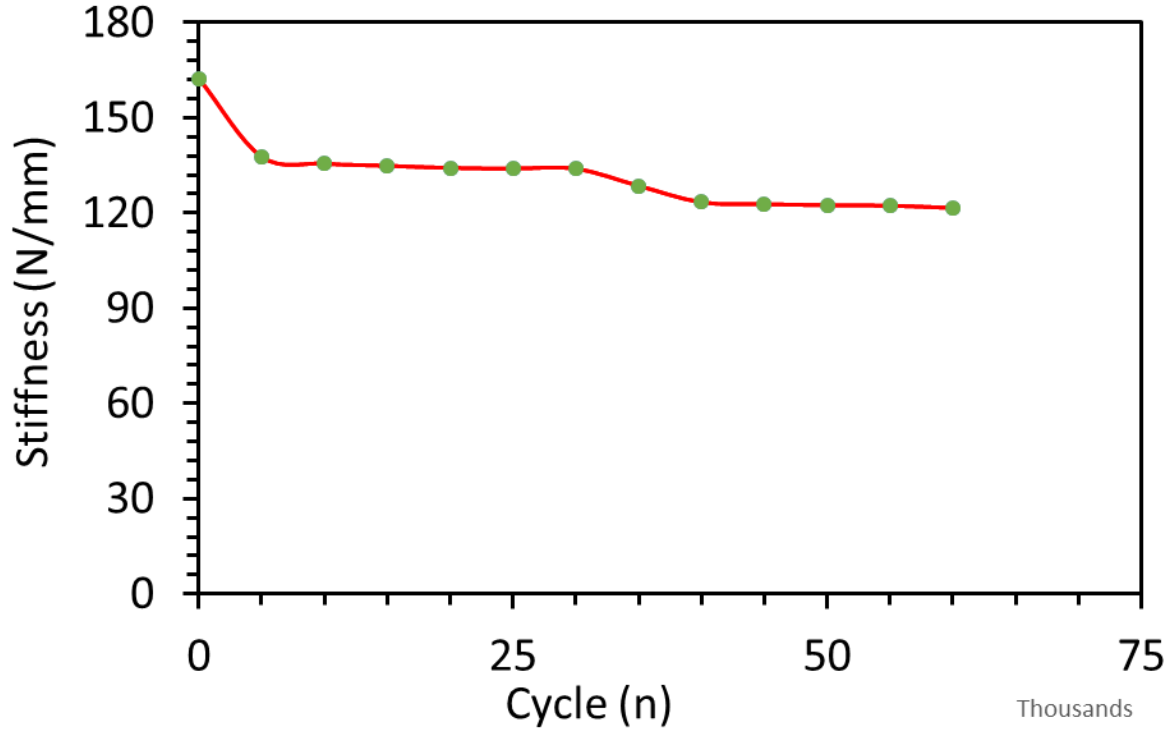

Figure 3.16 Stiffness degradation of $[0]_{25}$ in preliminary fatigue test

Chapter 4

STATIC TEST RESULTS

In this chapter, the results of static experiments that are conducted with curved composite laminates are discussed. All tests are planned and conducted at RÜZGEM, METU Wind Center. Static loading experiments are carried out using two different lay-up orientations namely, $[0]_{15s}$ UD and $[0_3/90_3/0_3/90_3/0_3]_s$ cross-plied curved composite laminates under bending moment. Four different static tests are conducted on each specimen configuration in order to determine ultimate strength and understand the failure mechanism of each material to use in fatigue experiments. Failure mechanisms are investigated using micrographs and high speed camera images. Static test results of two different lay-ups are presented. The results and the damage mechanisms are compared for both lay-up orientations. In the all plots, the results of [0] UD laminates are designated with red lines and cross-plied laminates with black lines.

4.1. [0] UD laminates

The first results belong to [0] UD curved composite laminates. The lay-up details are explained in the experimental method and material part. **Figure 4.1** presents the load displacement curve of 4 different static tests conducted on [0] UD curved composite laminates. The initial slope of the four specimens are the same which corresponds to the initial stiffness of the material. After reaching to the maximum interlaminar stress, sudden load drop is observed corresponding to delamination. After the first failure, the maximum load capacity of [0] UD curved composite laminates drops to around 40% of the maximum load. All specimens carry load with very low slope with steps in the load displacement plot which corresponded to little load drops due to crack formation leading to the second delamination with multiple cracks through the thickness at the curved region corresponding to complete stiffness loss of the specimens.

Load-displacement curves (**Figure 4.1**) of the four specimen have similar behavior. However, although all specimens have the same initial slope the ultimate strengths of the four specimen are different. The first specimen has higher ultimate strength than the other three specimens. The other three specimens experience the first load drop almost at the same load value. Despite the different maximum load values of the specimens, the first load drop level of all specimens are almost the same, 400 N. Even the damage occurs at different load values the failure pattern of the specimens are almost the same under static loading for [0] UD curved composite laminates. The average ultimate strength of [0] UD specimens are 1100 N at 8 mm displacement in order to use in fatigue loading experiments.

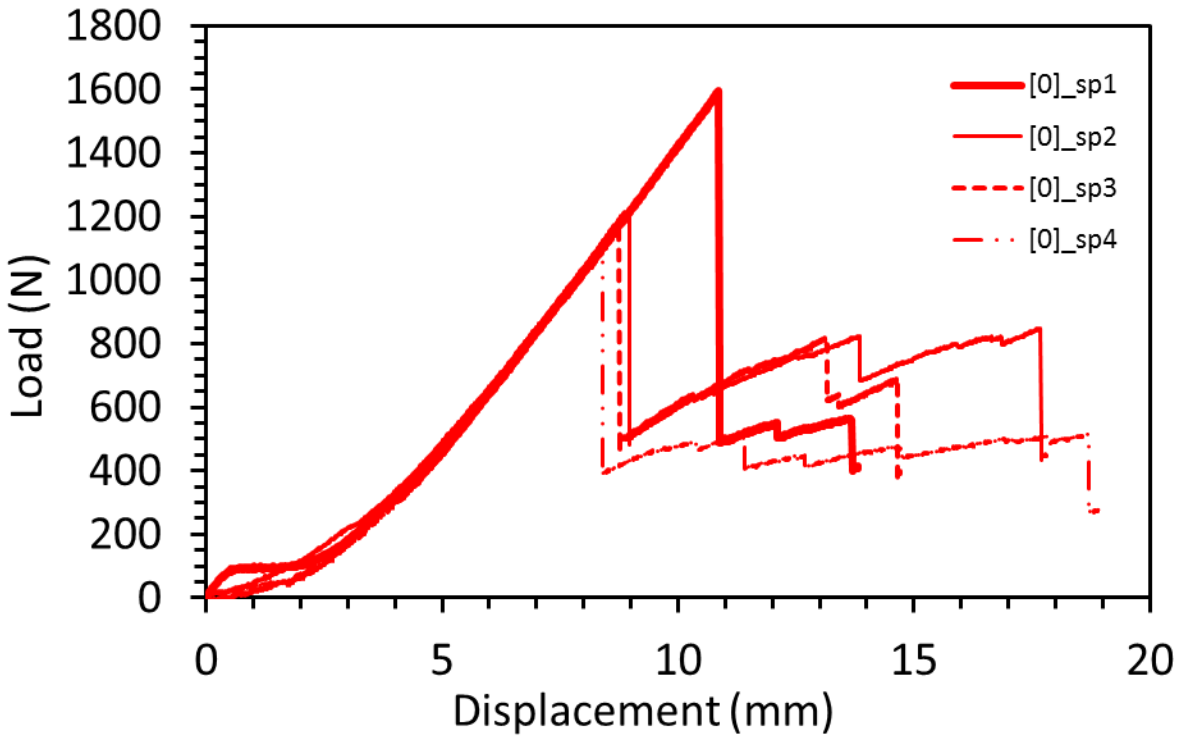

Figure 4.1 Load-displacement plot of [0] UD specimens under static loading

In the preliminary tests, specimens with 25 ply carry 1650 N average maximum load. Since these [0] UD laminates are thicker, it is expected to carry more load. However, as can be seen from the plot, the average maximum load is 1200 N. Besides the thickness, the inner radii are different for two specimen configurations. [0] UD laminates in this study is 5 mm, smaller than the inner radius of preliminary test specimens. According to Kedward et al. [46], the radial stress, σ_r increases with decreasing mean radius, R_m as shown in **Equation 4.1,** so that in this study [0] UD laminates experience higher stress state with lower load level.

$$\sigma_{r,max} = \frac{3M}{2btR_m} \qquad (4.1)$$

Crack initiation and propagation occur sudden and catastrophic. DSLR camera cannot catch the initiation and the progression of the damage. In order to understand the failure mechanism in detail high speed camera images are taken with 210000 fps. The high speed camera images present the damage evolution of [0]_sp1. The load-displacement curve of the specimen is investigated separately in **Figure 4.3**. The load drops are marked on the load-displacement curve which correspond to the delaminations observed in high speed camera images. **Figure 4.4** presents the high speed camera images and the damage progression of [0]_sp1. **Figure 4.4a** presents the delamination occurring in the first load drop. The first delamination starts suddenly from the middle of the curvature at 0.35t near the highest radial stress location. Then the delamination proceeds to the arms instantaneously. The little load drop is observed in the load-displacement plot, however no delamination is observed from the lateral

surface. **Figure 4.4b** presents the delaminations corresponding to the second load drop. Multiple cracks are formed near the initial delamination with increasing load and the second delamination occurs and grow through the arms instantaneously corresponding to the second load drop. The second delamination occurs at the 0.65t of the specimen which corresponds to 0.4 of the remaining beam thickness. At that location the maximum stress in the remaining ligament occurs.

In previous studies and preliminary tests, maximum radial stress and delamination occurs at 0.4t. FEA shows that decrease in inner radius changes the location of maximum radial stress location [47]. **Figure 4.2** present the maximum radial stress variation with decreasing inner radius. The maximum radial stress occurs at 0.4t for R_i,equals to 10 mm whereas if inner radius is 5 mm as in this study, the maximum radial stress location shifts to 0.35t.

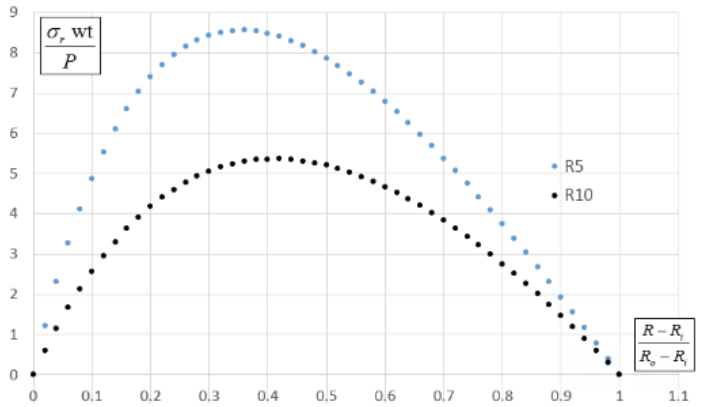

Figure 4.2 Radial stress distribution through thickness [47]

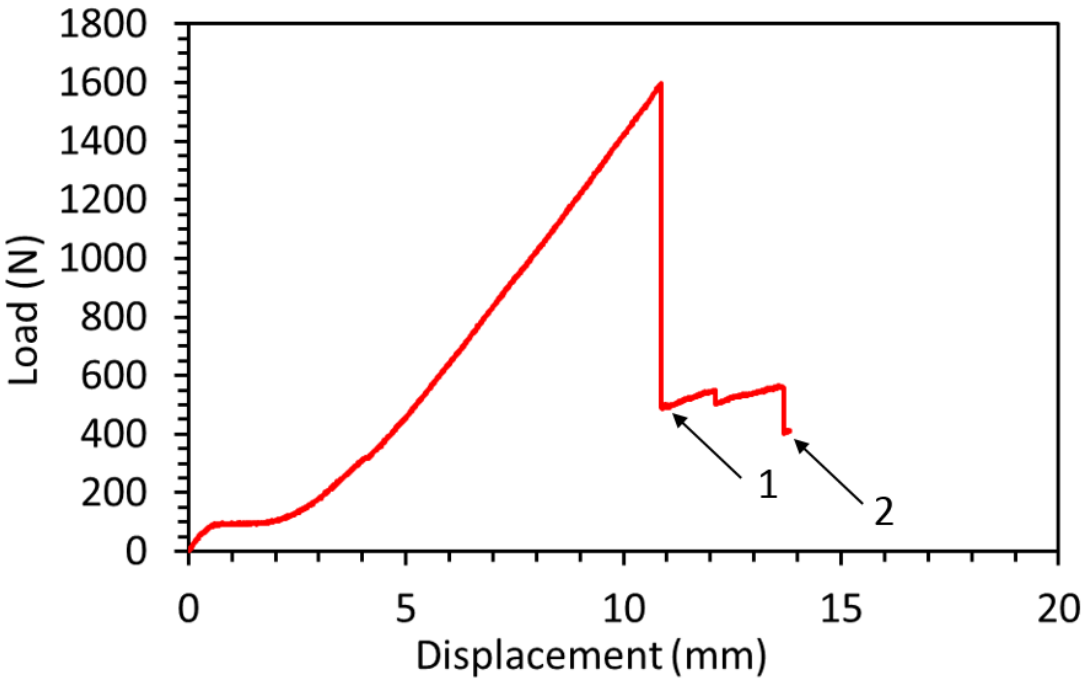

Figure 4.3 Load-displacement plot of [0]_sp1 under static loading

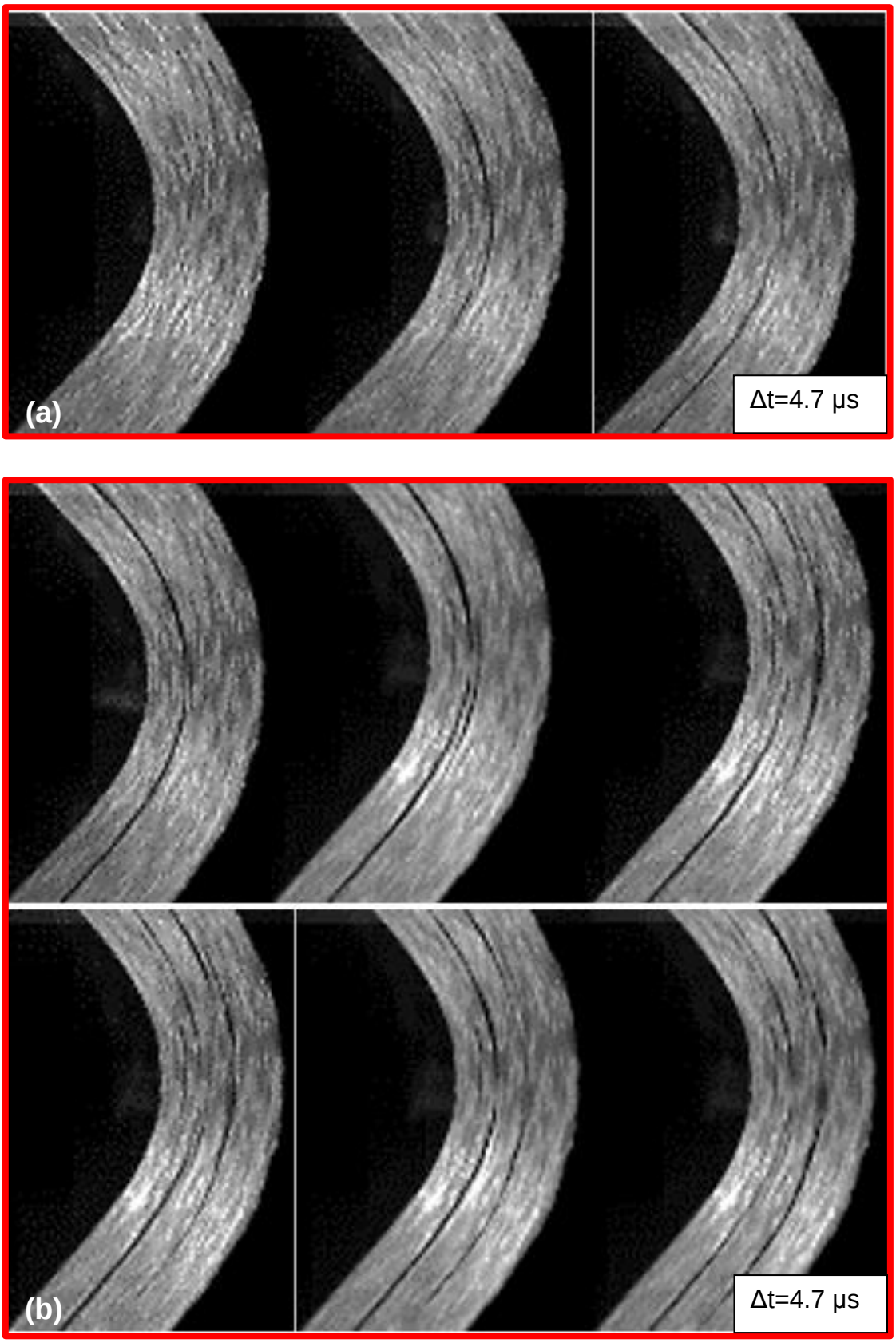

Figure 4.4 High speed camera images of [0]_sp1 (a) The first load drop; (b) The second load drop

The damage evolution is investigated using DSLR camera as well. The results of [0]_sp2 is examined. The load-displacement curve of [0]_sp2 is presented in **Figure 4.5** individually. The initial state and the load drops are marked and corresponding damage evolution is shown in **Figure 4.6**. **Figure 4.6a** represents the initial form of the specimen without any crack. **Figure 4.6b** shows the first delamination occurred which corresponds to the first load drop. The delamination initiated at 0.35t where the radial stress is maximum. In the load-displacement curve little load drop are observed after first load drops which means crack propagation to the arm of the curved laminates as shown in **Figure 4.6c**. The final failure is presented in **Figure 4.6d** corresponding to final load drop. As shown in the figure the final failure occurs with the multiple crack through the thickness which means the complete stiffness loss of the specimen. The second major delamination occurs at 0.75t of the specimen corresponding to the 0.4t of the remaining thickness where the radial stress is maximum for the remaining ligament. **Figure 4.6e** presents the micrograph of the curved region of the same specimen. Since there is no load on the specimen in the micrograph, the delaminations are more unapparent than the DSLR camera images. However, the path of the delaminations can be seen easily on the lateral view of the specimen.

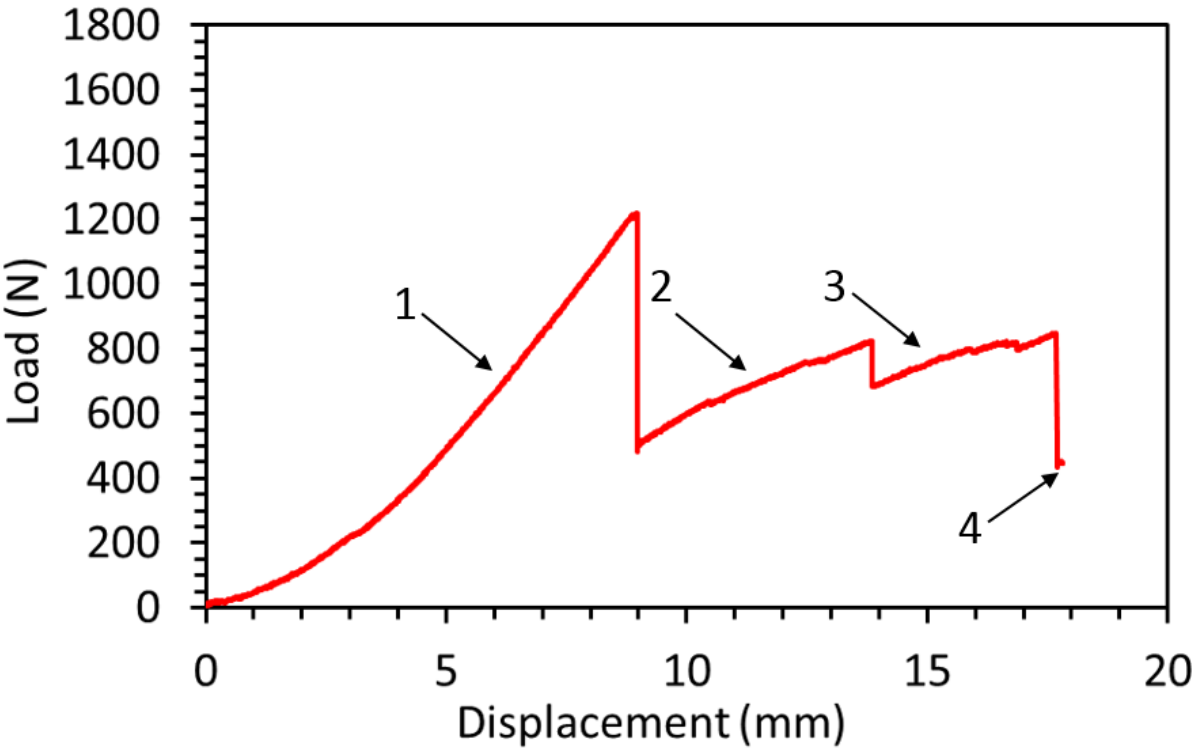

Figure 4.5 Load-displacement plot of [0]_sp2 under static loading

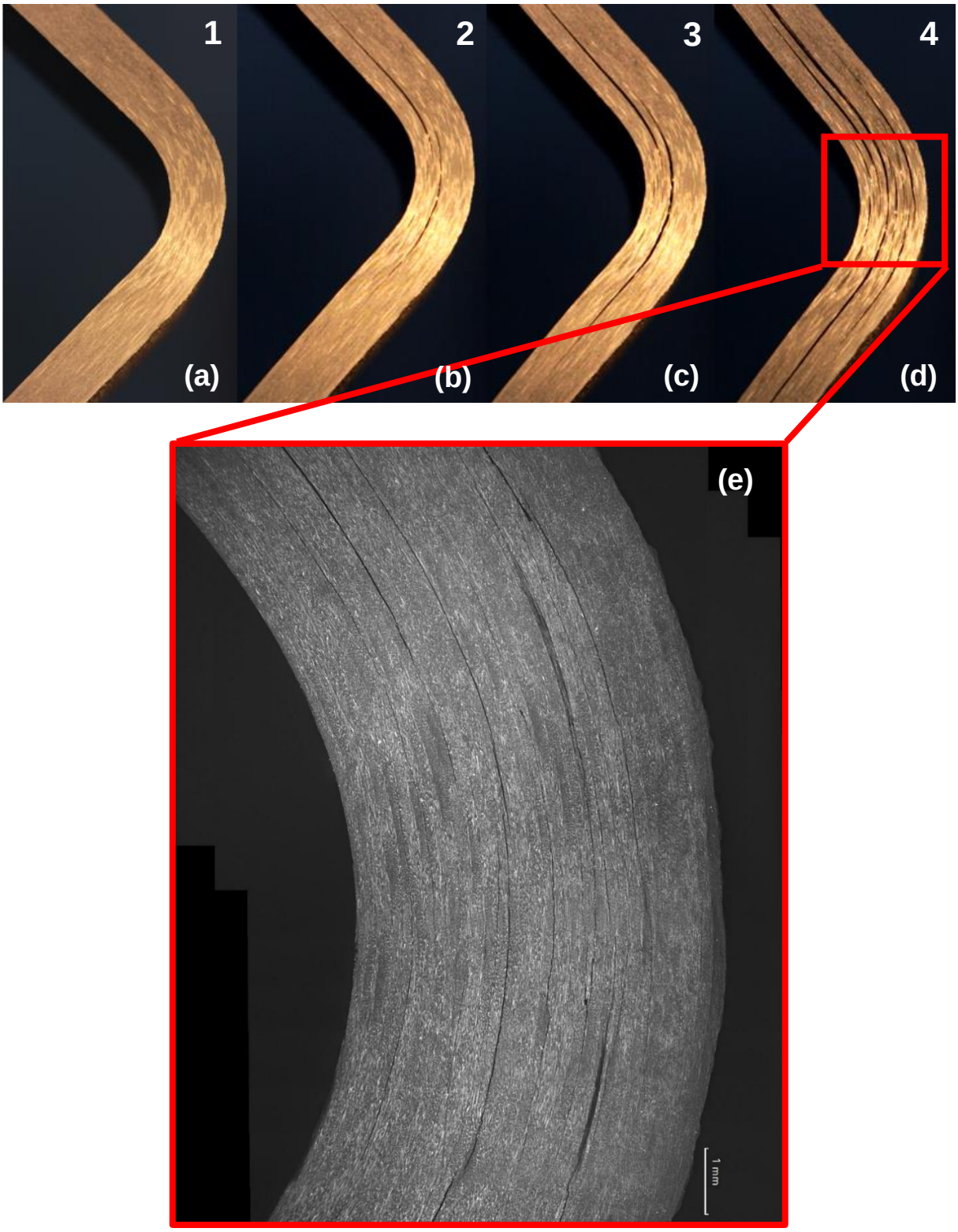

Figure 4.6 The images of [0]_sp2 under static loading (a) Initial state; (b) After first load drop; (c) The crack propagation; (d) After failure; (e) The micrograph of the side view after failure

4.2. Cross-plied laminates

In this section the results of cross-plied laminates are presented. The lay-up orientation is $[0_3/90_3/0_3/90_3/0_3]_s$ and the lay-up details are explained in the experimental method and material part. **Figure 4.7** presents the load displacement curve of 4 different static tests conducted on cross-plied curved composite laminates. The initial slope of the four specimens are the same which corresponds to the initial stiffness of the material. Cross-plied laminates experience multiple load drops until failure. The first load drop corresponds to the first delamination occurred in the interior off-axis plies where the tensile stress is maximum. The ultimate strength of all specimen varies and the load drops to different load levels after the delamination. The first delamination occurs in the first off-axis ply of the first and the second specimen. Nevertheless, in the third and fourth specimens, delamination initiates from the second off-axis ply. The differences in load drop levels are the consequence of these differences in delamination initiation location. After the first delamination the remaining plies continue carrying load. The slope of the load displacement curve is almost the same with the initial slope of the material. The load reaches almost the maximum value then the second load drop occurs corresponding to the second delamination adjacent off-axis ply. Second load drop corresponds to the final failure for all specimens except the first specimen. The first specimen carries load after the second load with lower slope and then experience the third delamination in the off-axis plies corresponding to the final failure. The differences in the load-displacement curves of the specimens from the same batch may occur due to the manufacturing defects.

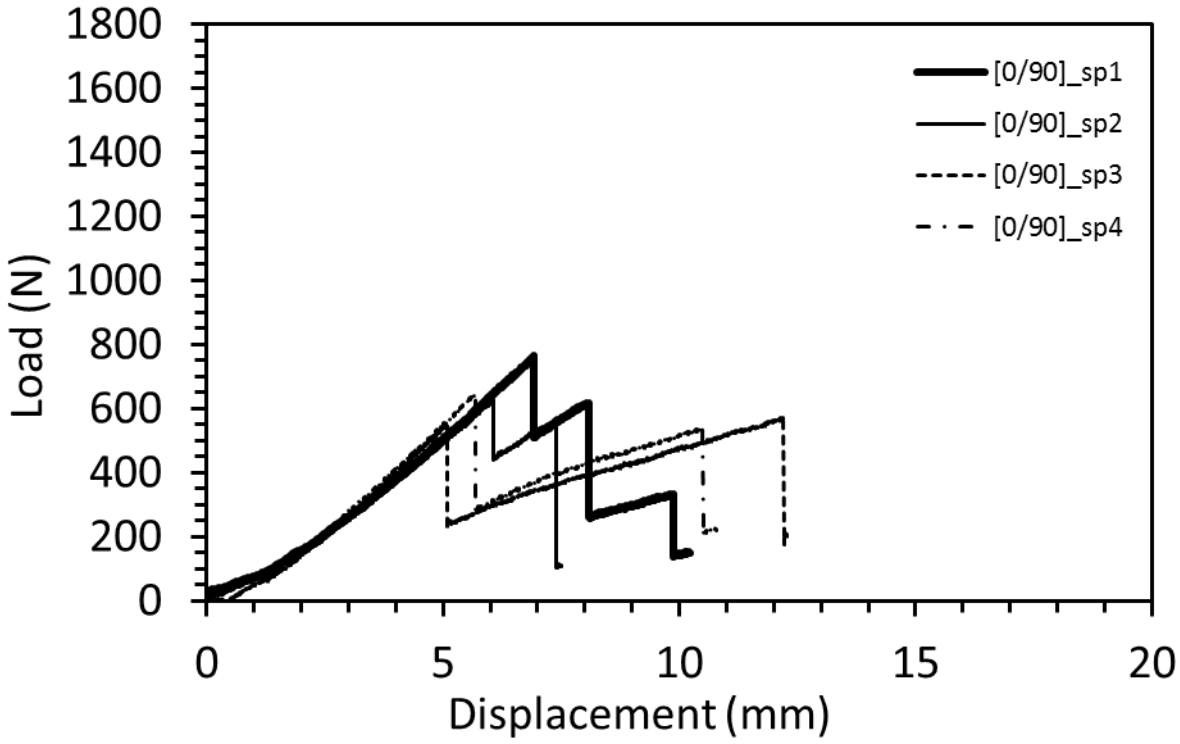

Figure 4.7 Load-displacement plot of cross-plied laminates specimens under static loading

The average ultimate strength of cross-plied laminates 650 N at 5.5 mm displacement in order to use in fatigue loading experiments.

The failure is catastrophic and sudden so that it is impossible to catch the initiation and the progression of the damage. In order to understand the failure mechanism, high speed camera images are taken for [0/90]_sp2. The load-displacement plot of [0/90]_sp2 is presented in **Figure 4.8**. The load drops are marked which correspond to the delaminations observed in the high speed camera images. High speed camera images of [0/90]_sp2 are shown in Error! Reference source not found.. **Figure 4.9a** shows the evolution of the first damage which corresponds to the first load drop. The first damage occurs suddenly in the interior off-axis ply as matrix cracks starting from the mid curvature then the matrix crack jumps to the adjacent 0º ply and lead the delamination propagation through the arm. **Figure 4.9b** presents the sequence of the damage evolution which occurs in the second load drop. The second and third delaminations occur instantaneously corresponding to the second load drop. However, high speed camera images show that matrix cracks start first in the second 90º plies and lead to the delamination proceeding through the adjacent 0º plies then the failure occurs in the next 90º plies. In the third off-axis plies matrix cracks initiates near the curved region leading to delamination in the interface.

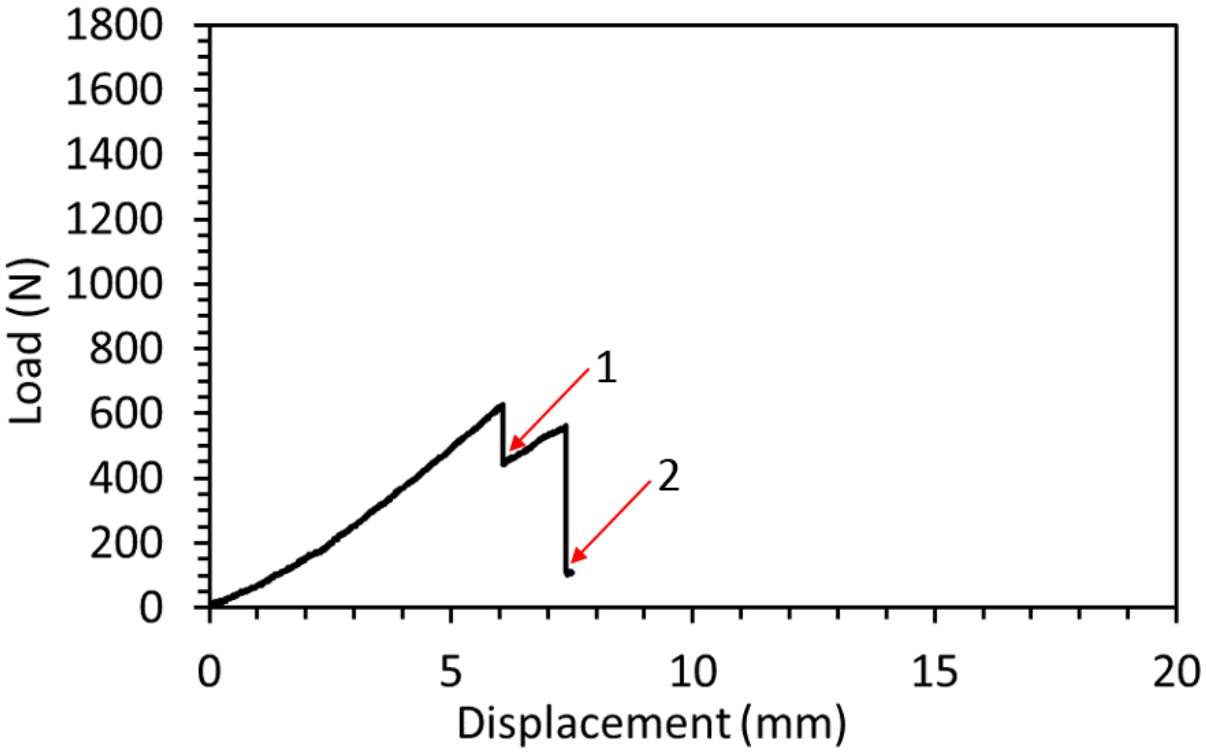

Figure 4.8 Load-displacement plot of [0/90]_sp2 under static loading

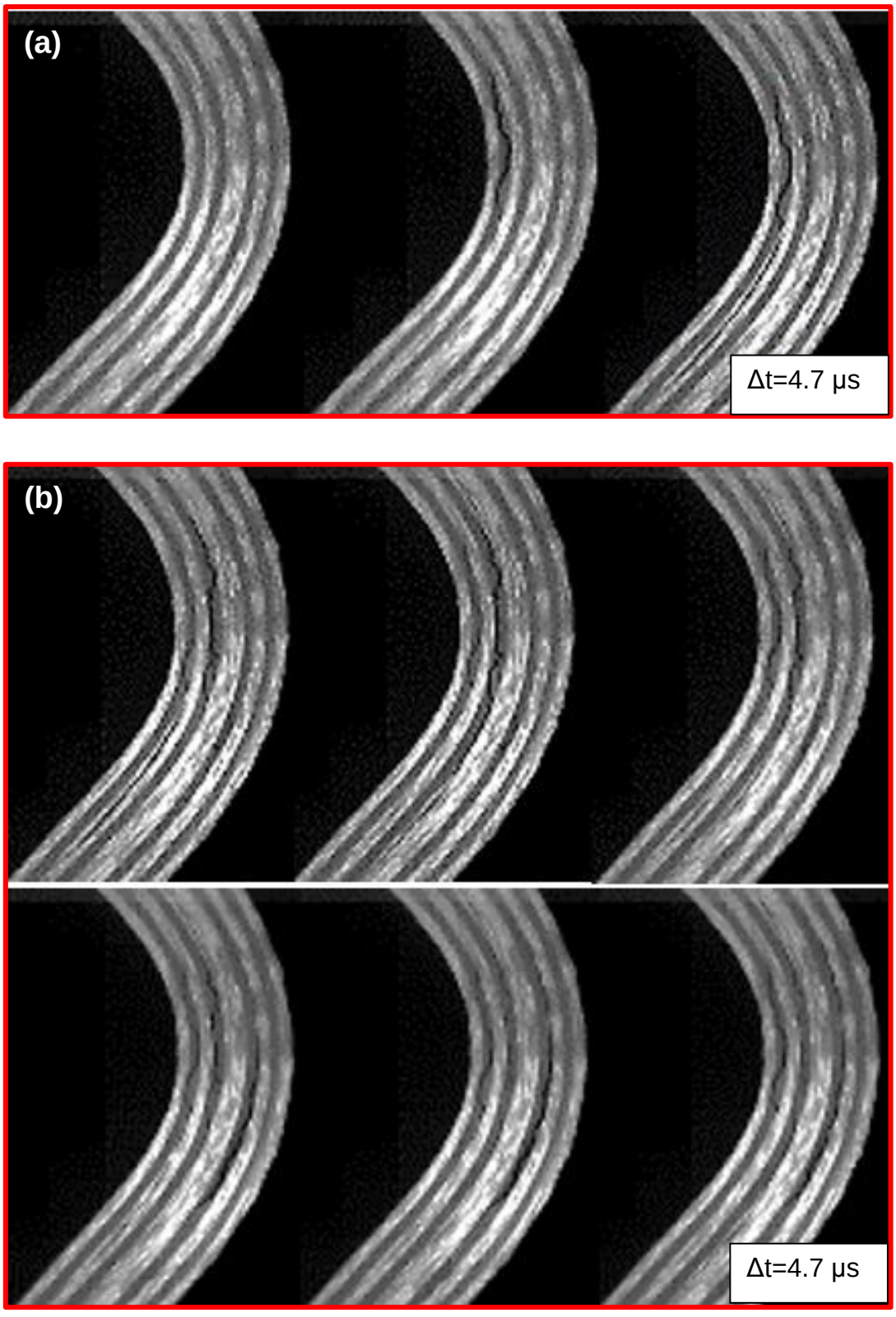

Figure 4.9 High speed camera images of [0/90]_sp2 (a) The first load drop; (b) The second load drop

In order to investigate the damage mechanism, DSLR camera images are examined as well. The damage evolution on [0/90]_sp4 is presented using normal camera images. **Figure 4.10** shows the load-displacement plot of [0/90]_sp4. The initial state of the specimen and load drops which correspond to the delaminations observed in the normal camera images are marked on the load-displacement curve. **Figure 4.11** presents the damage evolution on the specimen [0/90]_sp4. **Figure 4.11a** shows the initial situation of the specimen without any crack. In **Figure 4.11b**, the crack initiates at the curved region and propagates through the arms. In the middle region the matrix cracks are observed which jump to the adjacent 0º plies and propagate as delamination (**Figure 4.11c**). **Figure 4.11d** presents the second delamination occurred in the next off-axis ply corresponding to the final failure of the specimen. Matrix cracks occurred in the mid of the curvature lead to delamination in the interface of the 0º and 90º plies. The delamination propagates through the arm of the specimen. **Figure 4.11e** presents the micrograph of the curved region of the same specimen. Little defects can be seen easily in the interior and the second off-axis ply. The matrix cracks initiated from the off-axis plies can be observed easily. In the second 90˚ ply, it can be easily seen that the matrix crack not only proceeds through the interface, but also jump to the adjacent 0˚ ply and progress as delamination throughout the fibers. In the third off-axis ply, the matrix crack proceed through the interface as well. The damage initiates at different 90º ply on [0/90]_sp2 and [0/90]_sp4. This difference cause the difference in the load level after first load drop. These images shows that despite the differences in the load-displacement curves of the specimens, the failure pattern is similar in cross-plied laminates. The results and failure pattern is consistent with the study conducted by Uyar et al. [45]

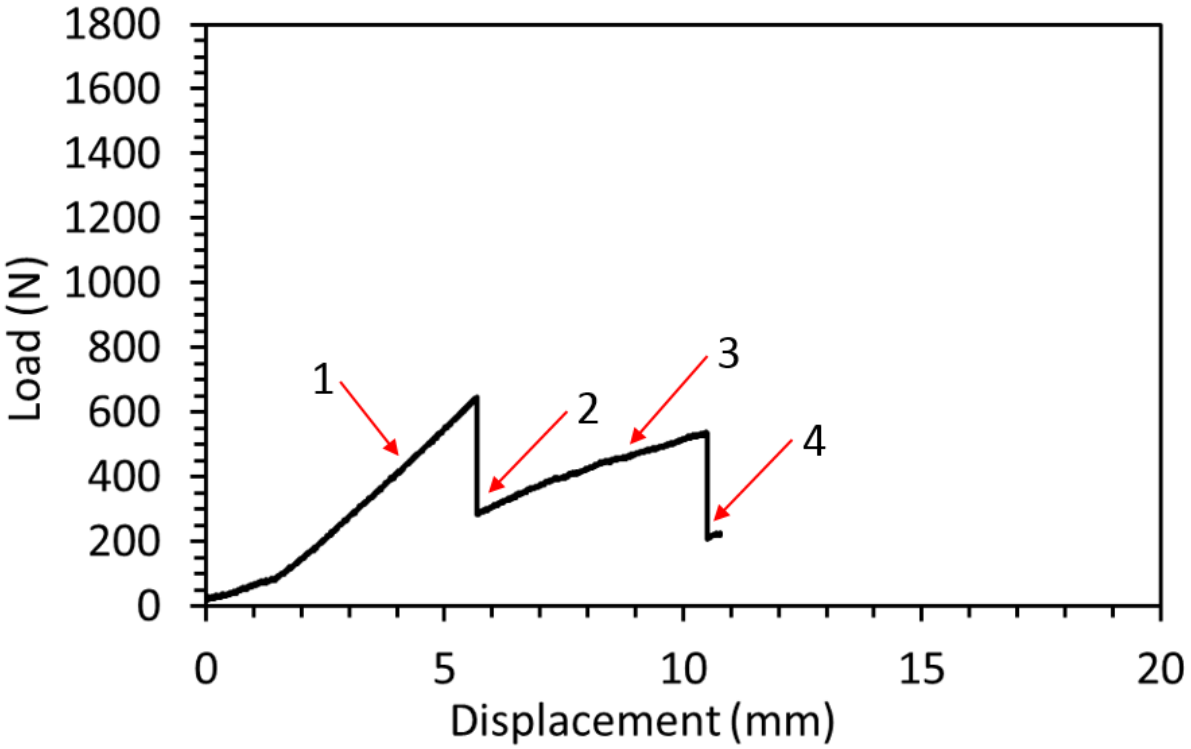

Figure 4.10 Load-displacement plot of [0/90]_sp4 under static loading

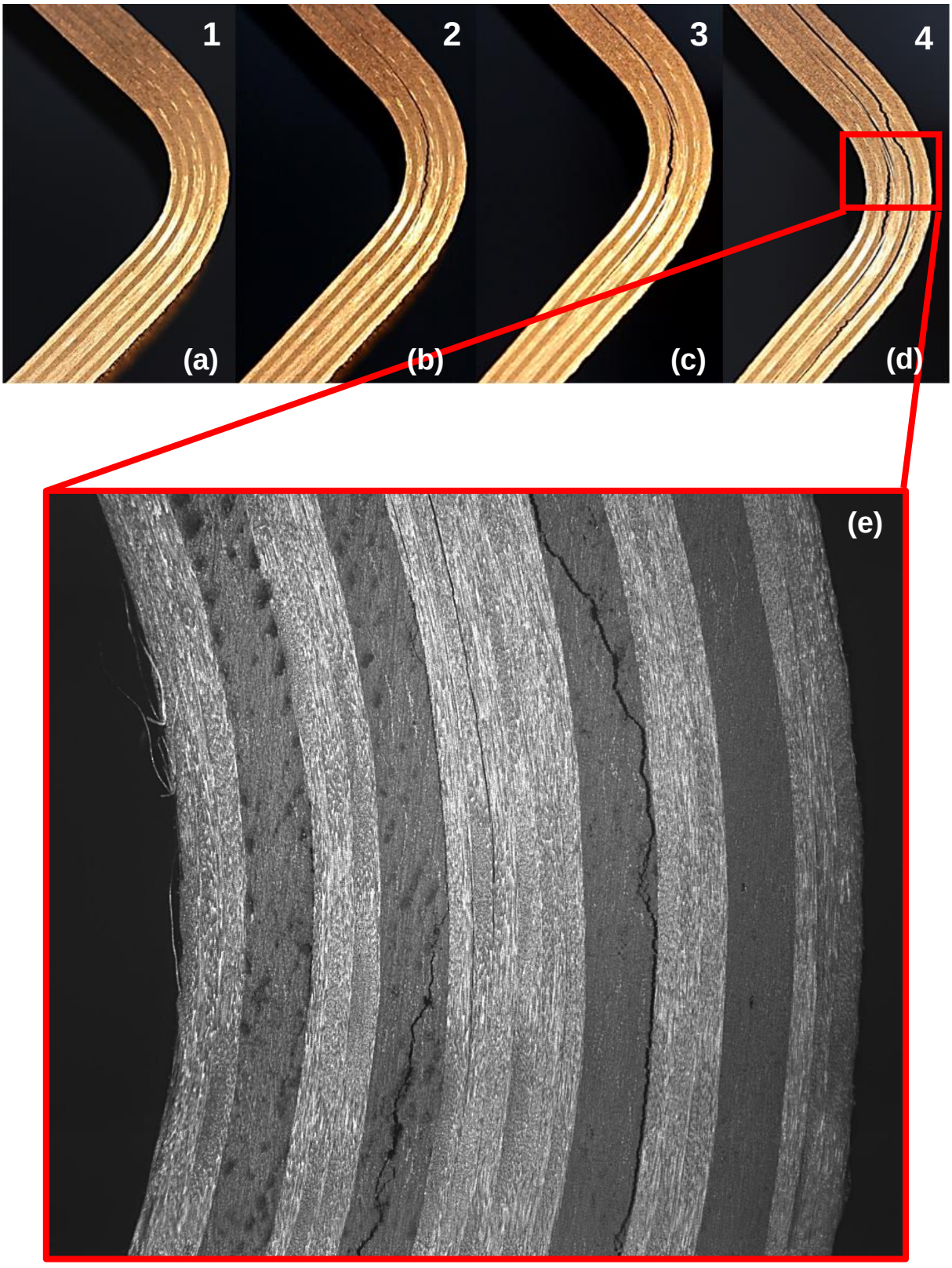

Figure 4.11 The images of [0/90]_sp4 under static loading (a) Initial state; (b) After first load drop; (c) The crack propagation; (d) After failure; (e) The micrograph of the side view after failure

Chapter 5

FATIGUE TEST RESULTS

In this chapter, the results of fatigue experiments that are conducted with curved composite laminates are discussed. All tests are planned and conducted at RÜZGEM, METU Wind Center. Fatigue loading experiments are carried out using three different lay-up orientations namely, $[0]_{15s}$ UD and $[0_3/90_3/0_3/90_3/0_3]_s$ cross-plied curved composite laminates under bending moment. Fatigue experiments are conducted under displacement control in order to observe the crack propagation. The ultimate strength of the materials and the corresponding displacement values obtained from the static test results are used as reference values for each lay-up orientation. Failure mechanisms are investigated using micrographs and DSLR camera images. Load-displacement plots of the experiments until failure and failure patterns of the specimens are presented. In the all plots, the results of [0] UD laminates are designated with red lines and cross-plied laminates with black lines. The scale of the load-displacement plots are decreased since the load and displacement values are much smaller than the static loading cases.

5.1. [0] UD laminates

The first results belong to $[0]_{15s}$ UD curved composite laminates. The lay-up details are explained in the experimental method and material part. Two fatigue loading test results conducted under displacement control are presented in this section. The specimens show different behavior under fatigue loading than static loading case. The specimens carry higher loads for lower displacement values so that fatigue loading tests for [0] UD curved composite laminates are conducted under low displacement values. First fatigue test is belong to [0]_sp9 which is conducted with 5 mm maximum displacement at R-ratio of 0.5. **Figure 5.1** presents the load-displacement plot of the fatigue cycles until failure of [0]_sp9. The plot presents only the part of the cycles for simplicity. Although the maximum displacement is 5 mm, the specimen is under high stress and first stiffness reduction is experienced after 50 cycles. The maximum load drops to 60% of the initial maximum load at 5 mm displacement. The second stiffness reduction is observed in the 15000th cycle leading to the final failure of the specimen. This stiffness reduction only causes 15% of load capacity loss of the specimen. Initial slopes and slopes after load drops are marked and matched with the normal camera images.

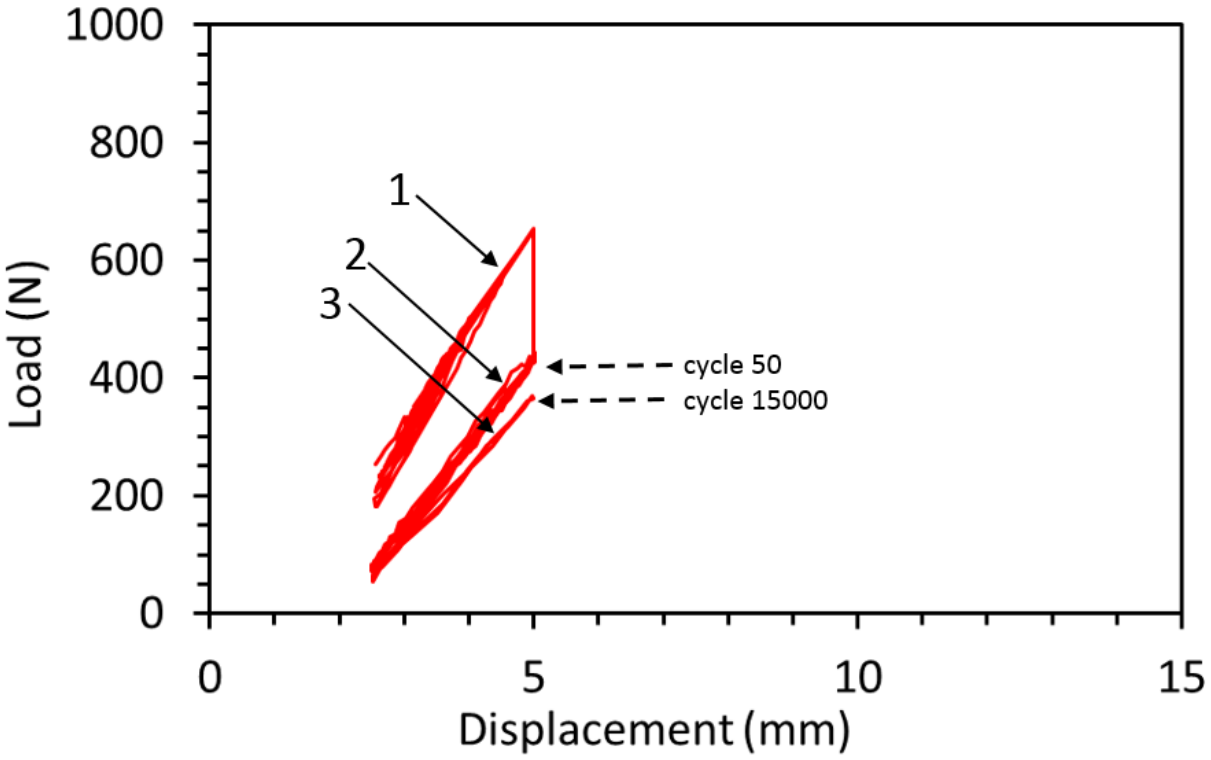

Figure 5.1 Load-displacement curves of [0]_sp9 with ongoing fatigue cycles until failure

The images taken after the load drops are presented in **Figure 5.2**. **Figure 5.2a** shows the initial form of the specimen without any damage corresponding to the first slope on the plot. The first load drop occurs suddenly with cracking sound. However, as shown in **Figure 5.2b**, after the first load drop there is no cracks or delaminations are formed in the edges of the specimen. After the first load drops, fatigue loading with the same displacement value is conducted on [0] UD curved composite specimen and after 1000 cycle, second load drop is observed with small delamination occurred in 67% of the thickness at the curved region (**Figure 5.2c**). This delamination corresponds to the final failure of the specimen. **Figure 5.2d** presents the micrograph of the same specimen. The delamination leading to the failure is thin and unclear so that it is marked on the micrograph. It can be seen easily that there is no damage sign except the delamination occurred at 0.67t of the thickness.

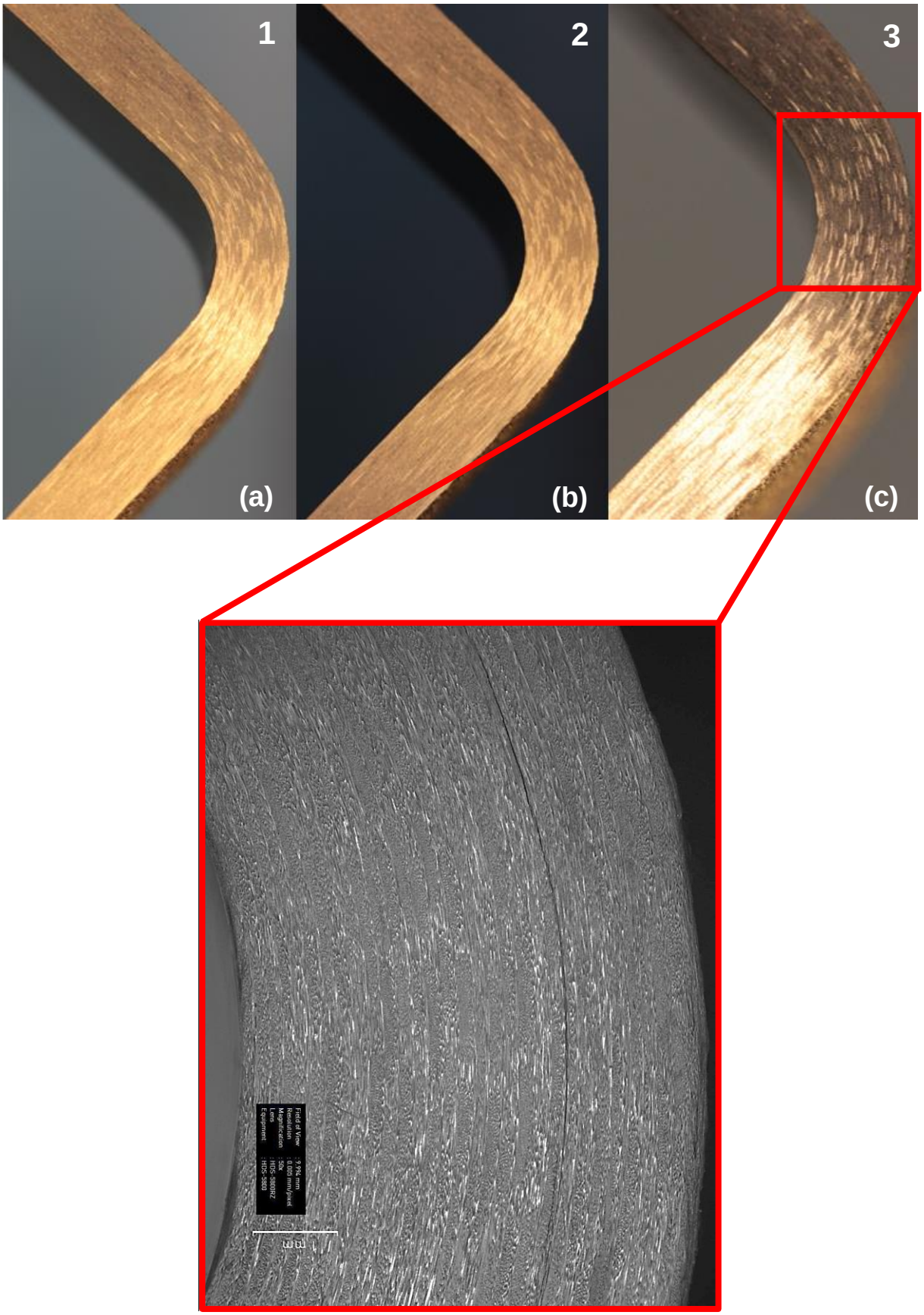

Figure 5.2 The images of [0]_sp9 under fatigue loading (a) Initial state; (b)After first load drop; (c) After failure; (d) The micrograph after failure

In order to understand the failure mechanism after the first load drop without any delamination observed, another fatigue test is conducted using [0] UD curved composite laminate with [0]_sp8. **Figure 5.3** presents the load displacement plot of the [0]_sp8 with ongoing cycles until the first stiffness degradation. 4 mm opening corresponds to over 800 N load so it is applied as maximum displacement at R-ratio of 0.5. The first slope corresponds to the initial stiffness of the material. Until the first load drop, the material preserve the initial stiffness so that the load-displacement plot includes only the last cycles of the initial slope and the first cycles of the remaining stiffness. The maximum load applied to the specimen is 850 N at 4 mm displacement. After 150000 cycles, [0] UD curved composite laminate experience the stiffness reduction. The maximum load at 5 mm displacement drops to its 65% after the first damage occurred. The load drop occurred after the first damage on specimen 8 is consistent with the first failure of specimen 9.

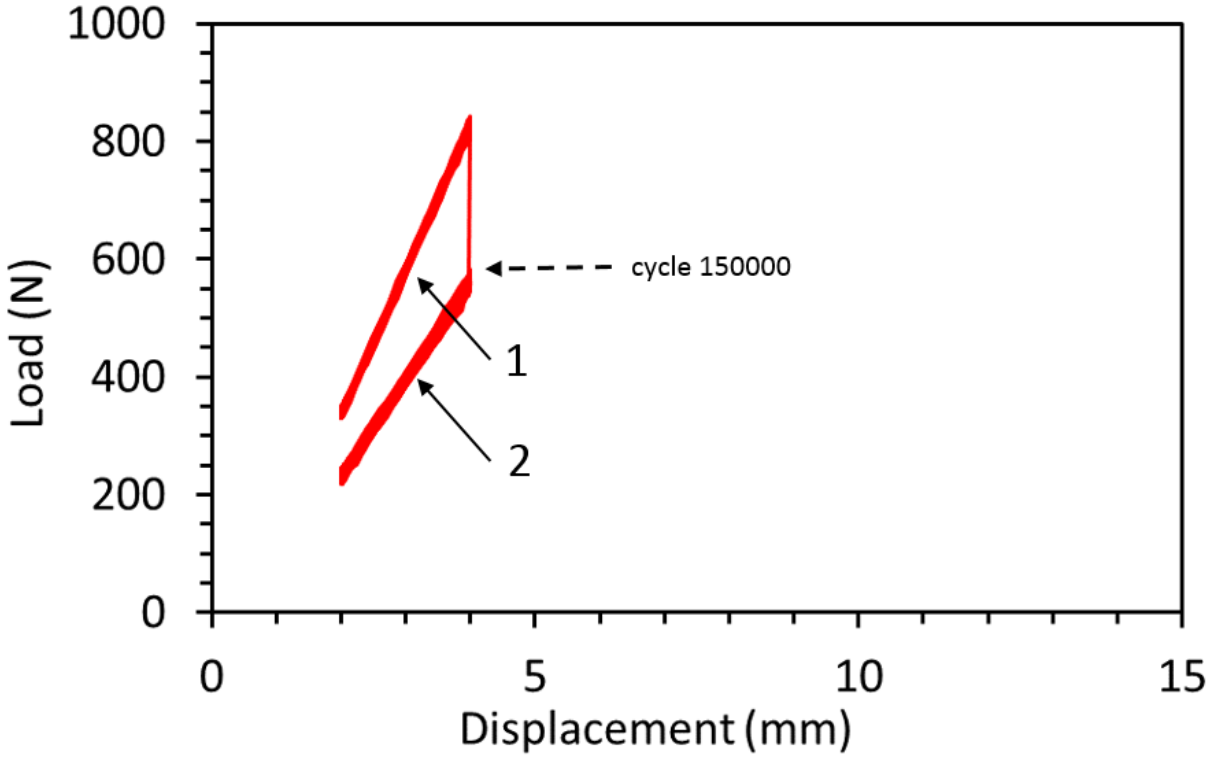

Figure 5.3 Load-displacement curves of [0]_sp8 with ongoing fatigue cycles

Figure 5.4a present the specimen without any damage corresponding to the initial slope on the load-displacement plot. **Figure 5.4b** is taken after the first load drop. As can be seen from the figure, there is no crack or delamination that can be seen from the lateral surface of the specimen. In order to investigate the source of the stiffness degradation, micrographs are taken (**Figure 5.4c**). As can be seen from the micrograph, there is no sign of any crack or delamination formed in the edges of the laminates. The marks on the surface correspond to the epoxy. Nondestructive testing is required to observe the interior damages. Through-transmission ultrasonic testing (TTU) is conducted on specimen 8 after the first stiffness degradation without any edge

delaminations. The details of NDT method is explained in Methodology chapter. Figure xx shows the results of TTU testing of [0]_sp8. **Figure 5.5a** presents the result of the initial state of the specimen as reference image and **Figure 5.5b** present the result of the specimen after the stiffness degradation. The images shows the top view of the specimen and the arrow marks the radius. The color differences in **Figure 5.5b** correspond to defects occurred in the specimen. It is clear that in the curved region interior delamination is formed. Delamination is arrested in the curved region and cannot proceed until the edges of the specimen. This interior damage explains the stiffness degradation occurred under fatigue loading.

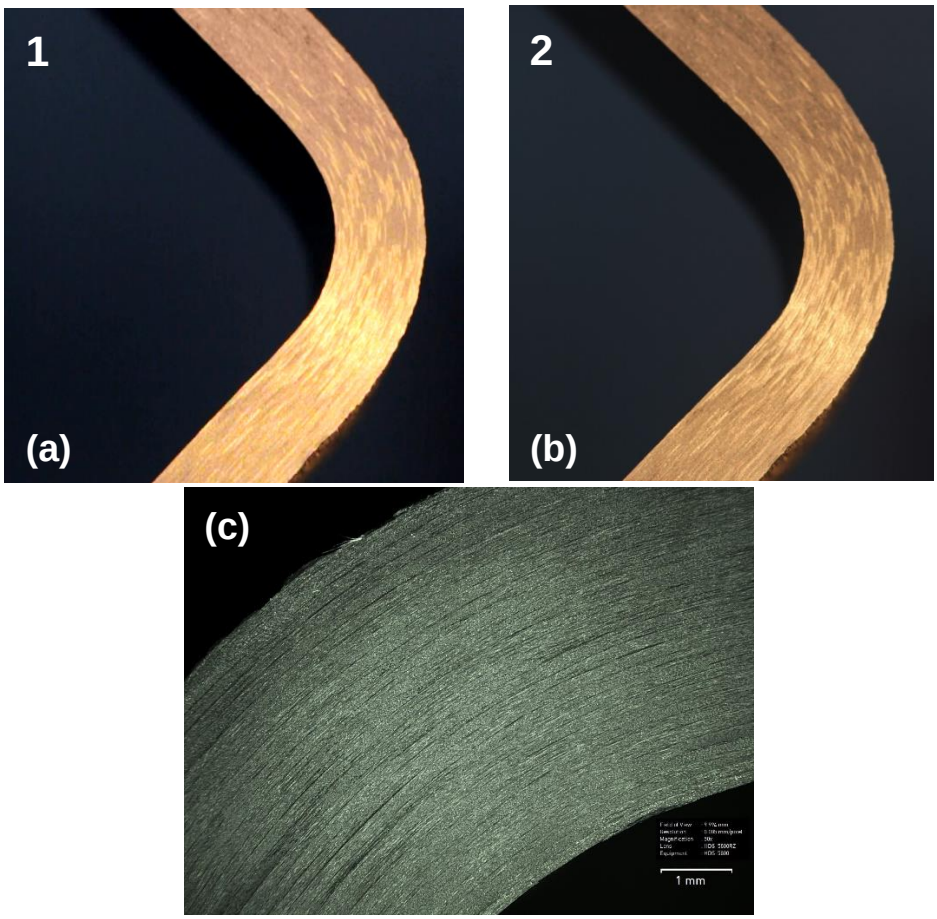

Figure 5.4 The images of [0]_sp8 under fatigue loading (a) Initial state; (b) After first load drop; (c) The micrograph after the first load drop

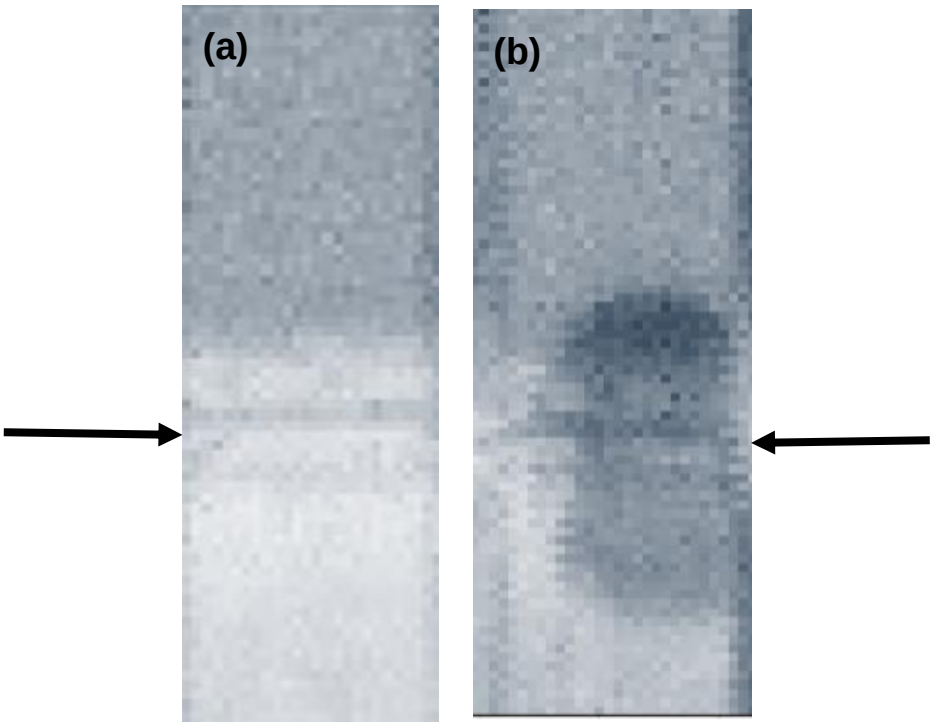

Figure 5.5 TTU test results (a) Initial state; (b) After first load drop

In **Table 5.1**, the slopes varying with the ongoing cycles are presented for both [0] UD specimens. The slopes corresponding to the stiffness of the materials are similar. Slight differences may be due to the difference in the loading rate. In order to investigate the stiffness reduction of [0] UD laminates until failure, the slope of the ongoing cycle for both fatigue loading specimens are calculated. The normalized stiffness values of [0]_sp9 until failure and [0]_sp8 until first failure are presented in **Figure 5.6**. As can be seen from the plot, [0]_sp9 experience the first load drop earlier than [0]_sp8. Although the fatigue resistance of specimens are different, the stiffness reduces to the same level, 60%, after the first load drop. It is observed that, the stiffness reduction which corresponds to the first damage is very sharp in both specimens. However, after first load drop, stiffness degrades gradually until failure which corresponds to gradual damage progression. However, failure on the lateral surface occurs sudden which may be caused by interior delaminations. After failure [0]_sp9 preserves 50% of its initial stiffness.

Table 5.1 The load-displacement curve slopes of [0] UD specimens under fatigue loading

Specimen	Initial Slope	2nd Slope	3Rd Slope
[0]_sp9	222.25	133.35	125
[0]_sp8	235.25	140.25	-

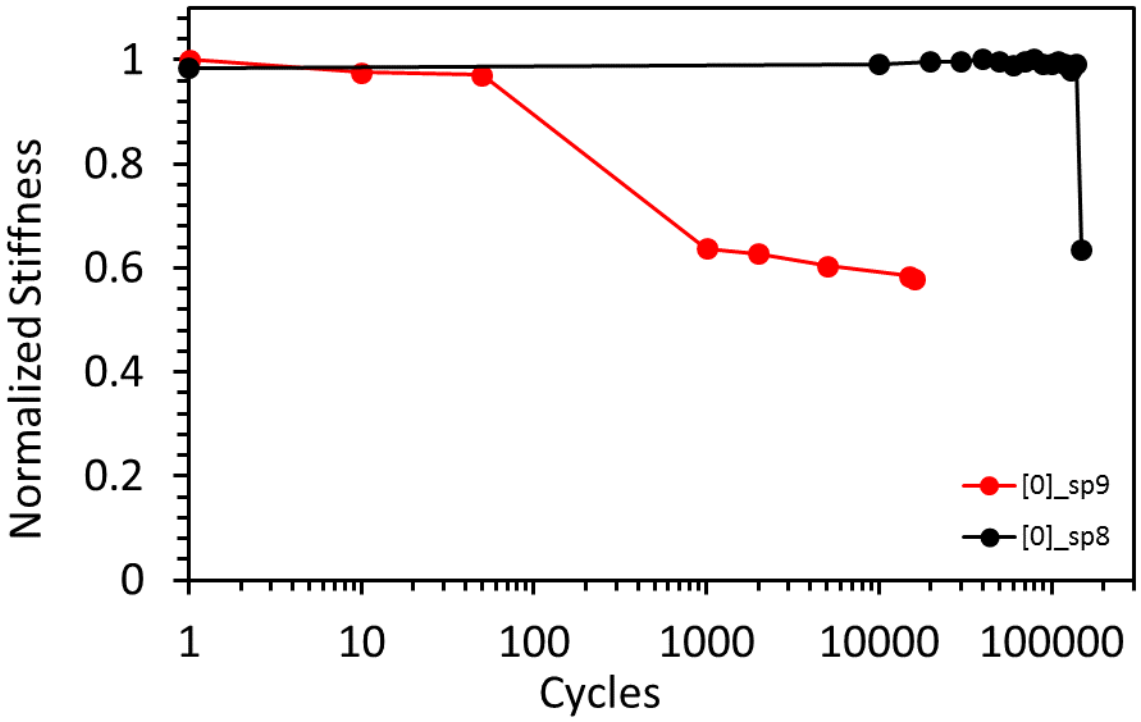

Figure 5.6 Normalized stiffness degradation with ongoing cycles of [0]_sp9 and [0]_sp8

5.2. Cross-plied laminates

Cross-plied specimens carry consistent load values with static loading case. The average ultimate strength of cross-plied laminates are decided as 650 N. Fatigue loading experiments are conducted at high stress states. **Figure 5.7** presents the load-displacement plot of [0/90]_sp8 under fatigue loading until failure. The experiment is conducted under displacement control with maximum displacement of 6.5 mm at an R-ratio of 0.5. The corresponding load value for 6.5 mm is 600 N which is 90% of the average ultimate strength of cross-plied laminates. The load-displacement plot shows all fatigue cycles until failure. The initial slope corresponds to the initial stiffness of the material. After 500 cycles, the first stiffness degradation is observed. The maximum load at 6.5 mm displacement drops to 300 N which corresponds to 50% of the initial maximum load. After the first load drop, it is observed that the load at minimum displacement value drops slightly. Although the stiffness value of the laminate degrades, cross-plied laminates preserve load carrying capacity with lower slope. Fatigue loading is conducted with the same maximum displacement value after the first load drop and the cross-plied specimen experience the second stiffness degradation in the 1500th fatigue cycle. The maximum load at maximum displacement drops to 200 N which corresponds to 65% of the remaining maximum load value. This load drop leads to final failure of the specimen and the maximum load capacity is only 35% of the initial maximum load value. After the second load drop, load value corresponding to the minimum displacement remains constant. The slope of the load-displacement plot corresponding to the stiffness of the material decreases which is

relatively less than the degradation after first load drop. The initial slope and the slopes after load drops are marked which correspond to the damage observed in the normal camera images.

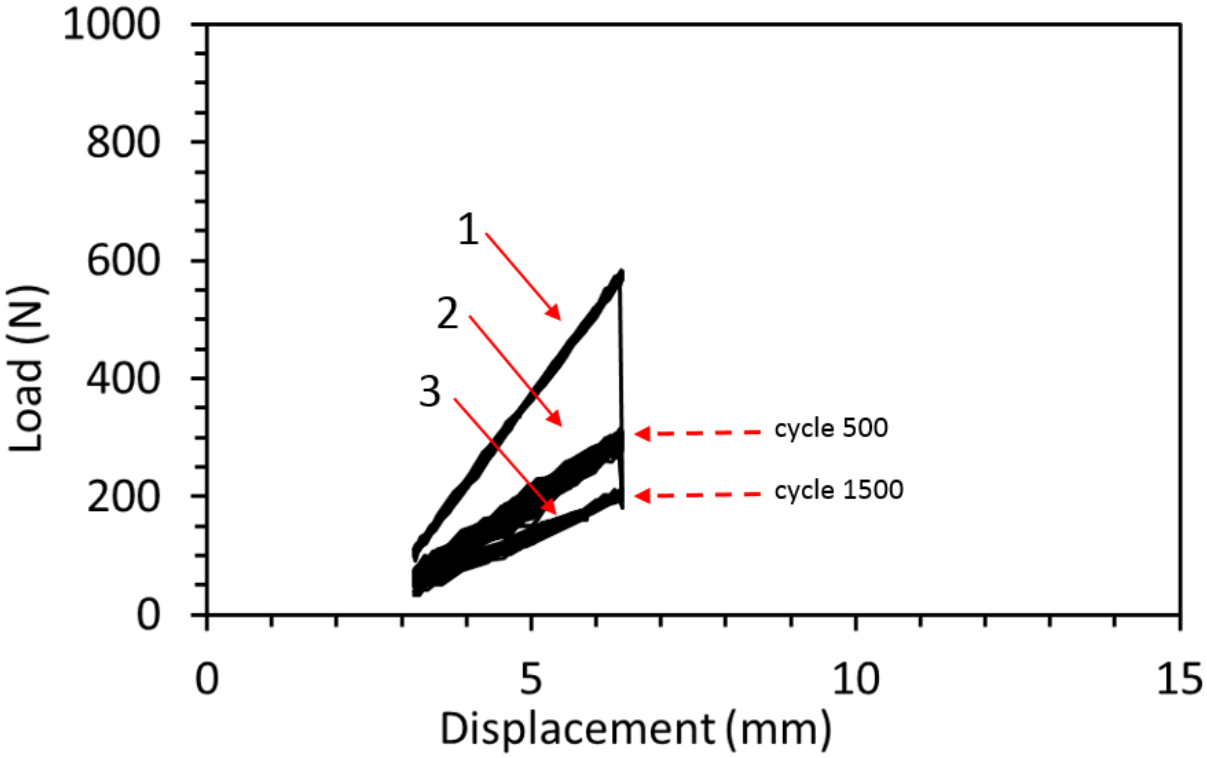

Figure 5.7 Load-displacement curves of [0/90]_sp8 with ongoing fatigue cycles until failure

The evolution of the damage under fatigue failure on [0/90]_sp8 is presented in **Figure 5.8**. The images are taken after every load drop using DSLR camera. **Figure 5.8a** shows the initial state of the specimen without any damage. This image corresponds to the initial slope on load-displacement curve of the specimen. **Figure 5.8b** presents the initial crack occurred in the second off-axis ply corresponding to the first load drop after 500 cycle. Since the first damage forms in the second 90º ply, high rate of stiffness loss is observed after the first load drop. The images are taken using normal camera so that the initiation and progression of the damage cannot be caught. However, as can be seen from **Figure 5.8b**, the failure pattern includes matrix cracking through the curved region and progressed delaminations through the arm. Matrix cracks initiate first and lead to the delaminations. Matrix crack proceed lead to delamination through the interface of the adjacent 0º ply to the upper arm. Matrix cracks continue as delamination through the lower arm. Delamination starts at the interface of the two plies and proceeds through the 0º ply. Delaminations do not progress through the arms, the crack tips are marked with the arrows. **Figure 5.8c** presents the failure pattern leading to the final failure of the specimen occurred in 1500th cycle. With the ongoing cycles, it is observed that the first damage occurred in the second off-axis ply remains constant. It is observed that damage is formed in the third off-axis ply corresponding to the second load drop and final failure. Matrix cracks are formed at

the curved region and they slightly proceed to the arms through the interface with the adjacent 0º ply. Both matrix cracking and delamination occurred in the third off-axis ply is smaller than the first damage. **Figure 5.8d** presents the micrograph of the lateral view of the specimen. The matrix cracks delaminations proceeding through the lower arm are seen easily.

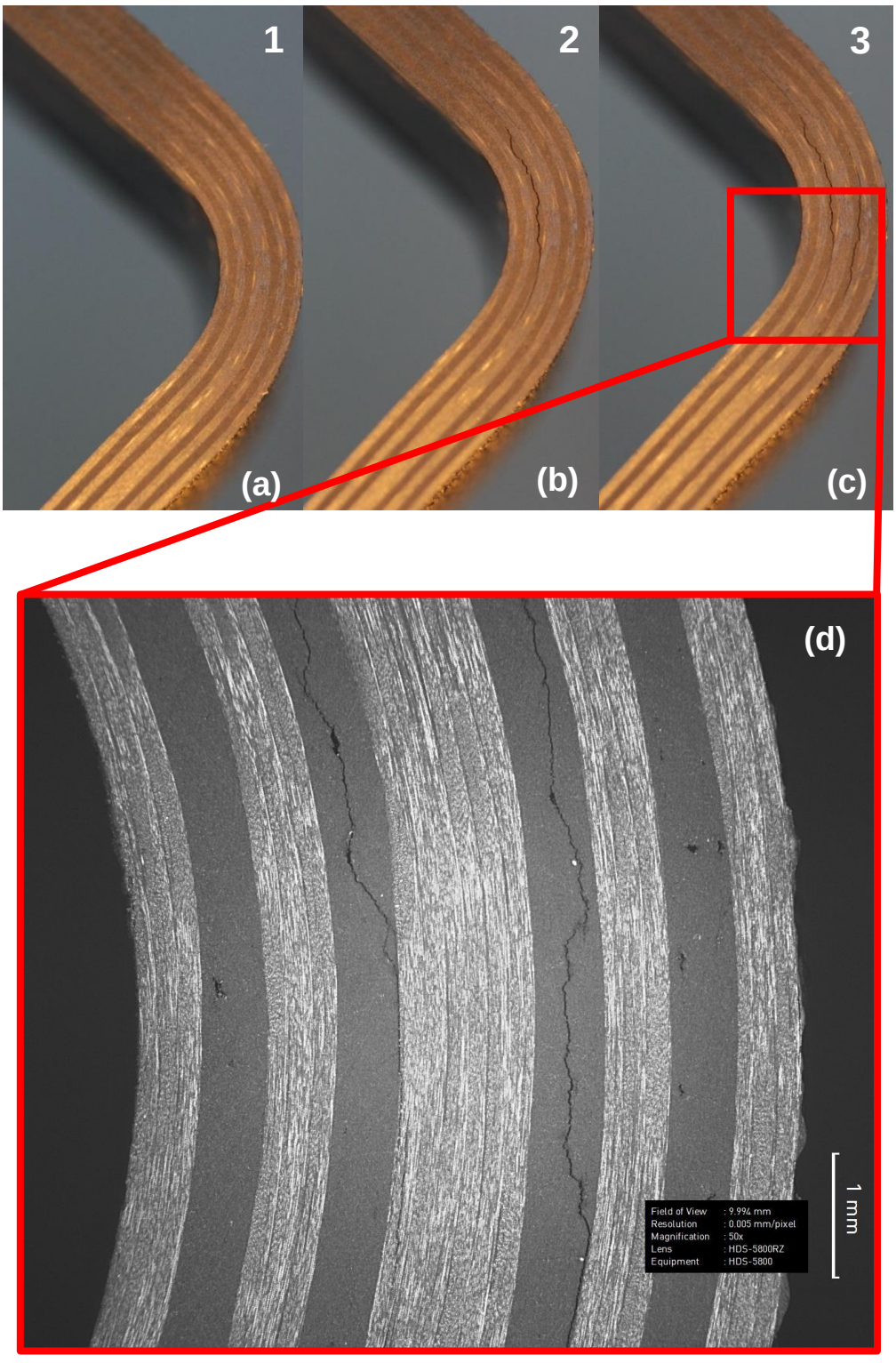

Figure 5.8 The images of [0/90]_sp8 (a)Initial state; (b)After first load drop; (c)After failure; (d)The micrograph taken after failure

In order to investigate the stiffness reduction of cross-plied laminates under fatigue loading until failure, the slope of the ongoing cycles are calculated for [0/90]_sp8 . The normalized stiffness values of [0/90]_sp8 until failure are presented in **Figure 5.9**Figure 5.6 . It is observed that, until damage initiation stiffness value remains constant with ongoing cycles. Then, stiffness degrades sharply which corresponds to sudden damage initiation not gradual damage progression. After the first load drop, the stiffness value is 48% of its initial value and after failure the only 32% of the maximum stiffness is preserved. The results are consistent with the results of load-displacement curve.

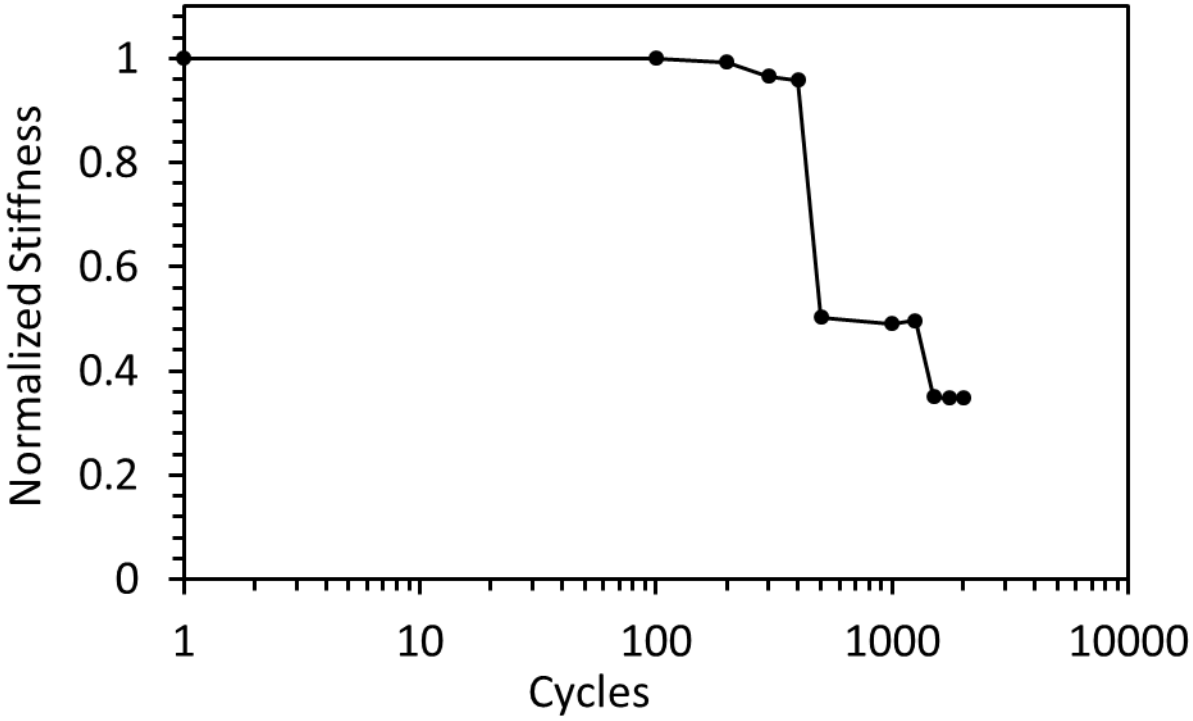

Figure 5.9 Normalized stiffness degradation with ongiong cycles of [0/90]_sp8

Chapter 6

DISCUSSION

In this chapter, the results of static loading and the results of fatigue loading presented in the previous chapters are compared with each other for [0] UD and [03/903/03/903/03]s cross-plied lay-up orientation. In Section 6.1, the static loading results of [0] UD and cross-plied laminates are compared to discuss two different lay-up orientations with the same thickness in terms of microstructure, load-displacement plots and the failure patterns. In Section 6.2, the results of [0] UD laminates under static and fatigue loading are compared to discuss the load displacement curves and failure mechanisms. In Section 6.3, the behavior of cross-plied laminates under static and fatigue loading are compared using the load displacement curves and micrographs. On the other hand, in Section 6.4, the effect of defects are compared for cross-plied laminates. The differences in load displacement plots and the differences in crack initiation location are discussed. In this chapter, the load-displacement curves are plotted using the same scale with static loading results chapter. The designations in the load-displacement plots are the same with the previous chapters, as red for [0] UD laminates and black for cross-plied laminates.

6.1. Effect of lay-up orientation under static loading

In this section, the effect of the lay-up orientation on failure mechanism under static bending moment loading is discussed. The results of [0]_sp2 from [0] UD laminates and [0/90]_sp4 from cross-plied laminates are compared as average results. According to the results, a dynamic delamination is occurred in both cases so that the included off-axis plies do not change the dynamic failure however, they affect the load carrying capacity. Figure 6.1 presents the load-displacement curves of [0]_sp2 and [0/90]_sp4 under static loading until failure. As can be seen from the plot, the initial slope of [0] UD laminate is slightly greater than the cross-plied laminate. [0] UD laminate can carry up to 1200 N, whereas the maximum load cross-plied laminate is 650 N. The difference between this load carrying capacity is due to the difference between the longitudinal modulus of the laminates. The greater longitudinal modulus provides strength to the laminates in the longitudinal direction and as presented in **Table 3.4** the longitudinal modulus of [0] UD laminates are higher than the cross-plied laminates. After the first failure the load carrying capacities are different as well. [0] UD laminates lose most of its load carrying capacity, the slope of the load-displacement curve degrades. The little steps are observed in the load-displacement curves after the first failure then second load drop occurs leading to the final failure. In contrast, cross-plied laminates carry load after first failure. Although the slope of the load-displacement curve slightly

decreases, the specimen carry load to the level which is close to the maximum load value then second load drop occurs leading to the final failure.

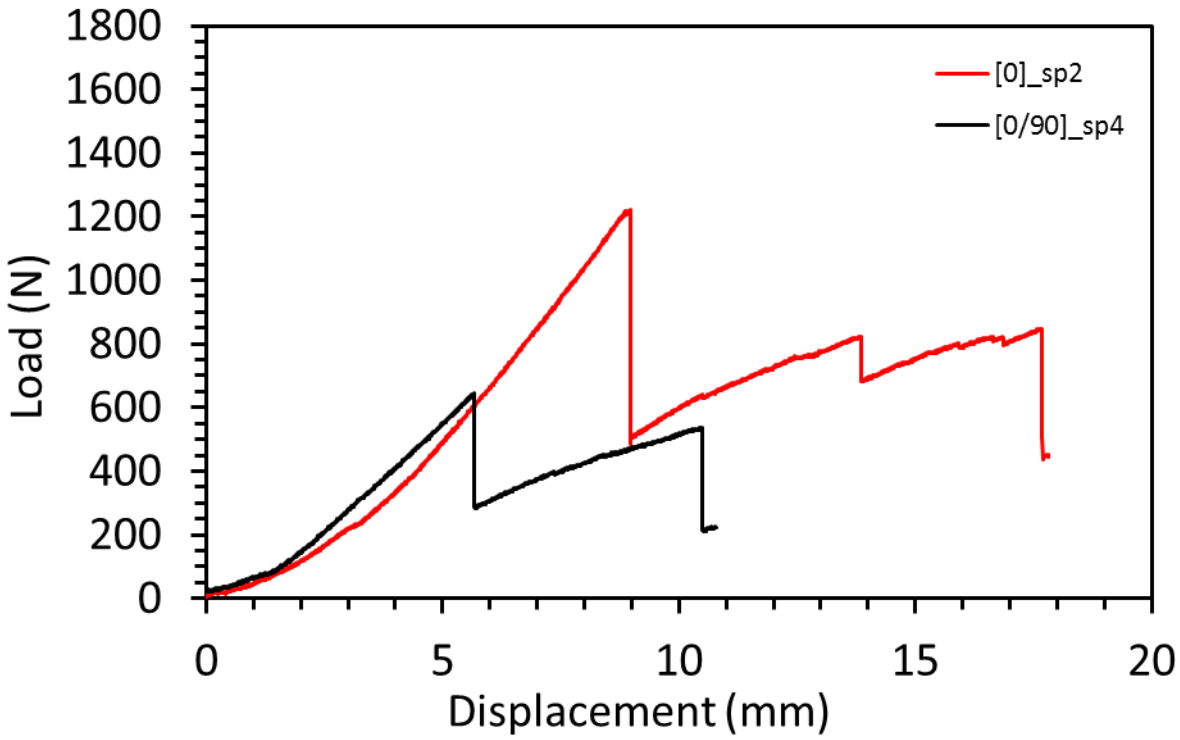

Figure 6.1 Load-displacement comparison of [0]_sp2 and [0/90]_sp4 under static loading

The results show that the failure mechanisms are different between two lay-up orientations. **Figure 6.2a** presents the damage evolution of [0]_sp2 from UD laminates and **Figure 6.2b** presents the damage evolution of [0/90]_sp4 from the cross-plied laminates. In [0] UD laminates the first delamination occurs at near the highest radial stress location, 0.35t corresponding to the first load drop where 0˚ plies are weak at that direction. In the second load drop, multiple delaminations are observed at the 0.4t of the remaining thickness again at the maximum radial stress location of the remaining ligament. However, in cross-plied laminates the failure initiates with matrix cracking in the interior off-axis ply where the highest tangential stress occurs and these matrix cracks weaken the lamina in the angular direction and lead to the delaminations at these points. In the second load drop, matrix cracks and delaminations are observed in the second and third off-axis plies instantaneously. However, the high speed camera images of [0/90]_sp2 proved that the failure is sequential which includes the first failure in the second 90˚ ply then the third 90˚ ply (**Figure 6.3**).

It is concluded that, the cross-plied laminates are more damage tolerant under bending moment loading. The load carrying capacity of cross-plied laminates is preserved more than [0] UD laminates. The stiffness value does not change, therefore, this is beneficial for design process.

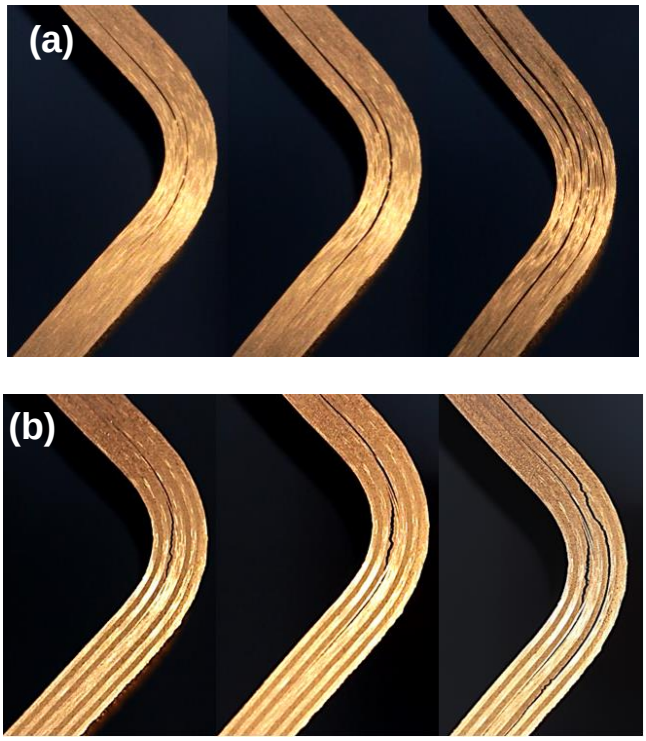

Figure 6.2 The damage evolution under static loading (a)[0]_sp2; (b)[0/90]_sp4

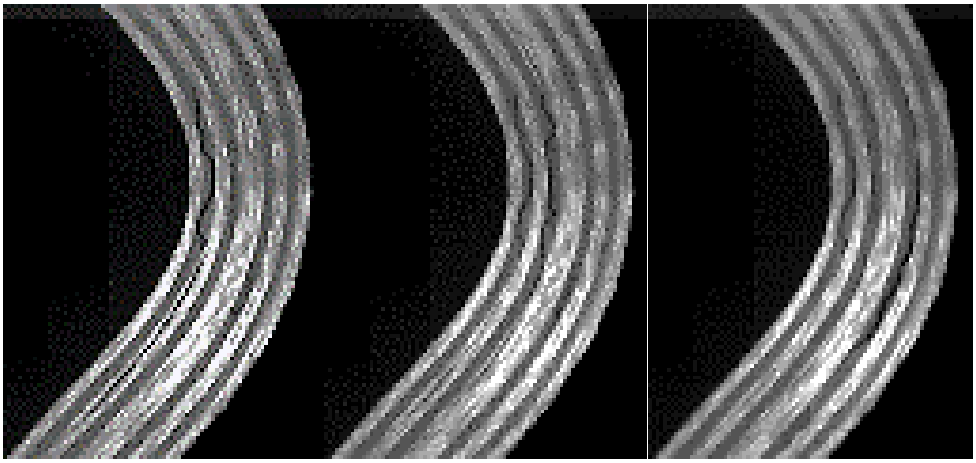

Figure 6.3 High speed camera images of [0/90]_sp2

6.2. Comparison of static and fatigue failure

6.2.1. Comparison of [0] UD laminates

In this section, the static and fatigue loading results of [0] UD curved composite laminates are compared. The load-displacement plots are compared; the slopes and load drops are discussed. The failure pattern of the specimens under static and fatigue loading are compared using DSLR camera images. **Figure 6.4** presents the load-displacement plot of [0] UD curved composite laminates under static and fatigue

loading. Fatigue loading cycles on the plot represents the results of [0]_sp9 and they are designated with red lines. Static loading results belong to [0]_sp2 and are represented with red dashed line. Static and fatigue load-displacement curves behave similar. However, as can be seen from the plot, there is a slight difference at the initial slope of static and fatigue loading curves. Since the slope is higher under fatigue loading, at 5 mm displacement [0]_sp2 carries 600 N load whereas [0]_sp2 carries only around 400 N. In two load cases, two load drops are observed. The first load drop is relatively greater than the second load drop under static and fatigue loading. Under fatigue loading, the load drops 400 N after loading cycles with constant maximum displacement of 5 mm. Under static loading, increasing displacement causes load drop as well which is equal to the first load drop level of fatigue loading. Under fatigue loading, after the first load drop, the remaining slope is almost the same with the initial slope of the static test specimen. After the first failure, static loading curve experience a small load drop corresponding to crack propagation, however, the slope of the curve remains constant. Then, [0]_sp9 experience the final failure and the specimen lose almost all its stiffness. However, under fatigue loading the specimen experience small load drop leading to the failure of the specimens. The final slope of the load-displacement curve of the fatigue loading is higher than the remaining slope of the static loading specimen after failure. Table 6.1 presents the slopes of [0]_sp9 and [0]_sp2 until failure. Under fatigue loading, the slopes of the curves are greater than the slope of the static loading specimen from the initial state until failure.

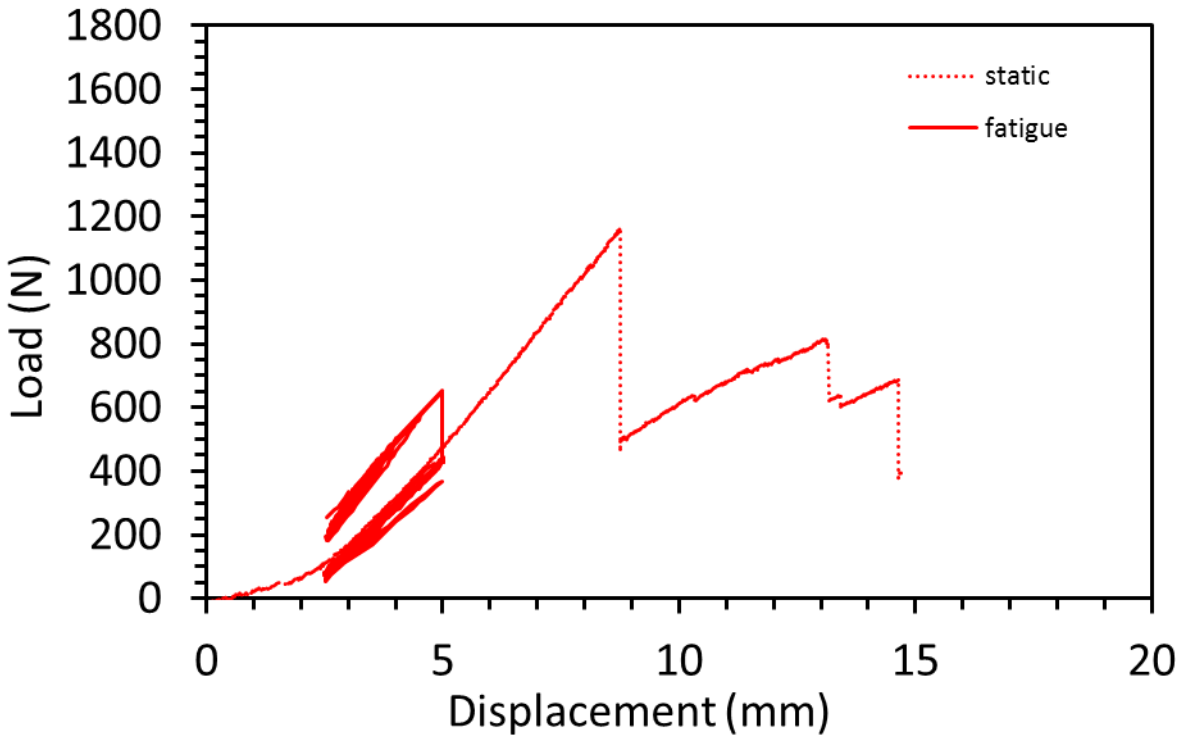

Figure 6.4 Load-displacement curves of [0]_sp2 and [0]_sp9 until failure

Table 6.1 Slope of load-displacement curves; [0]_sp2 and [0]_sp9

Specimen	Loading Condition	Initial Slope	2nd Slope	3Rd Slope
[0]_sp2	Static	187.5	80	42
[0]_sp9	Fatigue	222.25	133.35	125

The difference in the failure mechanisms are presented in **Figure 6.5**. Both images represents the final failure of [0] UD curved composite laminates; **Figure 6.5a** shows the static failure and **Figure 6.5b** presents the failure occurred after fatigue cycles. The failure mechanisms are obviously different than each other. In **Figure 6.5a**, multiple delaminations on [0]_sp2 can be seen easily which occur under static loading. **Figure 6.5b** shows the final failure of [0]_sp9 under fatigue loading. The delamination corresponding to the fist load drop cannot be seen from the lateral view of the specimen. However, under static loading first load drop is in combination with delamination through the specimen length at 0.35t of the specimen. With another fatigue loading experiment, it is observed that, the load drop on the load-displacement plot corresponds to interior delamination. Under fatigue loading the first damage occurs inside and it initiates from the mid-point of the curvature. As can be seen from **Figure 6.5a**, the second major delamination occurs at 0.75t in combination with small delaminations through the thickness at the curved region which lead to the final failure of the specimen under static loading. Although the failure comes with the multiple and arm-length delaminations under static loading, under fatigue loading the only failure pattern observed from the lateral surface of the specimen is an arrested and thin delamination at the 0.75t of the curved region of the specimen. The second delamination corresponding to the final failure occurred under both static and fatigue loadings are at the same location. However, the damage progression under fatigue loading totally differs from the fatigue failure.

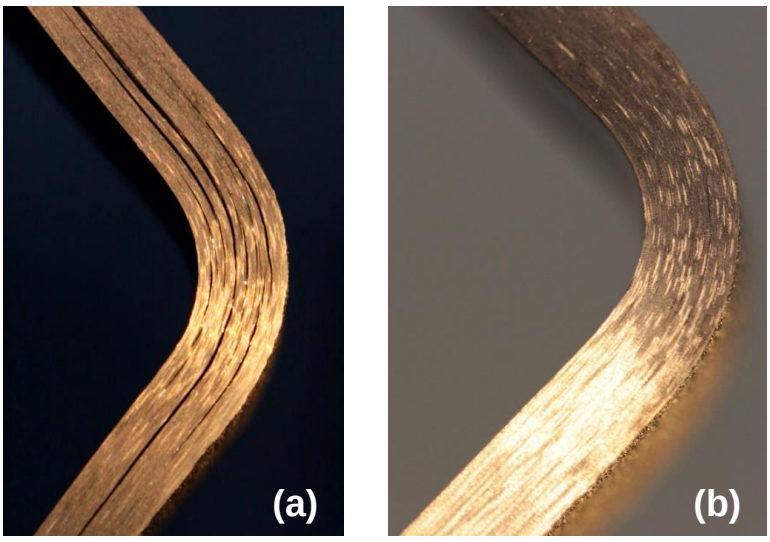

Figure 6.5 (a) Static failure; (b) Fatigue failure

6.2.2. Comparison of cross-plied laminates

In this section, the static and fatigue loading results of $[0_3/90_3/0_3/90_3/0_3]_s$ cross-plied curved composite laminates are compared. The load-displacement plots are compared; the slopes and load drops are discussed. The failure pattern of the specimens under static and fatigue loading are compared using DSLR camera images. In order to compare the results of static and fatigue loading appropriately, [0/90]_sp4 from static results and [0/90]_sp8 from fatigue results are chosen since both specimens have damage on the same plies. **Figure 6.6** presents the load-displacement plot of cross-plied curved composite laminates under static and fatigue loading. Fatigue loading cycles on the plot representing the results of [0/90]_sp8 are designated with black lines. Static loading results belonging to [0/90]_sp4 are represented with black dashed line. The load-displacement curves of the static and fatigue loadings behave similar. The initial slope of the load-displacement curves of both static and fatigue loading cases are almost the same. It can be easily seen that, the stress state is 90% of the peak stress of the static loading. After low number of fatigue cycles, the first stiffness degradation occurs. Under static loading, around the same displacement value, the specimen experience the first failure corresponds to the first load drop. As can be seen from the graph, the maximum load at maximum displacement level after the first load drop under fatigue loading is equal to where the peak load drops after first failure under static loading. The remaining stiffness of the fatigue loading specimen is the same with the remaining stiffness of the static loading specimen as the slope of the curves are equal after the first failures. Under static loading, [0/90]_sp4 carry load with increasing displacement until almost the peak load value then experience the second load drop. [0/90]_sp8 resists to fatigue cycles with remaining stiffness then the second load drop occurs. As the first load drop, the load value is the same under static and fatigue loading where the remaining maximum load drops after final failure. The slopes of static and fatigue curves are the second load drop corresponding to the remaining stiffness value after the final failure of both specimens. The corresponding slopes calculated from the load-displacement curves of [0**/**90]_sp4 under static loading and [0/90]_sp8 under fatigue loading are presented from the initial state until failure in **Table 6.2**. As can be seen from the table, although only slight difference is observed in the initial slopes, the slopes corresponding to the stiffness values after each load drops are similar.

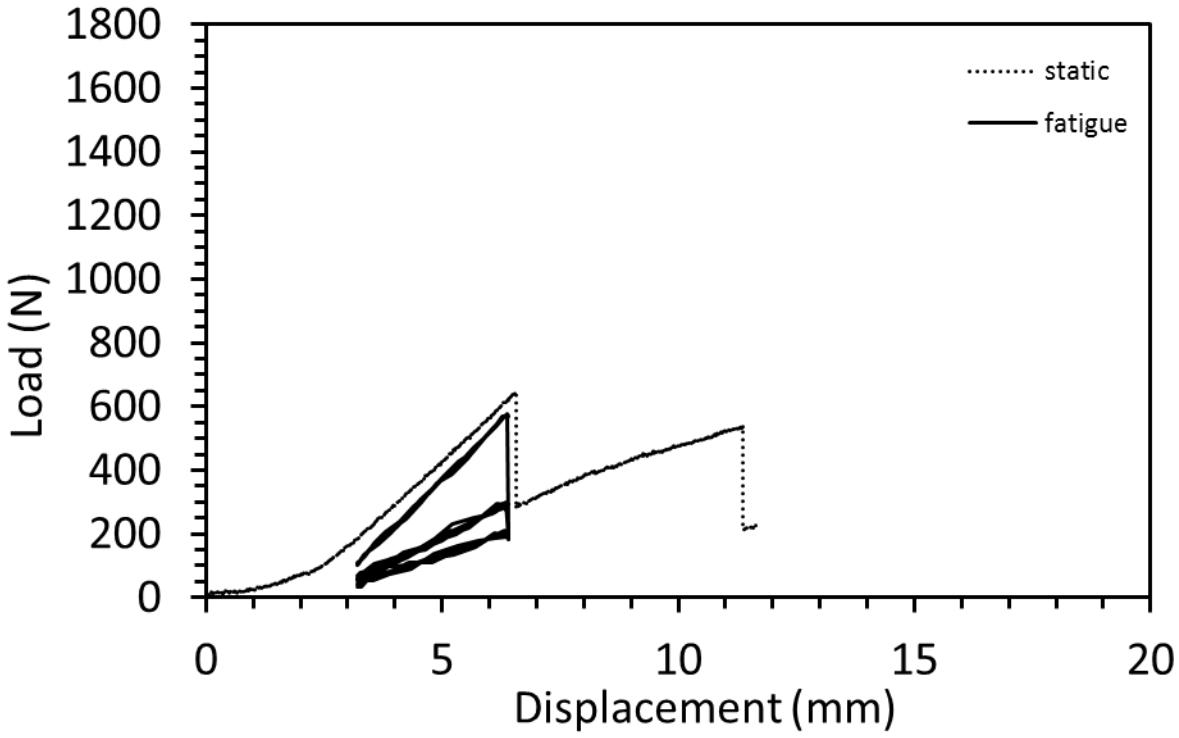

Figure 6.6 Load-displacement curves of [0/90]_sp4 and [0/90]_sp8 until failure

Table 6.2 Slope of load-displacement curves; [0/90]_sp4 and [0/90]_sp8 until failure

Specimen	Loading Condition	Initial Slope	2nd Slope	3Rd Slope
[0/90]_sp4	Static	160	68.95	40.80
[0/90]_sp8	Fatigue	147	71.40	42.70

The difference in the failure mechanisms are presented in **Figure 6.7**. Both images represents the final failure of cross-plied curved composite laminates; **Figure 6.7a** shows the static failure of [0/90]_sp4 and **Figure 6.7b** presents the failure occurred after fatigue cycles on [0/90]_sp8. In the images representing the failure mechanisms of static and fatigue loading show similarities. In both cases, the damage occurred in the second off-axis ply corresponds to the first load drop and the damage occurred in the third off-axis ply corresponds to the second load drop leading to the failure of the specimens. Under static loading, matrix cracks initiate in the second 90˚ ply at the curved region and proceed as delaminations through the adjacent 0˚ ply. The crack tip on the upper arm can be seen, however, the delamination progress through the lower arm. Under fatigue loading, similar matrix cracks are observed at the curved region corresponding to the first load drop. Matrix cracks form through the off-axis ply and the length is greater than the static failure. Matrix cracks lead to the delaminations proceeding through the adjacent 0˚ ply as static failure. However, both delaminations stop after proceeding short distance in contrast of the delaminations occurred under

static loading. The second delamination occurred in the third 90˚ ply (**Figure 6.7a**) is formed under static loading and matrix cracks initiated at the upper curved region of the specimen and in both arms, matrix cracks lead to delamination proceeding through the interface with the adjacent 0˚ ply which progress until the end of both arms. However, the biggest difference between the static failure and the damage occurred under fatigue loading leading to the final failure of [0/90]_sp8 is the crack length. The matrix cracks initiate at the curved part and lead to delamination, however, delaminations are arrested in the curved region of the fatigue loading specimen. The progress of the delaminations are similar with the behavior of the first delaminations under fatigue loading which is tend to be proceeding through the adjacent 0˚ ply to the both arms.

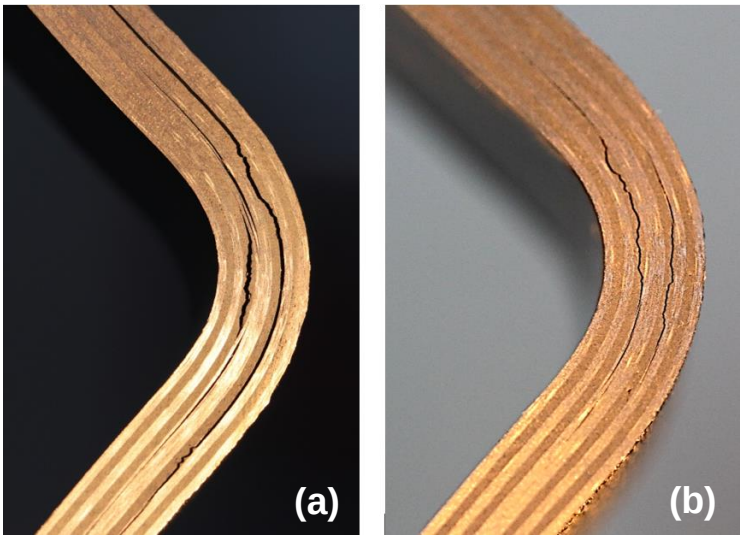

Figure 6.7 The final failure pattern (a) [0/90]_sp4; (b) [0/90]_sp8

6.3. Effect of defects

In this section, the effect of defects occurred during manufacturing process, especially in cross-plied laminates are discussed. Hand lay-up technique is more defect prone since human errors are included during the process.

As proposed in the study conducted by Uyar et al. [45], under static loading, cross-plied laminates are expected that the failure initiates at the interior off-axis ply where the maximum tensile stress occurs corresponding to the first failure. After the first failure, the remaining fibers carry load and peak load value before the second load drop is expected to be close to the initial maximum load value then second failure occurs at the second off-axis ply since tensile stress is now the highest at that location. After the second load drop, cross-plied laminates show the same characteristic and the third damage is expected to progress in the third 90˚ ply. The last off-axis ply is under compression loading and no failure is expected to be observed.

In contrast, in this study, some specimens show different behavior than expected under static and fatigue loading. The failures in these specimen initiate in the mid off-axis plies, not in the interior one so that these specimens cannot be used in the results. However, after investigating the initial images and micrographs of the specimens with the failure patterns, it is understood that this unexpected behavior is due to the voids formed in the off-axis plies.

Figure 6.8a presents the initial state of [0/90]_sp7 of cross-plied laminates before fatigue loading experiment. The image is taken using DSLR camera and the defects formed as voids can be seen on the third off-axis plies at the curved region. In order to investigate the defects, the micrograph of the curved region is taken (**Figure 6.8b**). As can be seen from the micrograph the voids are present in the third off-axis ply at the curved region. The critical size voids seen in the normal camera image are matched with the voids seen in the micrograph.

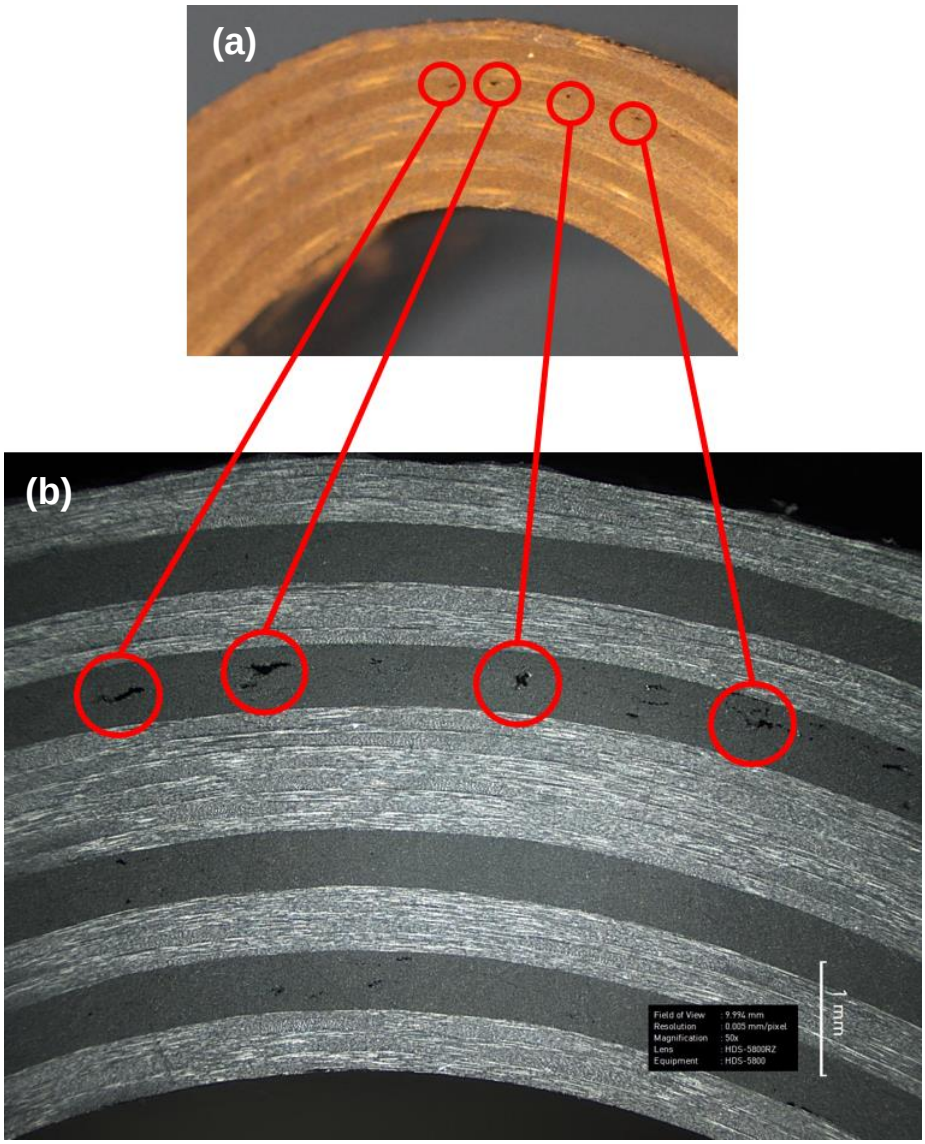

Figure 6.8 The initial state of [0/90]_sp7 (a) DSLR camera image; (b) Micrograph of curved region

The DSLR camera image after the first failure of [0/90]_sp7 occurred under fatigue loading corresponding to the first load drop is presented in **Figure 6.9a**. As can be seen from the figure, the failure initiates not in the highest tensile stress location but in the third 90° ply. From the normal camera image, it is observed that the matrix cracks pass through the voids. **Figure 6.9b** shows the final failure of the specimen occurred after fatigue cycles. The second damage corresponding to the final failure occurs at the interior off-axis ply where the tensile stress is maximum as expected. Figure 6.92c presents the micrograph of the curved region of [0/90]_sp7 after failure. The damage in the third off-axis ply corresponding to the first load drop occurs due to the void presence in the critical location, although the higher tensile stress is in the interior off-axis ply. The matrix cracks initiated from the voids which is seen in the normal camera image are matched with the micrograph of the curvature.

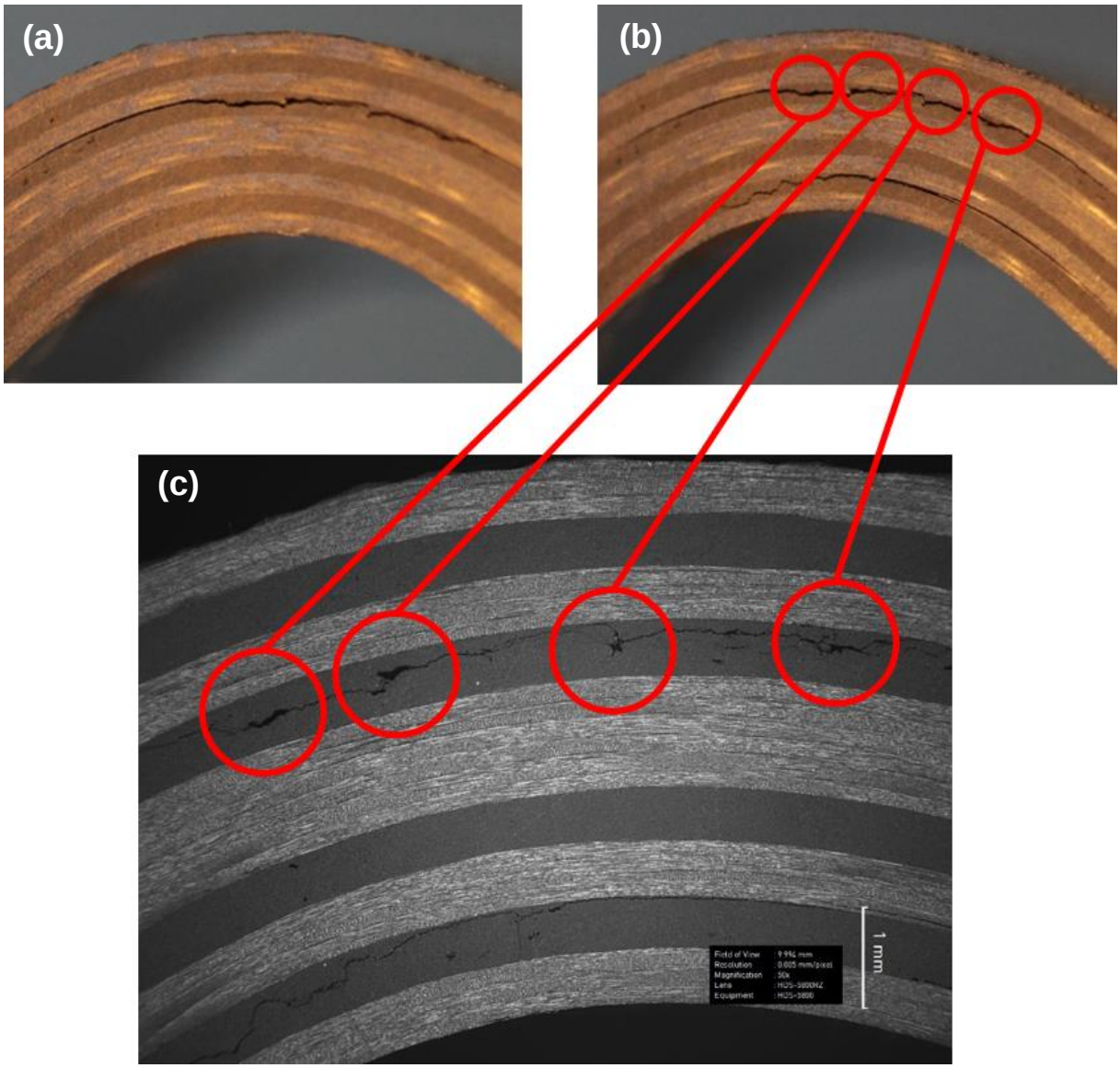

Figure 6.9 [0/90]_sp7 (a) DSLR camera image after first load drop; (b) DSLR camera image after failure; (c) Micrograph taken after failure

The same unexpected behavior is observed not only under fatigue loading but also under static loading. Under static loading, the failure occurred in [0/90]_sp4 is different than expected. In order to investgate this damage behavior, the initial state of the specimen is investigated using normal camera images and micrographs. **Figure 6.10a** represents the initial state of [0/90]_sp4 of cross-plied laminates before the static loading experiment. The image is taken using DSLR camera. If the normal camera image is investigated in detail, the void can be seen in the second off-axis ply. The void exists at the critical curved region and it is marked with the red circle. In order to investigate the location and size of the void, the micrographs are taken before the static loading experiment (**Figure 6.10b**). As can be seen from the micrograph, in the interior off-axis ply, many defects are observed which are occurred only at the surface. In the second 90˚ ply, the defects formed as voids can be seen easily. The void seen in the normal camera image is matched with the one in the micrograph and the other voids are marked with red circle.

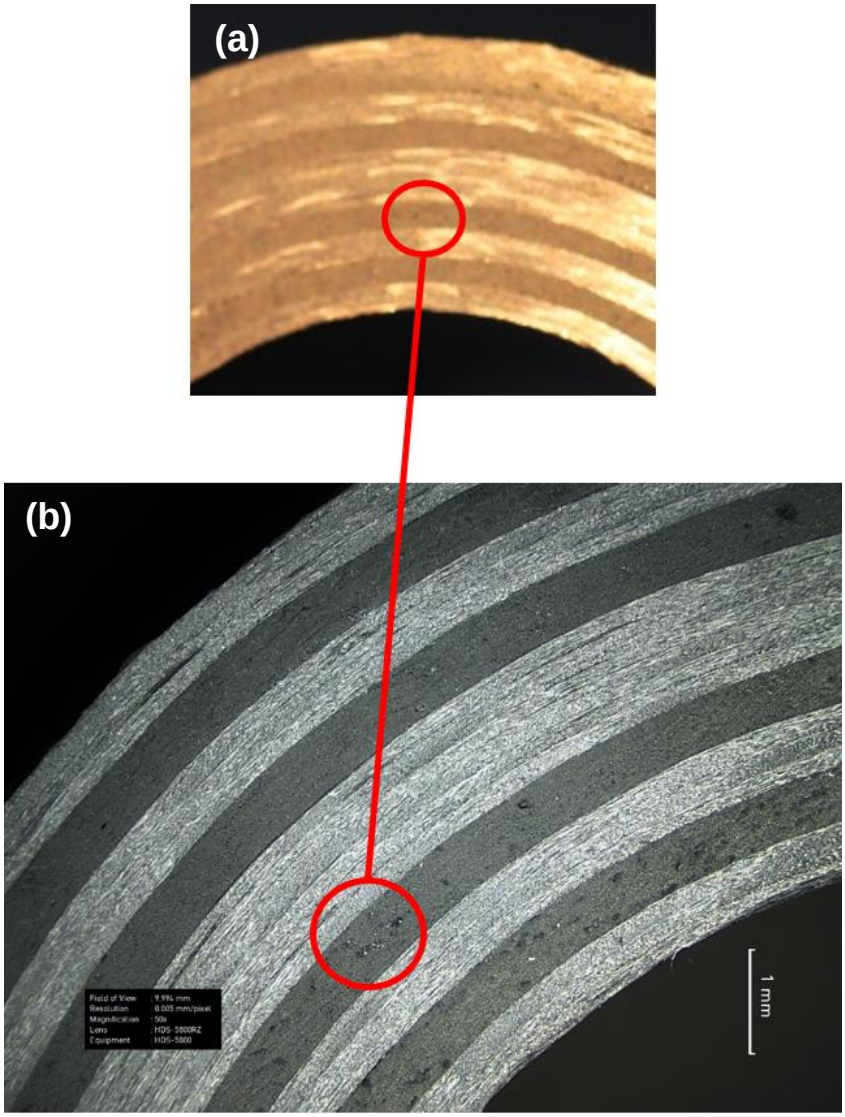

Figure 6.10 The initial state of [0/90]_sp4 (a) DSLR camera image; (b) Micrograph of curved region

The DSLR camera image after the first failure of [0/90]_sp4 occurred under static loading corresponding to the first load drop is presented in **Figure 6.11a**. As can be seen from the figure, the failure initiates not in the highest tensile stress location but in the third 90^{p} ply. The void size is small so that it is impossible to understand from the normal camera images whether the matrix initiation is caused by these voids. **Figure 6.11b** shows the final failure of the specimen occurred after fatigue cycles. The second damage corresponding to the final failure occurs at the third off-axis ply, since after the first failure the remaining thickness carries load and the highest stress occurs at that location causing the failure. **Figure 6.11c** presents the micrograph of the curved region of [0/90]_sp4 after failure. The damage in the second off-axis ply corresponding to the first load drop occurs due to the void presence in the critical location, although the higher tensile stress is in the interior off-axis ply. It can be easily seen that the matrix cracks initiate from the voids which cannot be observed in the normal camera image. The voids leading to matrix cracking are marked with red circles.

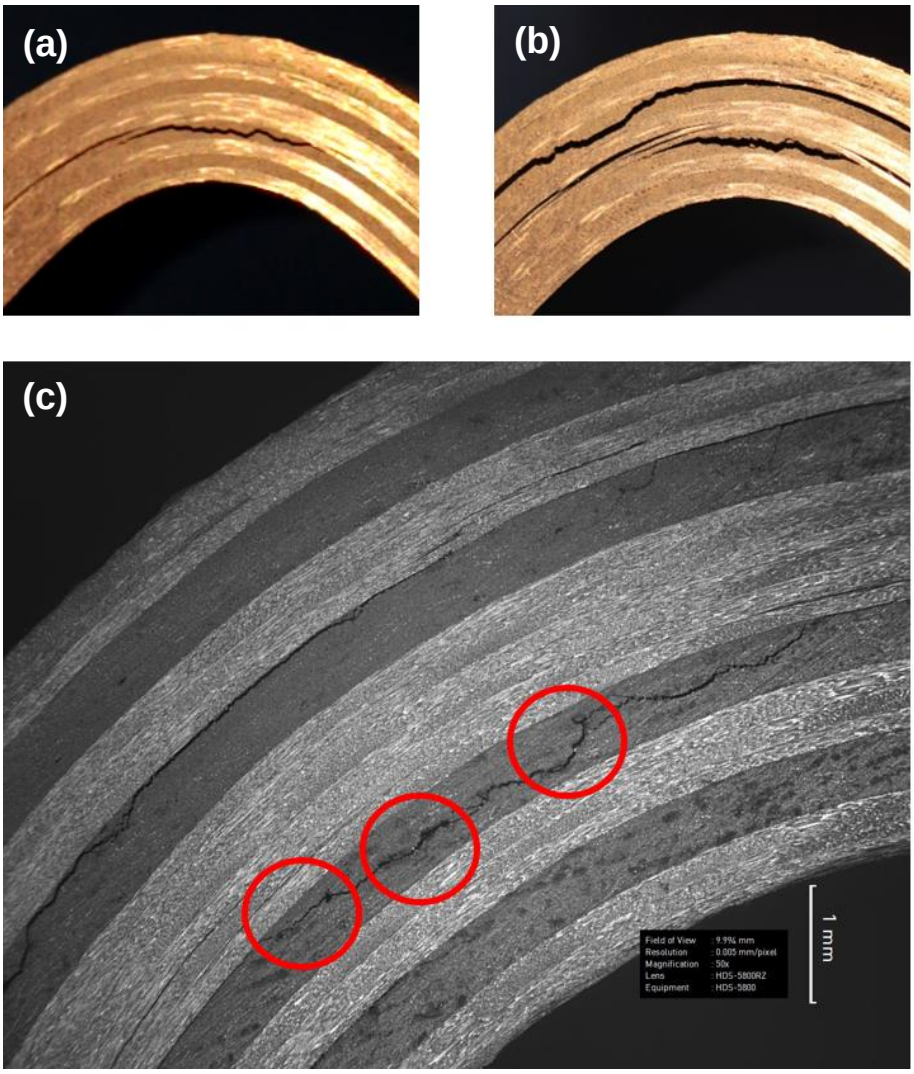

Figure 6.11 [0/90]_sp4 (a) DSLR camera image after first load drop; (b) DSLR camera image after failure; (c) Micrograph taken after failure

Chapter 7

SUMMARY AND CONCLUSION

7.1. Summary

In this thesis, fatigue behavior of curved composite (CFRP) laminates with different lay-up orientations under bending moment is investigated experimentally. In the first chapter, application of composite materials and curved composite laminates in aircraft and wind turbine industry is discussed. Fatigue characteristics of composite materials and conventional metals are compared. Fatigue resistance of composite laminates are superior to metals, so that metal support elements in aerospace industry have been replaced with curved composite laminates. The examples of curved composite laminate sub-components are given in detail. Service loads on wing box structure which causes fatigue on these components are defined. Curved composite laminates have different failure mechanisms than conventional metals under fatigue loading. The primary source of failure in these materials is delamination through the curved region in combination with matrix cracking in off-axis plies due to the low through-the-thickness properties of curved composite laminates. These failures are induced from the flight loads which can be reduced to three simple loading case namely, axial loading (P) which is parallel to the arm, shear loading (V) which is perpendicular to the arm length and moment loading (M). In this study, it was focused on failure induced from the moment loading created at the curved region of the composite laminates.

With this aim, a literature research is conducted related to fatigue damage progression in flat specimens and fatigue damage prediction in curved composite laminates. The studies in the literature on curved composite laminates under bending moment are not damage mechanism based but generally consist of interlaminar tensile fatigue properties and models for delamination initiation and progression. Studies are generally focused on generating SN curves which corresponds to delamination onset. There is a lack of knowledge about failure mechanism and damage progression under fatigue loading and comparison with static loading failure. There is an ASTM standard to find interlaminar tensile strength of curved composite laminates, however, in this study for simplicity, bending moment is obtained by applying axial force from both tips of the specimens since this study focuses on investigation of failure mechanism. A special fixture is designed to apply axial load to the specimens using universal test machine. In the third chapter, the loading case and the loading fixture are explained in detail. Static loading experiments are conducted as well in order to obtain the ultimate strength of the material to use in fatigue experiments. Monitoring of the failure is conducted with high speed camera system. The experimental procedure and specimen configuration for static and fatigue loading experiments are explained in chapter 3 in detail. Two different lay-up orientations are selected for the experiments namely [0] UD

curved specimens as fiber dominated laminates and cross-plied $[0_3/90_3/0_3/90_3/0_3]_s$ curved specimens as matrix dominated laminates. The manufacturing of the specimens is conducted in cooperation with TAI. In chapter 4, the preliminary tests, which are conducted using 25-ply [0] UD curved laminates, are explained. During experiments load-displacement data are recorded. The dynamic delamination is captured by high speed camera with 210000 fps. The delaminations occurred under static and fatigue loadings also captured by DSLR camera. The load displacement plots of the static and fatigue tests are presented. The failure mechanisms are investigated and compared for different lay-up orientations and loading cases. Finally, the effects of defects are discussed which leads to unexpected failure patterns on cross-plied laminates.

7.2. Conclusions

In this thesis, fatigue behavior of curved composite (CFRP) laminates with different lay-up orientations: $[0]_{15s}$ UD and $[0_3/90_3/0_3/90_3/0_3]_s$ curved composite laminates are investigated experimentally under bending moment. The goal of this thesis is to observe the failure mechanisms under fatigue loading and compare the differences with the static failure.

In experimental work, static loading experiments are conducted on each lay-up orientations in order to obtain the average ultimate strength of the material to use in fatigue loading experiments. Moreover, the failure patterns occurred under static loading are investigated. In order to examine the damage mechanisms, DSLR camera images, high speed camera images and micrographs are used. The maximum failure loads, stiffness of the load-displacement curves and load drops until failure are observed. Under static loading, load drops are observed which correspond to crack growth on both [0] UD and cross-plied curved laminates. However, load-displacement curve behaviors and failure patterns show differences between two lay-up configurations. The initial slope of fiber dominated [0] UD laminates which corresponds to the initial stiffness is greater than the initial stiffness of matrix dominated cross-plied laminates, since the longitudinal modulus of [0] UD laminates are higher. Cross-plied laminates experience the first load drop corresponding to the first failure earlier than [0] UD laminates. However, after first load drop, the cross-plied laminates preserve most of its stiffness, whereas [0] UD laminates lose most of its load carrying capacity. Cross-plied laminates experience the second load drop at the load value which is close to maximum load observed. However, the maximum load which [0] UD laminates reaches after first load drop is only 65% of its peak value. Although the maximum load that [0] UD laminates carry is higher than the maximum load of cross-plied laminates, cross-plied laminates are more damage tolerant since they preserve most of their initial stiffness after failure.

The failure patterns corresponding to the load drops show differences for each lay-ups. The failure occurs in cross-plied laminates in the interior off-axis ply where the tensile stress is maximum and in every load drop damage is formed in the off-axis plies sequentially. The results are consistent with the previous studies. In the previous studies, and preliminary tests, delamination occurs in the 0.4t of [0] UD laminates, then the specimens lose almost all of their stiffness value. In the preliminary tests, only one load drop occurs when the maximum load is 1650 N average. However, in this study, delamination initiates at 0.35t of $[0]_{15s}$ UD laminates, then the remaining thickness carries load after the first failure, then the second delamination is formed leading to final failure. In contrast to the previous studies, these thick $[0]_{15s}$ UD laminates experience two load drops with 1200 N average maximum load also in the previous studies the highest maximum stress occurs at 0.4t. These differences is due to inner radius effect. In preliminary tests the inner radius is 10 mm whereas in this study inner radius is 5 mm. Decrease in inner radius increase the stress level at the curved region. Thus, the specimens experience higher stress state at lower load levels. Moreover, inner radius affects the maximum radial stress location. Curved laminates with 5 mm inner radius have maximum radial stress at 0.35t. Since the laminates are thick, the remaining ligament carries thickness then final failure occurs.

Ultimate average strength of each lay-up configuration is obtained from static loading experiments, then fatigue loading experiments are conducted under displacement control at R-ratio of 0.5 and 3 Hz frequency. Failure patterns are investigated using DSLR camera images and micrographs. The maximum failure loads, stiffness of the load-displacement curves and load drops until failure are observed. Under fatigue loading, [0] UD laminates experience first stiffness reduction corresponding to the first damage. The stiffness reduction is sharp and the material lose 40% of its initial stiffness. However, no delamination is observed from the edges of [0] UD laminates after first stiffness degradation and through-transmission ultrasonic test images showed that corresponding delamination initiates from the interior region of the curvature and progress to the edges. After the first load drop, stiffness degrades gradually with ongoing fatigue cycles. This stiffness degradation corresponds to crack growth in the interior curved region of the laminates which leads to delamination occurring at 0.7t leading to the final failure. The damage progression under fatigue loading behaves different than static failure. Under static loading, two major delaminations occur corresponding to the load drops at the highest radial stress location, whereas damage initiates from the interior curved region corresponding to the first load drop, then interior crack growths in combination with stiffness degradation and leads to edge delamination causing the fatigue failure of [0] UD laminates. In contrast to arm length delamination occurred under static loading, the delamination occurred under fatigue loading is arrested through the curved region. The slopes obtained from the load-displacement curves of static and fatigue loading show differences as well. Under fatigue loading, the initial slope of load-displacement curve is higher than static loading curve. Laminates experience higher loads at lower displacement values under fatigue loading. Also, slight differences are observed

between the initial slopes of two fatigue loading specimens. Strong rate dependence on the stiffness of [0] UD curved laminates is observed as the early failure and higher stiffness during 3 Hz fatigue loading experiments than 2 mm/min static tests.

Fatigue loading experiments of cross-plied laminates are conducted under displacement control at R-ratio of 0.5 and 3 Hz frequency as well. The behavior of load-displacement curves of static and fatigue loadings are similar. Failure corresponding to load drops occurs sequentially starting from the interior off-axis ply where the tensile stress is maximum for both static and fatigue loading case. The initial slope and the slopes observed after load drops are equal in static and fatigue loading. Under fatigue loading, stiffness degradation is sharp not gradual which corresponds to instantaneous crack growth. Besides these similarities of load-displacement curves, static and fatigue failure patterns display similar behavior with slight differences. Damage initiates as matrix cracks in off-axis plies on cross-plied laminates under both static and fatigue loading. Under static loading, matrix cracks lead to dynamic delamination through the arm, whereas under fatigue loading delaminations initiate from the matrix cracks whose length is arrested through the curved region. Under fatigue loading, crack with much shorter length leads specimen to failure, although it is in the same location with the static loading specimens.

Finally, the effects of defects on cross-plied laminates are examined. It is expected that the failure initiates from the interior off- axis ply in cross-plied laminates. However, some specimens display unexpected failure behavior under static and fatigue loading. Micrographs and DSLR camera images of the initial state of the specimens are investigated and defects which occurred during the manufacturing process as voids are observed at critical curved region. It is observed that crack tends to initiate from the voids rather than the maximum tensile stress location. Failure location affects the load drop level and load carrying capacity. If the failure starts from the interior of-axis ply and progress sequentially, cross-plied laminates show more damage tolerant behavior, since after failure load drops to higher level and more plies can carry load until failure. Cross-plied laminates are sensitive to void presence so that manufacturing quality is very critical for performance of the cross-plied laminates. Hand lay-up manufacturing with smaller radius is more prone to void formation so that cross-plied curved composite laminates should be manufactured with higher inner radius values if hand lay-up technique is performed.

7.3. Future work

In the future, the experimental procedure should be fully extended to obtain complete understanding of the effects of geometric parameters on the stiffness and strength of the curved composite laminates. With this aim, static tests should be conducted using the laminates with different thicknesses and inner radii. More fatigue experiments should be conducted on the curved composite laminates for three different lay-ups under various stress states in order to generate full SN curves of the materials. Using

the SN curves a prediction model for damage initiation and propagation should be designed in order to understand the complete damage mechanisms under fatigue loading. In order to strengthen the curved laminates and extend their fatigue life, solution methods should be improved with providing light weight.

REFERENCES

[1] Daniel, I. M., & Ishai, O. (1994). Engineering mechanics of composite materials. New York: Oxford University Press.

[2] Kaw, A. K. (2006). Mechanics of composite materials. Boca Raton, FL: Taylor & Francis.

[3] The History of Composites. (n.d.). Retrieved May 18, 2016, from http://composite.about.com/od/aboutcompositesplastics/a/HistoryofComposites.htm

[4] AMT Airframe Handbook Volume 1 (FAA-8083-31) Ch. 7 Advanced Composite Material Retrieved May 2014 from https://www.faa.gov/regulations_policies/handbooks_manuals/aircraft/amt_airframe_handbook/media/ama_Ch07.pdf

[5] Yancey R., 'Why Composites are Taking Off in the Aviation Industry' Retrived May 22,2012 from http://insider.altairhyperworks.com/composites-aviation-industry/

[6] Worries about new composite made airplane. (n.d.). Retrieved May 18, 2016, from http://www.1001crash.com/index-page-composite-lg-2.html

[7] Australian Transport Safety Bureau (ATSB) 2007b, *Safety Investigation GuidelinesManual – OH&S (v. 1.00)*, report prepared by B Leyshon, M Squires & M Stallbaum, ATSB, Department of Transport and Regional Services, Canberra, p.89-93.

[8] A. (n.d.). A380flightdeck. Retrieved May 18, 2016, from http://a380flightdeck.tumblr.com/post/85909891740/evolution-composite-application

[9] Boeing 787 Specs, what makes a Dreamliner? (n.d.). Retrieved May 18, 2016, from http://modernairliners.com/boeing-787-dreamliner/boeing-787-dreamliner-specs

[10] Shokrieh, M., & Rafiee, R. (2010). Fatigue life prediction of wind turbine rotor blades manufactured from composites. Fatigue Life Prediction of Composites and Composite Structures, 505-537. doi:10.1533/9781845699796.3.505

[11] Salkind, M. (n.d.). Fatigue of Composites. Composite Materials: Testing and Design (Second Conference). doi:10.1520/stp27745s

[12] Forrest, P. G. (1962). Fatigue of metals. Oxford: Pergamon Press.

[13] Harris, B. (2003). Fatigue in composites: Science and technology of the fatigue response of fibre-reinforced plastics. Boca Raton: CRC Press

[14] Sanford, R. J. (2003). Principles of fracture mechanics. Upper Saddle River, NJ: Prentice Hall.

[15] Jones, R. M. (1975). Mechanics of composite materials. Washington: Scripta Book.

[16] Niu MCY. Airframe Structural Design. 2nd Edition. Hong Kong Conmilit Press Ltd, 2002, ISBN 962-7128-09-0.

[17] SAE International -- mobility engineering. (n.d.). Retrieved May 20, 2016, from https://www.sae.org/aeromag/techupdate/06-1999/06.htm

[18] Sørensen BF, Jørgensen E, Debel CP, Jensen FM, Jensen HM, Jacobsen TK, Halling KM. Improved design of large wind turbine blade of fibre composites based on studies of scale effects (Phase 1) - Summary Report. Risø National Laboratory Denmark, 2004, Risø-R-1390(EN).

[19] Immanuvel, D., Arulselvan, K., Maniiarasan, P., & Senthilkumar, S. (2014). Stress Analysis and Weight Optimization of a Wing Box Structure Subjected To Flight Loads. The International Journal Of Engineering And Science (IJES), 3(1), 33-40.

[20] Boeing787 Rescue & Firefighting Composite Structure Retrieved April 2013 retrieved from http://www.boeing.com/assets/pdf/commercial/airports/faqs/787_composite_arff_data.pdf

[21] Poonam Harakare, & Heblikar, V. K. (2013). Evaluation of Static and Buckling load carrying capability of the Wing box through FEM approach. International Journal of Current Engineering and Technology.

[22] Reader materials and structures: 11. Fatigue & Durability. (n.d.). Retrieved May 20, 2016, from http://www.slideshare.net/DelftOpenEr/reader-materials-and-structures-11-fatigue-durability

[23] Reader materials and structures: 6. Aircraft & spacecraft loads. (n.d.). Retrieved May 20, 2016, from http://www.slideshare.net/DelftOpenEr/reader-materials-and-structures-6-aircraft-spacecraft-loads

[24] Vanttinen, A., Strength prediction of composite rib foot corner, Helsinki University of Technology, 2008.

[25] Mouritz, A. P. (2012). Introduction to aerospace materials. Oxford u.a.: Woodhead Publ. Limited.

[26] Foral, R. F. (1991). Delamination Failures in Curved Composite Laminates. Key Engineering Materials, 37(1662), 9795th ser., 137-148.

[27] Martin, R. (n.d.). Delamination Failure in a Unidirectional Curved Composite Laminate. Composite Materials: Testing and Design (Tenth Volume). doi:10.1520/stp20170s

[28] Sridharan, S., Delamination behavior of composites, CRC Press LLC, 2008.

[29] Quaresimin, M., Carraro, P., Mikkelsen, L., Lucato, N., Vivian, L., Brøndsted, P., Talreja, R. (2014). Damage evolution under cyclic multiaxial stress state: A comparative analysis between glass/epoxy laminates and tubes. Composites Part B: Engineering, 61, 282-290. doi:10.1016/j.compositesb.2014.01.056

[30] Whitworth, H. (1997). A stiffness degradation model for composite laminates under fatigue loading. Composite Structures, 40(2), 95-101. doi:10.1016/s0263-8223(97)00142-6

[31] Jackson, W., & Martin, R. (n.d.). An Interlaminar Tensile Strength Specimen.Eleventh Volume: Composite Materials—Testing and Design. doi:10.1520/stp12638s

[32] Martin, R., & Jackson, W. (n.d.). Damage Prediction in Cross-Plied Curved Composite Laminates. Composite Materials: Fatigue and Fracture, Fourth Volume. doi:10.1520/stp24727s

[33] Shivakumar, K. N., Allen, H. G., & Avva, V. S. (1994). Interlaminar tension strength of graphite/epoxy composite laminates. AIAA Journal, 32(7), 1478-1484. doi:10.2514/3.12218

[34] Seon, G., Makeev, A., Nikishkov, Y., & Lee, E. (2013). Effects of defects on interlaminar tensile fatigue behavior of carbon/epoxy composites. Composites Science and Technology, 89, 194-201. doi:10.1016/j.compscitech.2013.10.006

[35] Blanchfield, J.P., & Allegri, G. (2014) Fatigue delamination initiation in L-bend CFRP coupons. ECCM-16TH European Conference on Composite Materials 22-26.06.2014

[36] Charrier, J., Laurin, F., Carrere, N., & Mahdi, S. (2016). Determination of the out-of-plane tensile strength using four-point bending tests on laminated L-angle

specimens with different stacking sequences and total thicknesses. Composites Part A: Applied Science and Manufacturing, 81, 243-253.

[37] Whitworth, H. (2000). Evaluation of the residual strength degradation in composite laminates under fatigue loading. Composite Structures, 48(4), 261-264. doi:10.1016/s0263-8223(99)00113-0

[38] Talreja, R. (1986). Stiffness properties of composite laminates with matrix cracking and interior delamination. Engineering Fracture Mechanics, 25(5-6), 751-762. doi:10.1016/0013-7944(86)90038-x

[39] Wimmer, G., Kitzmüller, W., Pinter, G., Wettemann, T., & Pettermann, H. (2009). Computational and experimental investigation of delamination in L-shaped laminated composite components. Engineering Fracture Mechanics, 76(18), 2810-2820. doi:10.1016/j.engfracmech.2009.06.007

[40] Amadori, M., Design and Development of the New Composite-Metal Mainplane of Dallara T12 Race Car',2012

[41] Mallick, P. K. (2007). Fiber-reinforced composites: Materials, manufacturing, and design (3rd ed.).

[42] http://fab.cba.mit.edu/classes/4.140/section.CBA/people/Henrot/week12.html

[43] ASTM Standard D6415/D6415M, 2006. Standard test method for measuring the curved beam strength of a fiber–reinforced polymer–matrix composite. ASTM International, West Conshohocken PA, 2006, DOI: 10.1520/D6415_D6415M, www.astm.org.

[44] NDT of Composite Materials. (n.d.). Retrieved from https://compositesuk.co.uk/system/files/documents/ndtofcomposites.pdf

[45] Uyar I. Experimental Investigation of Dynamic Delamination in Curved Composite Laminates, M.Sc. Thesis, September 2014.

[46] Kedward, K., Wilson, R., & Mclean, S. (1989). The flexure of simply curved composite shapes. Composites, 20(6), 512. doi:10.1016/0010-4361(89)90880-x

[47] Personal communication with Denizhan Yavaş